Technology Development for Cosmic Microwave Background Cosmology

by

Charles D. Munson

A dissertation submitted in partial fulfillment
of the requirements for the degree of
Doctor of Philosophy
(Physics)
in the University of Michigan
2017

Doctoral Committee:

Associate Professor Jeffrey McMahon, Chair
Professor Katherine Freese
Associate Professor Dragan Huterer
Associate Professor Christopher J. Miller
Professor Gregory Tarle

Acknowledgments

First and foremost, I would like to thank my friends and family, without whose support this thesis would not exist. I am also grateful to the collaborators and colleagues who were instrumental in the success of the projects I undertook as a graduate student. I would like to thank Kongpop U-Yen for serving as my mentor at NASA Goddard Space Flight Center, and Jeff McMahon, Chris Miller, and Ed Wollack for their guidance and advice throughout my thesis.

My efforts were supported by a University of Michigan Regent's Fellowship and a National Aeronautics and Space Administration (NASA) Space Technology Research Fellowship (NSTRF) under Grant No. NNX12AM32H.

Table of Contents

List of Tables

List of Figures

List of Appendices

Abstract

The Cosmic Microwave Background (CMB) offers a unique window into the early universe by probing thermal radiation remaining from the big bang. Due to its low temperature and bright foregrounds, its thorough characterization requires technological advancement beyond the current state-of-the-art. In this thesis, I present the development and fabrication of novel metamaterial silicon optics to improve the sensitivity of current and future CMB telescopes. By machining subwavelength features into the silicon surfaces, traditional antireflection coatings can be replaced by all-silicon metamaterials that significantly reduce reflections over previous approaches. I discuss the design of these structured surfaces and the design and construction of a sophisticated fabrication facility necessary to implement this technology on large diameter (30+ cm) lenses for the Atacama Cosmology Telescope Polarization project (ACTPol). I then apply this metamaterial technology to the development of improved free-space filters for millimeter and sub-millimeter wavelength imaging (focusing specifically on blocking infrared radiation, necessary for current cryogenic detector systems). This produces a highly effective infrared-blocking filter, blocking over 99% of the incident power from a 300 K blackbody while maintaining transmission of better than 99% in a target CMB observing band (between 70 and 170 GHz). I conclude with a discussion of the development of a real-space simulation framework to assist in better understanding current CMB results and forecasting for future experiments. By taking a CMB realization and adding to it accurate real-space modeling of the Sunyaev-Zel'dovich effect and weak lensing distortions (introduced by galaxy clusters), a better understanding of the impacts of large scale structure on the CMB can be obtained.

Chapter 1

Introduction to Cosmic Microwave Background Cosmology

> In the beginning the Universe was created. This has made a lot of people very angry and been widely regarded as a bad move.
>
> Douglas Adams, The Restaurant at the End of the Universe

Cosmology is the study of the structure and origin of the universe as a whole. The Cosmic Microwave Background, as the oldest observable light and as radiation emitted shortly after the big bang, provides a powerful probe of the universe on the largest scales and in its earliest moments. This makes it a natural tool for the study of cosmology.

In this chapter, I will give a brief overview of the history of cosmology, leading up to the discovery of the Cosmic Microwave Background. I will then discuss the Cosmic Microwave Background and its usefulness as a tool for illuminating the conditions of the early universe and structure of the universe on its largest scales.

1.1 Turtles All the Way Down: A Brief Timeline of Cosmological Theories

Since mankind first gazed up at the stars, we have pondered the shape and structure of the universe and our place in it, as well as how it came to have this shape and structure. As early as the beginnings of civilization itself, people have been describing the structure of the universe and its origins. In the beginning, this was a static universe that was created, in its current form, for mankind to dwell in. In early

Mesopotamian cultures (as chronicled in cuneiform writings from the Sumerians and Akkadians), the universe is described as consisting of discrete levels separated by empty space. The highest of these levels were the heavens, where the gods resided. Below the heavens sat the starry sky, which stood above the Earth's surface. Below the Earth's surface were the subterranean waters and the underworld. These levels that constituted their universe were built by the gods in the early times and were held together by cosmic bonds [16].

1.1.1 The Cosmology of the Greek Philosophers

Throughout much of the rest of human history, our concept of the cosmos has been very similar. We have envisioned the universe as static, centered upon the earth and humankind, and assembled in its present form in some moment of creation long ago. As humanity's mathematical and philosophical understanding developed, so did our views on the structure and origin of the universe. The Greeks, with a strong tradition of philosophical inquiry, sought to provide a fundamental picture of the structure and workings of the universe beginning with Plato in the 5th century B.C. Plato looked to understand and explain the physical world with logical thought, and when he turned to the heavens, he explained their motion with uniform circles. This view (and variants thereof, such as the epicycles needed to correct the perceived motion of the planets) of stars following uniform circular motion persisted until the 17th century A.D., when Johannes Kepler demonstrated that the planets follow elliptical orbits around the sun [17].

Aristotle, around the 4th century B.C., described a modified geocentric universe in which celestrial bodies were carried by nested spheres that rotated around the Earth, with all Earthly materials falling to the center. This universe was, by necessity of its construction, finite in span and eternal. Not long after, in the 3rd century B.C., another Greek philosopher, Aristarchus, presented the first described model placing the sun at the center of the universe, with the Earth revolving around it [18]. Aristarchus also suggested that the stars were similar to our sun, but his theories were met with little enthusiasm and the heliocentric universe remained unpopular. Ptolemy introduced a further modification on the Aristotelian spheres in which these hollow spheres moved relative to each other, allowing for more complicated movement of heavenly bodies with respect to each other and the Earth. These concepts were developed further over the following centuries, including by Arab and Persian mathematicians and astronomers who devised improved astronomical techniques, such as the method

to construct linear motion from a combination of uniform circular motions (the Tusi couple, a technique similar to one that later appeared in Copernicus's description of the solar system) [17]. Variants of the Aristotelian cosmological model were prevalent until modern astronomical techniques provided the data to build an orbital model of the solar system founded in precise observations, which didn't occur until the 17th century.

This began to change in the early seventeenth century with the foundation of observational astronomy by Galileo Galilei, Johannes Kepler, and others, aided by the recent development of telescope optics [19]. The improved observations that followed (and indirectly, the modern scientific processes that began with Galileo during this time) began the shift towards our current cosmological views and the scientific description of the universe on its largest scales.

1.1.2 The Beginnings of Modern Astronomy: Copernicus, Galileo, and Kepler

Starting in the early 16th century, Nicolaus Copernicus began to work on a heliocentric cosmological theory that set the foundation for modern astronomy and the shift to a scientific approach to cosmology. With some possible inspiration from the works of Aristarchus [20], Copernicus posited that the center of the universe was in the vicinity of the Sun, around which the six known planets orbited. He first announced these ideas in *Commentariolus* in 1514 [21], and gave a careful description of this theory, as well as the motions of the planets and the moon in his manuscript *On the Revolutions of Heavenly Spheres (De Revolutionibus Orbium Coelestium)* which he completed in 1530 and published in 1543 [18]. In the interim, Georg Joachim Rheticus, a young professor and pupil of Copernicus, published his *Narratio Prima* describing advantages of the heliocentric system and claiming that "each of the planets, by its position and order and very inequality of its motion, bears witness that the earth moves." This concept was developed by Copernicus during the following years and ultimately led to the detailed observations in *On the Revolutions of Heavenly Spheres*. This manuscript provided accurate determination of the order and distances of the known planets and detailed the dynamics of their orbits as determined by the mathematics of epicycles and equants (betraying an infatuation with uniform circular motions that ultimately undermined the usefulness of the Copernican system in the long run)[21] . He also suggested that each heavenly body might possess its own gravity, an idea that later led to the development of a mathematical description of

gravitation. This was the first serious challenge to the presumed geocentric system in many centuries, and it lay the foundation for a revolution in astronomy and cosmology [18]. Figure 1.1 shows sketches from Copernicus's book in which he lays out the motion of objects in the mathematical language of epicycles.

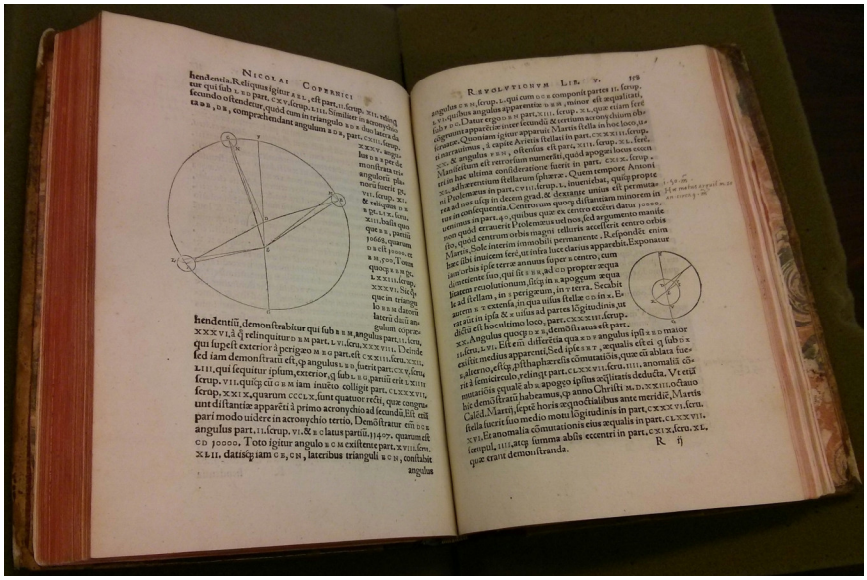

Figure 1.1: The motion of celestial objects, laid out in epicycles according to Copernicus. Book courtesy of the University of Michigan Special Collections Library.

In the late 16th century, the Danish astronomer Tycho Brahe made a series of precise astronomical observations as the last of the great astronomers unaided by telescopes. He observed comets moving through the solar system, the paths of which were incompatible with the Ptolemaic idea of heavenly bodies fixed to crystal spheres that rotated around the Earth. His detailed observations also served as the basis for the work done by Johannes Kepler (both before his death, during which Kepler was employed by him, and after it, due to Kepler inheriting the data he had collected), in which Kepler demonstrated that the motions of the planets followed elliptical orbits with the Sun at one focus [22]. Kepler's work, as he strove to elegantly describe a Copernican system that matched the precise data from Tycho Brahe, led him to determine the laws of planetary motion for which he is still known, and which set in motion the scientific path to Newton's discovery of a mathematical law of gravitation [18]. While Brahe's geocentric cosmological system was incorrect, it incorporated aspects of the Copernican system (indeed, it was likely inspired by the Copernican system [21]), and served as the basis for another step towards a scientifically grounded cosmological theory. Figure 1.2 shows a portrait of Tycho Brahe from the title page of his book describing astronomical instruments.

Figure 1.2: Tycho Brahe, the Danish astronomer, represented on the title page of the book describing his astronomical instruments, Astronomiæ Instauratæ Mechanica. Book courtesy of the University of Michigan Special Collections Library.

It was also during the late 16th and early 17th centuries that Galileo Galilei, the famed Italian astronomer and physicist and the "father of observational astronomy" [23], made his observations that similarly helped to undermine the ideals of Aristotelian cosmology that had prevailed until then. Galileo made a number of important telescopic observations of various celestial objects, including detailed observation of the moon's surface in which he determined that it was uneven and rough, like an earthly material, and not smooth as was expected of a celestial body. He also discovered the 4 largest moons of Jupiter (See Figure 1.3 for the letter describing this discovery), and noted their orbit around an object that was not Earth. These observations demonstrated that the Earth was not the sole locus of earthly matter and was not the only point around which heavenly bodies rotated [19].

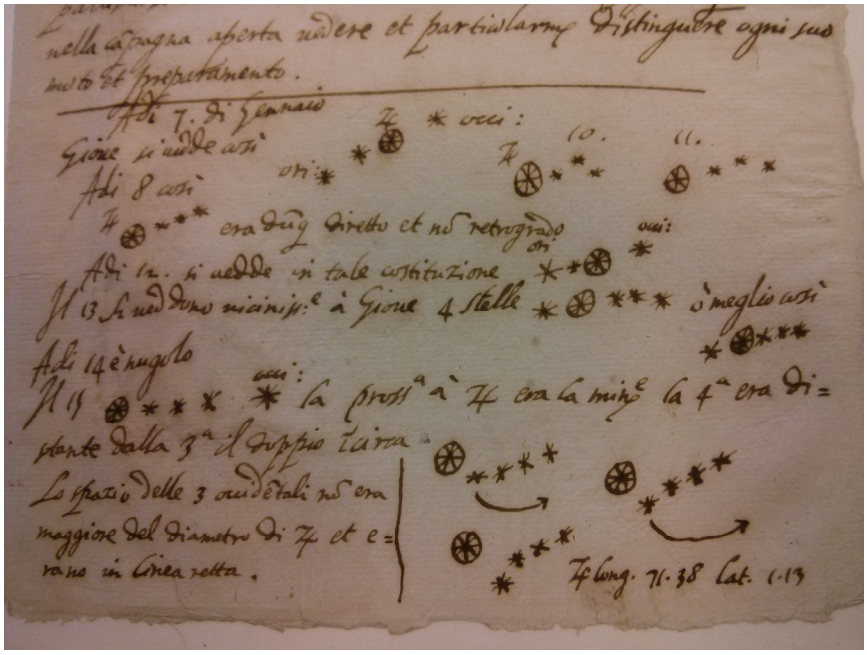

Figure 1.3: A draft of the letter in which Galileo described his discovery of the first four moons of Jupiter. The sketched figures throughout depict the motion of these moons relative to Jupiter and to each other over the course of several observations. Document courtesy of the University of Michigan Special Collections Library.

1.1.3 Newtonian Mechanics and the Physics of the Cosmos

In 1718, the Astronomer Edmond Halley discovered that 3 bright stars had moved relative to their previously established positions. This called into question the long-standing assumption that the stars remained in fixed locations in the sky, and introduced the possibility of the stars moving mechanically, as earthly objects are wont to do. Isaac Newton began with the motion of celestial (as well as earthly) bodies, and treated this as a problem for mechanics. In doing so, he developed a theory of gravitation that accurately described the elliptical orbits followed by the planets (with a little help from perturbative corrections introduced by Leonhard Euler necessary to improve the calculated orbits of the Moon, Jupiter, and Saturn, anomalies in which were later resolved by Pierre-Simon Laplace). The development of a mathematical theory of gravitation brought the cosmological view of the universe firmly into the scientific domain and provided the necessary framework to truly begin discussing the dynamics of the heavens. All at once, the multitude of celestial objects, once thought to be eternal and unmoving - placed at the moment of creation - were correctly viewed as dynamic objects. They moved according to the same dynamical rules that governed the earthly world, and their dynamics could offer insight into their underlying

nature and physical characteristics.

Laplace, in addition to resolving anomalies in the orbits of Jupiter and Saturn, was an early proponent of the nebular hypothesis, which posited that stars were formed by the cooling and condensation of massive rotating nebular clouds of hot gas. This idea took another step to bringing the scientific description of the cosmos into the realm of physical mechanics, and with it, mankind developed the next step in understanding the dynamics of the cosmos and the mechanisms of their formation.

As the end of the 18th century approached, improvements in the size and quality of telescopes enabled ever better observations, and through them, further advances in man's understanding of the universe. William Herschel, enabled by his construction of massive reflecting telescopes, peered deeper into the heavens than ever before, and noticed patterns in the distribution of nebulae and clusters of stars that suggested the structure we now know as the Milky Way [24]. He described a (not wholly accurate) massive, branching structure of millions of stars, and (erroneously) placed our solar system near the center based on the distribution of stars around us. This theory contained too many flawed premises to convince the scientific community, though, and cosmology stagnated until the improved telescopes and observations in the early 20th century began to illuminate further depths of the cosmos.

1.1.4 The Path to the Big Bang

In the early 20th century, several new observatories were founded, and astronomical photography began to better characterize observations of faint astronomical objects, leading to a greatly expanded view of the structure of the universe. Harlow Shapley, using the 60 inch telescope at Mount Wilson Observatory, discovered the first hint at the larger universe and added a rung to the measurement ladder for establishing cosmic distances. Shapley noticed faint stars in distant clusters, and established their distances using the properties of Cepheid variable stars [25], whose characteristic brightness variation had been observed a few years earlier by Henrietta Leavitt. Leavitt had noticed that the period of brightness variation of a class of stars (now known as Cepheid variables) was related to the overall brightness of the star [26]. Shapley used this periodicity to establish absolute brightness of a given star, and then obtained the distance from the observed brightness. This enabled the first real distance measurement of faint globular clusters of stars, and provided the observation that they were distributed evenly across the sky (except for in the plane of the Milky Way, where clouds of intervening material mask their presence). The great distance

to these globular clusters, now established as part of our galaxy, portrayed a galaxy far more vast than originally thought, and paved the way for the establishment of a universe of countless such galaxies.

The remainder of this road was paved by Edwin Hubble, who noticed a few faint nebular objects that could be resolved into individual stars. After joining the staff of Mount Wilson Observatory (following Shapley's departure), Hubble discovered variable stars in one such nebula, and through diligent observation, established its distance. He determined this distance to be some 300,000 parsecs [27], placing it well beyond Shapley's estimates for the outer limit the Milky Way, and in doing so, illuminated a universe of massive galaxies like our own [28].

At the same time during the early 20th century, the theoretical underpinnings of modern cosmology were being formulated. Beginning with Einstein's description of the interactions between space and matter laid out in his field equations [29], there was a theoretical tool that was suitable for describing the dynamics on the largest scales, as required by the recently discovered scale of the universe. Using this tool to describe the universe as a whole, however, proved a formidable task that was set upon by a number of scientists in the early 1900s. Most notably, Willem de Sitter and Einstein himself [30]. Both Einstein and de Sitter devised separate solutions to the field equations, but they described very different universes and were both plagued by a number of troubling problems. Neither model could allow for the universe to contain matter and remain stable in a static universe. Einstein adjusted his model with the addition of a "cosmological constant" that provided expansion to counter the natural tendency of the universe to collapse under the gravitational attraction of matter, but it remained an unsatisfactory solution.

In the 1920s, measurements of distant nebulae suggested that the nebulae were receding, with the more distant nebulae receding faster. This discovery was first made by Vesto Slipher in 1915 [31], and was thoroughly characterized in 1929 by Edwin Hubble, who noted a linear relationship between the distance and recession velocity of distant nebulae [32], provided evidence that the universe was not, in fact, static. Fortunately, there were other scientists who had devised dynamical-universe solutions to Einstein's field equations. Alexander Friedmann, a Russian mathematician, and Georges Lemaître, a Belgian astrophysicist and Catholic priest were chief among these. In 1927, Lemaître proposed a model of an expanding universe [33, 34], which proved consistent with the observations of receding nebulae[35] and ushered in the era of the big bang (for he advocated that the present universe was the aftermath of some earlier explosion, akin to a firework). Mankind now looked out upon a vast

universe, filled with distant galaxies made of countless stars, ever receding into the night.

1.1.5 Modern Cosmological Theory

The 1930s and early 1940s held a lull in cosmology, due in part to the world war's diversion of resources from scientific endeavors to military ones, but in the late 1940s cosmology again surged forward. In 1948, George Gamow and Ralph Alpher published their calculations of how the early stages of a hot, expanding universe would give rise to nucleosynthesis of hydrogen and helium. Starting with the assumption of an enormously hot and dense early universe, and allowing it to expand and cool, they determined that elements could be formed in proportions (at least for hydrogen and helium) that agreed with the relative abundances observed in stars [36]. The expanding universe of the big bang was also aided by the recently developed techniques of radio astronomy. The war had prompted the development of drastically improved techniques for detecting faint radio signals due to military research on RADAR, and these tools were turned skyward after the war's end.

One consequence of the hot, dense early universe of the big bang model (in addition to synthesis of helium in nuclear reactions) was an early universe filled with radiation. As the universe cooled and expanded, a remnant of this radiation would persist, propagating throughout all space. Ralph Alpher and Robert Herman calculated this radiation remnant to have a temperature of approximately 5K [37], and in doing so, predicted the existense of what would come to be known as the Cosmic Microwave Background (CMB).

Microwaves, being used for RADAR and later communication, inadvertently led to the discovery of this critical hint at the universe's past. In 1964, Arno Penzias and Robert Wilson, working at Bell Labs on microwave receivers, had a noise problem. They diligently eliminated or characterized as many sources of noise as they could in the Crawford Hill horn antenna (see Figure 1.4), but excess noise remained. They eliminated terrestrial radio signals, possible atmospheric effects, and even pigeon droppings in the horn itself, but retained excess noise with an intensity equivalent to 3.5K [38]. Word of this noise made its way to Princeton University, and following a discussion with Robert Dicke, Penzias had his explanation: the cosmic background radiation had been discovered [39]. The two groups published their findings, Penzias and Willson describing their noise excess, and Dicke discussing the cosmic background radiation that provided it, in adjacent papers in The Astrophysical Journal [38, 40],

and the Cosmic Microwave Background became the next compelling piece of evidence for the hot big bang.

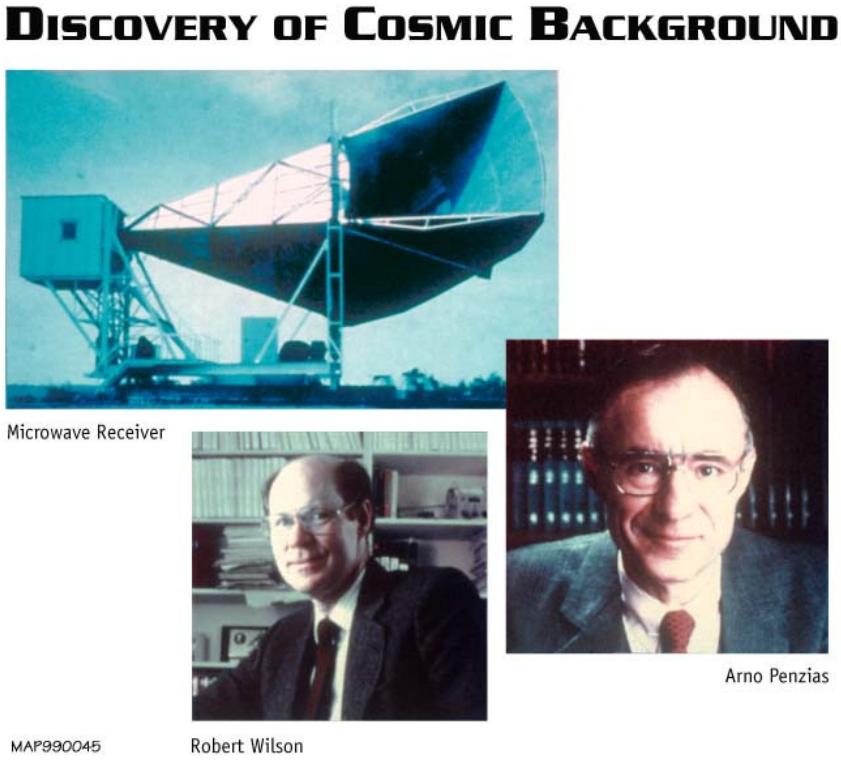

Figure 1.4: Arno Penzias (right) and Wobert Wilson (bottom), researchers at Bell Labs credited with the discovery of the CMB using the Crawford Hill horn antenna (upper left). This discovery opened up a new window for the study of cosmology, and began an era of exciting new discoveries about the early universe. Figure courtesy of NASA.

This big bang theory served as the basis for the current standard cosmological model, with the addition of an early period of rapid inflation (introduced by Alan Guth [41]) that serves to flatten the universe (bring it close enough to the critical mass density to yield a current universe as flat as we observe, known as the flatness problem), provide homogeneity on the largest scales, where regions otherwise would have spent their entire history causally disconnected (called the horizon problem, and a characteristic noticeable in even the earliest measurements of the CMB), and reduce the number density of magnetic monopoles (which could potentially have been created in the high energies of the early universe, if Grand Unified Theories of particle physics prove true) to levels consistent with the complete lack of detection in the volume of the potentially observable universe [42]. Adding to this theory dark matter (gravitationally, but not electromagnetically interacting matter) as suggested

by the anomalous rotation curves of galaxies and confirmed by a number of different experiments, including gravitational lensing and x-ray surveys, yields the current standard cosmological model [43]. This model consists of a hot big bang, cosmological inflation, dark matter, and dark energy (manifested as the cosmological constant originally proposed by Einstein to stabilize his solution to the field equations, and reintroduced to provide for increasing expansion in the late universe), and provides an excellent description of the universe as we currently observe it.

1.2 The Cosmic Microwave Background

The cosmic microwave background is the remnant radiation left over from the early universe. In the moments following the big bang, the universe was hot and dense. In this state, it consisted of a hot baryon-photon fluid, with radiation strongly coupled to the baryonic matter that was formed during big bang nucleosynthesis. From this early state, the universe cooled and expanded, while overdensities (the result of quantum fluctuations before inflation) collapsed under gravity. The gravitational collapse was countered by radiation pressure in the plasma, giving dynamics that yielded characteristic structure in this primordial universe. When the universe was $\sim 380,000$ years old, it had cooled to the point where protons and electrons in this baryon-photon fluid combined to form neutral hydrogen, reducing the coupling to photons and allowing them to propagate freely through the universe (a process known as free streaming). The light emitted from this era of decoupling (known as the surface of last scattering) has propagated forward to the present day, where it is seen as the cosmic microwave background (CMB). It presently exists as radiation with a temperature of 2.725K due to the factor of $\sim$1000 redshift of wavelength from the expansion of space in the intervening time. This light has been measured and characterized in increasing detail since its discovery in 1965, and has provided measurements that have helped establish our current cosmological description of the universe. Figure 1.5 shows a schematic view of the universe from the big bang to present day, with the decoupling of the CMB shown.

As the earliest visible light, emitted during the transition from opaque plasma to transparent gas, the CMB offers a powerful probe of cosmology, offering both a window into the conditions of the early universe and a probe of matter in the late universe. These effects appear as small anisotropies in the CMB at the level of 10^{-5} on top of the 2.7K thermal distribution. These anisotropies contain a wealth of information about the conditions in the universe at and before the surface of last scattering, and

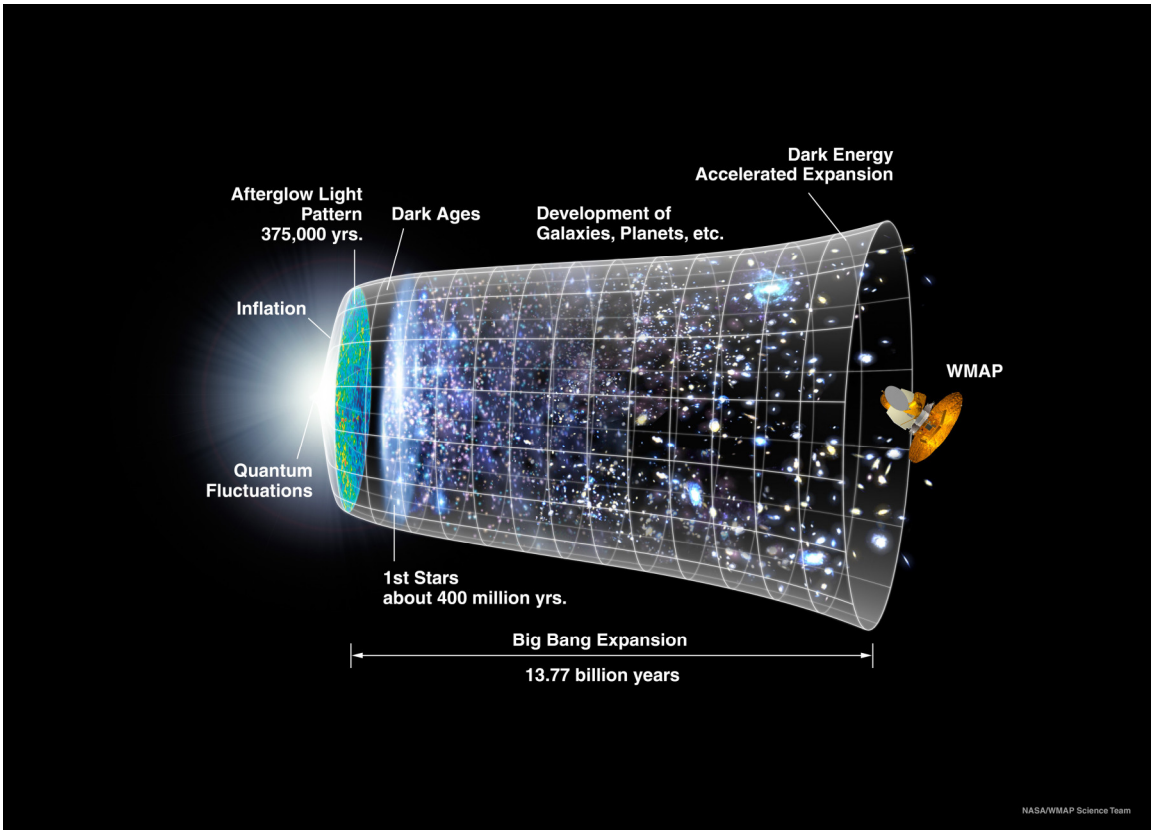

Figure 1.5: A schematic view of the history of the universe. Starting with quantum fluctuations (left side) frozen by inflation, the universe passed through a hot dense state which ended with the decoupling of the CMB and combination to neutral hydrogen. This was followed by a dark period, which was followed by the gravitational coalescing of matter into stars, the gradual formation of larger structures, and ultimately, the formation of the structure we see in the universe today. Figure courtesy of NASA.

also contain the imprints of large scale structure introduced by gravitational lensing and scattering of CMB photons off charged particles. Following its initial detection and the realization that it potentially held valuable cosmological information encoded in it, the CMB was characterized several times by increasingly sensitive experiments. The COBE (Cosmic Background Explorer) satellite was launched by NASA in 1989 to explore the CMB and marked the beginning of precision CMB cosmology. COBE precisely measured the CMB blackbody temperature (See Figure 1.6 for the spectral characterization of the CMB and a its comparison to an ideal blackbody) and discovered temperature anisotropies at the level of 1 in 100,000, which it mapped for the first time [44].

The COBE satellite was followed up by the Wilkinson Microwave Anisotropy

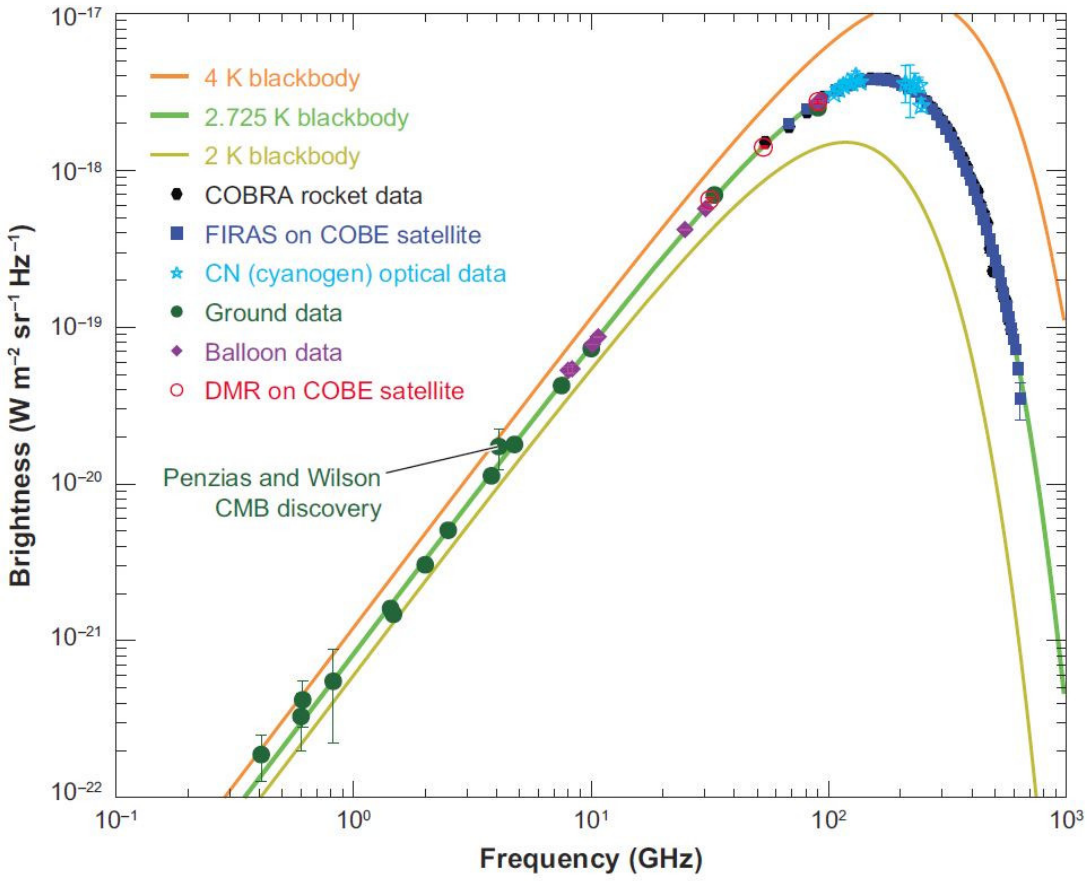

Figure 1.6: The brightness of the CMB, as a function of frequency and measured by a variety of different experiments. This shows that the CMB, to high precision, matches a 2.725K blackbody. Particularly noteworthy measurements are the CMB discovery by Penzias and Wilson (called out on the left side of the plot), and the FIRAS instrument from the COBE satellite (a calibrated spectrophotometer which definitively determined the temperature of the CMB to be 2.725K [2]. Figure from [3].

Probe (WMAP), which aimed to thoroughly characterize the CMB anisotropies in order to make fundamental measurements of cosmological parameters, at which it was incredibly successful. WMAP greatly improved the precision of cosmological parameters obtained from the CMB, and helped usher in the era of precision cosmology. These measurements are used as the standard of comparison for cosmological parameters, and the resulting best-fit parameters from the full mission can be found in Table 1.1. WMAP also mapped the polarization of the CMB, adding further measurements that improve the ability of the CMB to yield cosmological and astrophysical information.

Parameter	Symbol	WMAP data	Combined data
Fit ΛCDM parameters			
Physical baryon density	$\Omega_b h^2$	0.02256	0.02240
Physical cold dark matter density	$\Omega_c h^2$	0.1142	0.1146
Dark energy density ($w = -1$)	Ω_Λ	0.7185	0.7181
Curvature perturbations, $k_0 = 0.002 Mpc^-1$	$10^9 \Delta_R^2$	2.40	2.43
Scalar spectral index	n_s	0.9710	0.9646
Reionization optical depth	τ	0.0851	0.0800
Derived parameters			
Age of universe (Gyr)	t_0	13.76	13.75
Hubble parameter, $H_0 = 100h$ km/s/Mpc	H_0	69.7	69.7
Density fluctuations $8h^-1 Mpc$	σ_8	0.820	0.817
Baryon density/critical density	Ω_b	0.0464	0.0461
Cold dark matter density/critical density	Ω_c	0.235	0.236
Redshift of matter-radiation equality	z_{eq}	3273	3280
Redshift of reionization	z_{reion}	10.36	9.97

Table 1.1: Maximum Likelihood ΛCDM Parameters from WMAP 9 Year Cosmological Results[1]. Combined data includes WMAP, other CMB experiments, baryon acoustic oscillations, and hubble constant measurements. The top six parameters are the six ΛCDM free parameters, and the derived parameters are other values of physical interest derived from them.

Satellite CMB missions are aided by an array of ground-based and balloon-based experiments, which trade larger telescopes (enabling better angular resolution, and therefore the mapping of smaller structures in the CMB) and lower cost for varying degrees of atmospheric contamination and the inability to survey the entire sky from a single site. Large ground-based telescopes like the Atacama Cosmology Telescope (ACT) [45] and the South Pole Telescope (SPT) [46] complement space-based observatories by offering excellent angular resolution and serving as a proving-ground for the next-generation detector and optical technologies that are critical for the future of CMB science. Figure 1.8 shows a comparison between several hypothetical CMB experiments, illustrating the need for ground- as well as space-based observatories.

While the current measurements are incredibly successful, future instruments are needed to realize the full scientific potential of the CMB. These future instruments will offer the ability to make improved polarization measurements, as well as have the sensitivity to study large-angular-scale B-modes (indicative of early-universe gravitational waves), place better constraints on the sum of neutrino masses, and better characterize dark energy. They will also allow cataloging of galaxy clusters through improved measurements of the Sunyaev-Zel'dovich effect and weak gravitational lens-

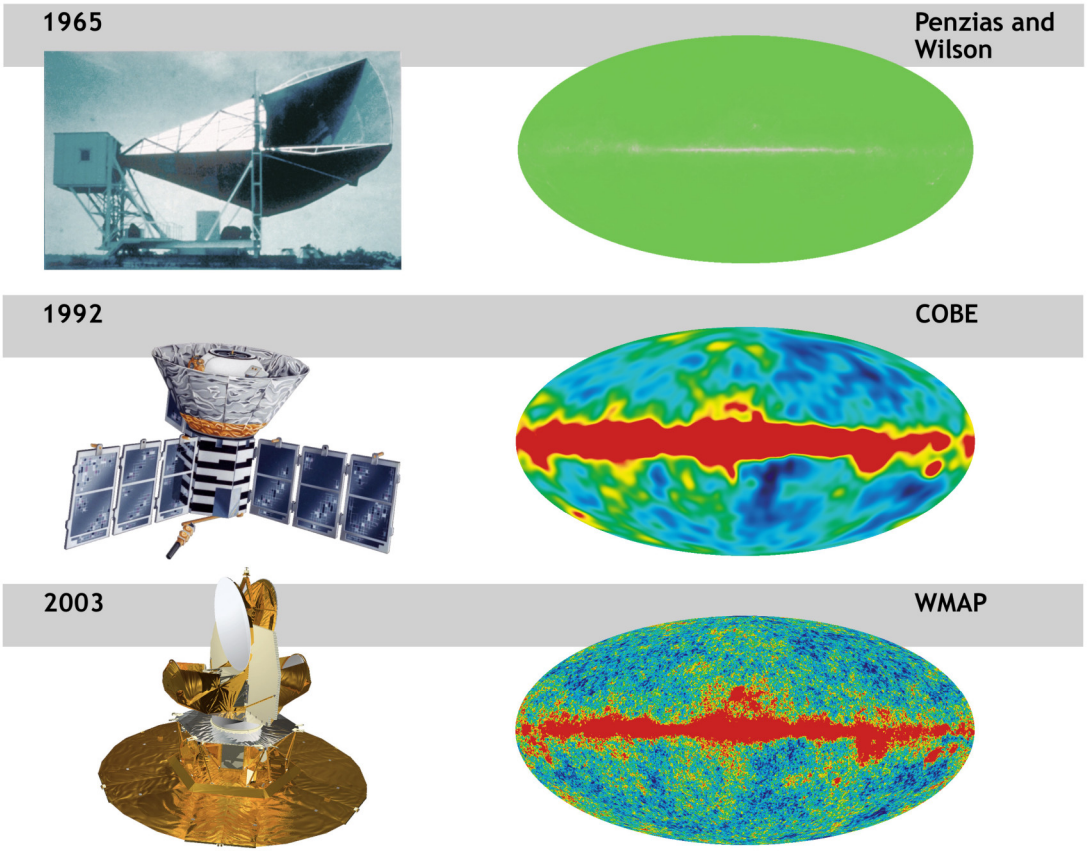

Figure 1.7: Maps showing progressive measurements of the CMB (right column), and the instruments responsible for them (left column). The original 1965 measurement by Penzias and Wilson established the existence of the CMB and showed a uniform temperature across the sky (excepting, of course, the galactic plane, which is filled with bright foreground emission). This was followed up by the COBE satellite in 1992, which established and mapped the intrinsic anisotropy of the CMB for the first time. This was followed by the WMAP satellite, which mapped these fluctuations precisely and used this to determine the composition of the universe and numerous other cosmological parameters to excellent precision. Figure courtesy of NASA.

ing.

1.2.1 CMB Anisotropies

Almost all of the cosmologically useful information encoded in the CMB (with the exception of its base temperature and uniformity across the sky) is embedded in the small anisotropies distributed across the sky. These anisotropies are present in both the temperature and polarization signals (with the polarization being discussed in the next section), and provide a wealth of scientific information from their careful

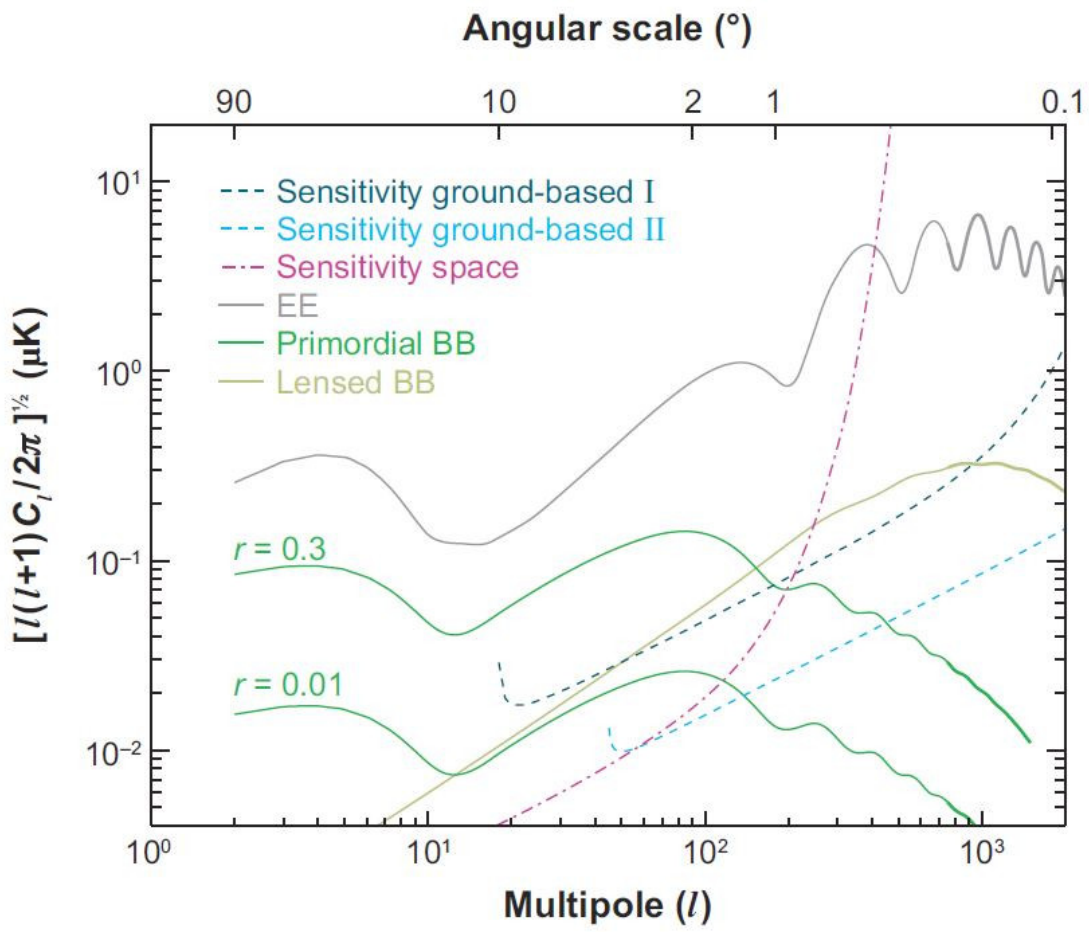

Figure 1.8: The sensitivity of several hypothetical CMB experiments, at comparable technology levels, and the CMB polarization power spectra. The pink dashed line shows the sensitivity of a hypothetical satellite mission, while the blue lines show sensitivities for a 6-arcmin resolution (experiment I) and 1-arcmin resolution ground-based experiments covering 4% and 0.4% of the sky respectively. This illustrates the usefulness of ground-based telescopes in reaching the small-angular-scale CMB features (an effect resulting from the greater achievable size of ground-based instruments, leading to larger apertures and consequently better angular resolution). Figure from [3].

characterization.

The typical observable discussed in CMB observations, then, is these anisotropies. Since they are a two-dimensional pattern on the sky, it makes sense to write them down as decomposed into spherical harmonics. If $\Theta(\hat{\mathbf{n}}) = \Delta T/T$, is defined to be the temperature fluctuation in a given direction, then it can be decomposed into spherical harmonics.

$$\Theta_{\ell m} = \int d\hat{\mathbf{n}} Y^*_{\ell m}(\hat{\mathbf{n}})\Theta(\hat{\mathbf{n}}) \tag{1.1}$$

If the fluctuations are Gaussian, then they can be fully characterized by their power spectrum, C_ℓ.

$$\langle \Theta^*_{\ell m}\Theta_{\ell' m'}\rangle = \delta_{\ell\ell'}\delta_{mm'}C_\ell \tag{1.2}$$

Thus, the standard representation of CMB measurements is as a set of power spectra of measured fluctuations [3, 4]. A TT power spectrum (temperature fluctuations correlated with themselves), can be found in Figure 1.9. The measured CMB sky from the Planck collaboration (the source of this power spectrum) can be found in Figure 1.10.

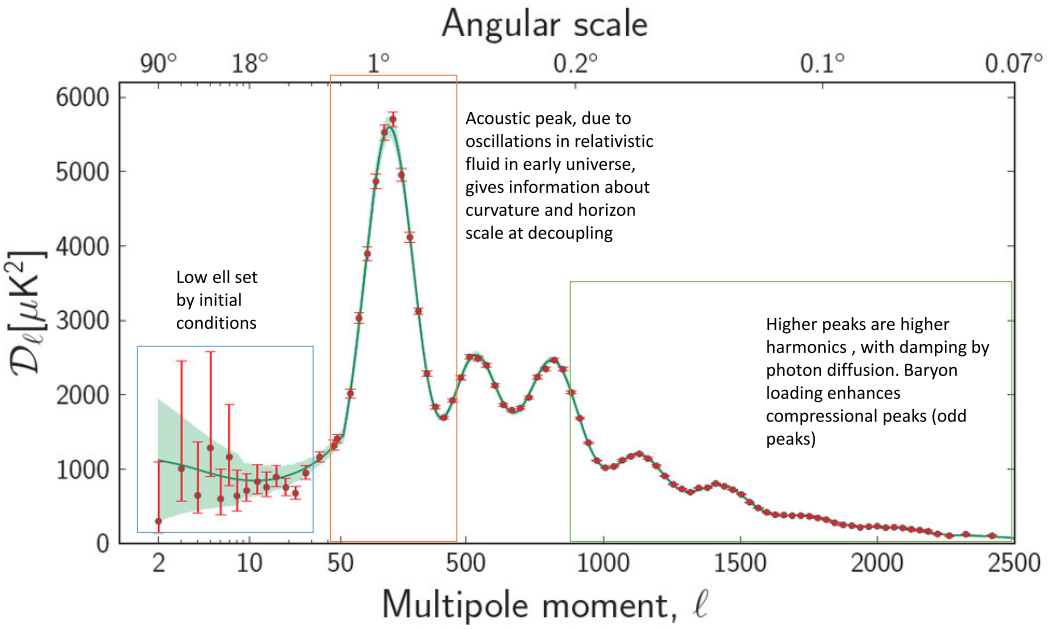

Figure 1.9: A TT power spectrum from the Planck collaboration, with various features called out. At low ℓ (large angular scale), the spectrum is set by the initial conditions in the early universe, and the statistical error increases due to the limited number of independent samples available (cosmic variance). At approximately one degree sits the first peak, the acoustic peak, which is the result of oscillations in the relativistic fluid in the early universe. Its location tells us the universe is flat. The higher peaks are higher harmonics, corresponding to more oscillations in the relativistic fluid and with damping due to photon diffusion. These are impacted by the baryonic content of the early universe.

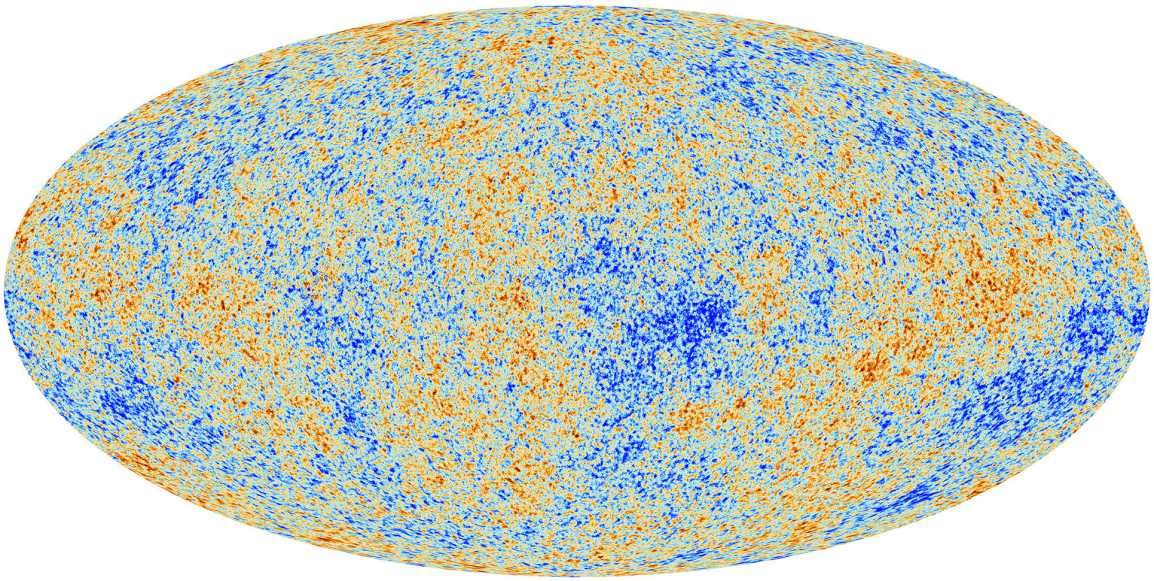

Figure 1.10: Anisotropies of the Cosmic Microwave Background, as measured by the Planck satellite and after masking the galactic plane and reconstructing the obscured CMB. These higher-resolution large scale measurements promise to replace WMAP as the standard CMB sky, and offer improved cosmological information over previous projects.

1.2.2 The Polarized CMB

In order to realize the full scientific potential of the CMB, both its temperature and polarization must be carefully characterized. The CMB is intrinsically polarized due to spatial inhomogeneities during its creation. If there is a quadrupole anisotropy in the temperature around a scattering center, scattering of radiation will generate a linear polarization (shown in Figure 1.11). Temperature quadrupoles are generated during decoupling due to oscillations in the early plasma, so a polarized CMB is expected. Since the polarization is a result of scattering, its anisotropy is lower than that in temperature, require even more sensitive instruments to properly characterize.

Polarization has the potential to contain more information than temperature alone. It must be characterized by both a degree of polarization and a direction, and this field can be decomposed into two components, E and B, which are scalar and pseudoscalar fields respectively (see 1.11 for an illustration of these E- and B-mode patterns). This decomposition is useful in reaching the fundamental physics of the CMB, as E-modes arise from density perturbations which do not produce B-modes, and B-modes arise from tensor distortions of the space-time metric (in the early universe). Unfortunately, B-modes can also result from gravitational lensing, which generates B-modes from E-modes. Additionally, astrophysical foregrounds can

generate B-mode patterns, further interfering with their accurate measurement [3, 4].

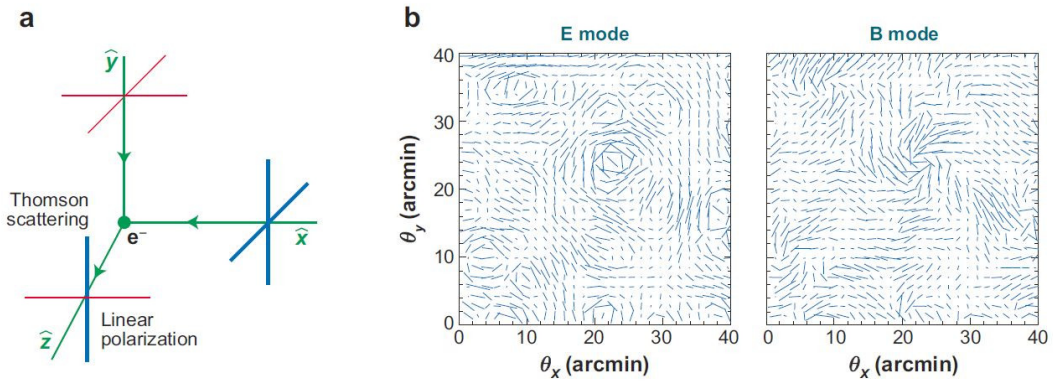

Figure 1.11: Polarization of the CMB. Panel a shows how quadrupole temperature anisotropies can lead to polarized radiation. The line thickness represents intensity. The different electric field orientations probe different directions, which are at different temperatures. Scattering of these different intensities off an electron yields a net polarized signal. Panel b shows the E and B mode polarization patterns. The line lengths represent the degree of polarization and their orientation gives the direction of maximum electric field. Figure from [3].

The power spectra of the CMB polarization patterns can be found in Figure 1.12.

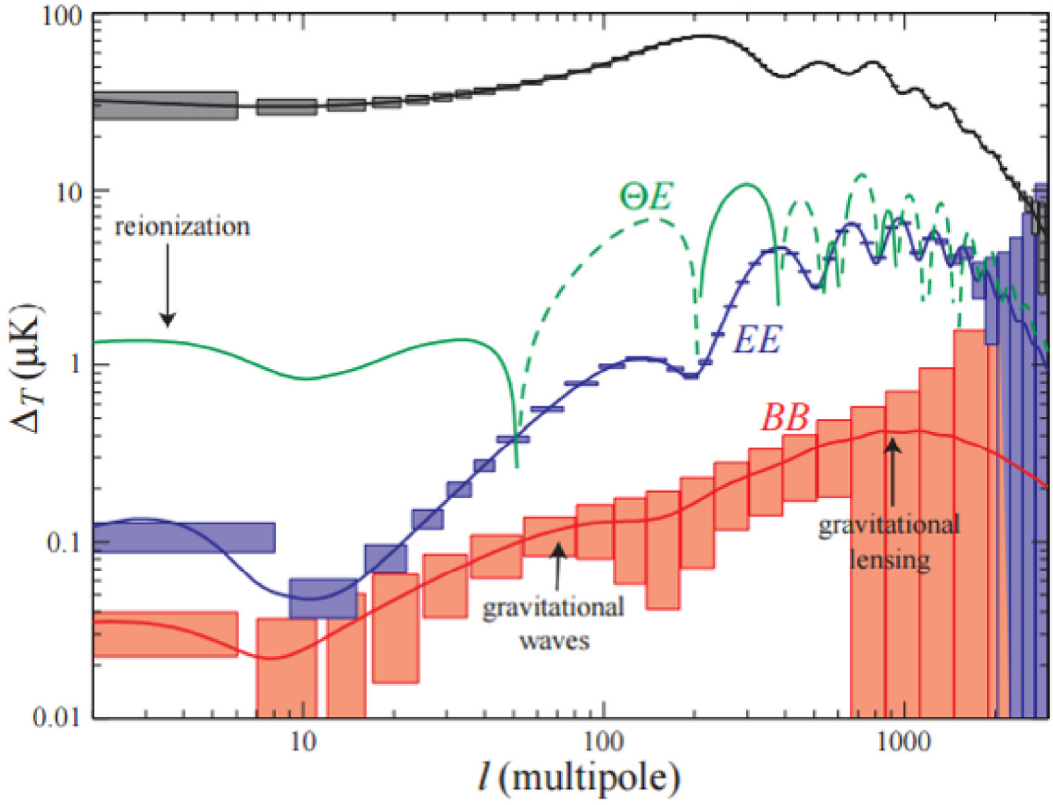

Figure 1.12: Theoretical temperature and polarization spectra. Dashed lines represent negative cross correlation and boxes represent the statistical errors predicted for the Planck satellite. Figure from [4].

1.2.3 Observing the CMB: Astrophysical Foregrounds

For all its cosmological promise, however, the CMB has proven a difficult instrumental challenge. The signals are faint, meaning even tiny amounts of instrumental noise can impede accurate measurements. Furthermore, there exist a range of astrophysical foregrounds that contaminate the base CMB.

Most of the astrophysical foregrounds come from material within our Galaxy. There is galactic synchrotron radiation, resulting from the motion of electrons in the galactic magnetic field. Due to the relatively low average field strengths present in the galaxy, this component affects lower frequencies. It is dominant at frequencies below 70 GHz. Thermal emission from interstellar dust is another significant foreground contaminant. This dust varies across the sky, depending on the dust grain size and temperature, and is the dominant foreground component at high frequencies (above 100 GHz). There are additional foreground contributions from electron-ion scattering (often referred to as free-free emission, or bremsstrahlung) and spinning dust, but these are unpolarized and subdominant to other foreground sources [3].

There are also atmospheric effects due to absorption lines from atmospheric components such as oxygen (around 60 and 120 GHz) and water vapor (around 20 and 180 GHz), as well as thermal emission from the atmosphere as a whole. These combine with the astrophysical foregrounds to make accurate measurement of the CMB a challenging endeavor [3].

Fortunately, these signal contaminants have characteristics that can be exploited to disentangle them from the CMB. In the case of atmospheric effects, many of the features (particularly emission lines) are spectrally well-localized, meaning they can be excluded from the instrument through careful choice of observing bands and filtering. In the case of astrophysical foregrounds, the task is rather more difficult but still tractable. The different foreground components have differing spectral shape, with none of them sharing the characteristic blackbody of the CMB. This means that by measuring the sky at a range of frequencies, estimates for the foregrounds can be generated. These foreground models can then be propagated to the primary CMB observing bands, and their contributions subtracted. This allows for foreground cleaning of the CMB, which serves to improve our measurements of it. Figure 1.13 shows the brightness of various foreground components in comparison to the CMB.

There are numerous projects deployed or in development that promise to improve these measurements dramatically, leading to better constraints on cosmological parameters and a better understanding of the dynamics of the universe at its largest scales and earliest times.

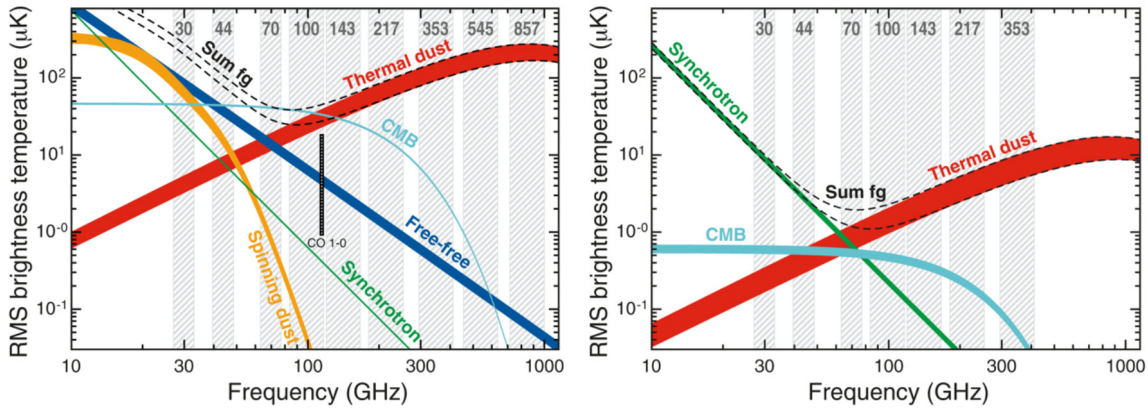

Figure 1.13: The spectral dependence of various CMB foreground signals. The left panel shows foregrounds in the temperature signal, and the right panel shows foregrounds in polarization. The combined foregrounds are of comparable or greater brightness than the CMB, and pose a significant challenge to accurately observing CMB anisotropies. A number of observing bands for the Planck satellite are called out on these plots. By observing at multiple frequencies, the foreground contributions can be estimated and subtracted, revealing the CMB underneath. Figure courtesy of the Planck collaboration [5].

1.2.4 Overview of This Thesis

This thesis covers the development of several technologies in support of the Atacama Cosmology Telescope Polarization project (ACTPol) [47], a polarization sensitive camera on a telescope in northern Chile. These technologies also support future CMB experiments by expanding the envelope of available capabilities and improving the overall efficiency possible in millimeter-wave cameras. Chapter 2 gives an overview of the telescope and instrument, providing the motivation for the technology development work being discussed. Chapter 3 gives an overview of metamaterial silicon optics for millimeter-wave imaging, and Chapter 4 discusses the development of fabrication capability for these structures. Chapter 5 extends the concept of metamaterial silicon optics to novel infrared blocking filters built on metamaterial silicon substrates. Chapter 6 shifts to discuss real-space CMB simulation work in service of understanding current experimental data and forecasting next-generation projects, with a focus on the Sunyaev-Zel'dovich effect and weak gravitational lensing, and Chapter 7 provides concluding remarks.

Chapter 2

The Atacama Cosmology Telescope and the ACTPol Instrument

The Atacama Cosmology Telescope (ACT) is a millimeter-wave telescope on Cerro Toco, a peak in the Atacama desert in northern Chile (see Figure 2.1 for location details). The ACT project and subsequent ACTPol and Advanced ACTPol (AdvACT) polarization projects map large portions of the CMB sky at arcminute scales in an effort to constrain cosmological parameters and provide measurements of secondary CMB effects such as gravitational lensing and the Sunyaev-Zel'dovich effect introduced by galaxy clusters [45, 47, 6].

The telescope is located at an elevation of 5190m (just over 17,000 ft., see Figure 2.2 for a photograph of the telescope site), where the high elevation and low atmospheric water content (measurable in the form of precipitable water vapor, or PWV, and one of the major sources of atmospheric noise for millimeter and submillimeter observations) enable sensitive observations of the mm-wave sky [45]. Additionally, the latitude of 23° S gives access to more than half of the sky and overlap with a number of large surveys covering different spectral regions (including optical, infrared, and X-ray surveys by a variety of different projects [47]).

This chapter provides an overview of the ACT and ACTPol experiments, setting the stage for the technology development work done in later chapters. The ACTPol lenses drove the development of metamaterial silicon anti-reflection surfaces (Chapters 3 and 4), the need for improved filtering motivated the infrared filter development work (Chapter 5), and current CMB weak lensing work motivated the development of improved real-space CMB simulations (Chapter 6).

Figure 2.1: The location of the Atacama Cosmology Telescope (top panels), with the aerial picture of the site itself (bottom panel). The telescope structure is clearly visible. Maps and imagery obtained from Google Maps.

2.1 Telescope Overview

The Atacama Cosmology Telescope is an off-axis Gregorian telescope with a 6m primary mirror and 2m secondary mirror. It was designed to have arcminute-resolution at the main CMB observing frequencies [48], setting the primary mirror size. The optical configuration and telescope structure were designed to be compact (with a short 5.2 primary focal length) to enable fast scanning of the telescope across the sky [45] (see Figures 2.3 and 2.4 for a photograph and schematic view of the telescope and its optical configuration).

Figure 2.2: The Atacama Cosmology Telescope site, with the stationary groundscreen visible on the left, various site structures in the center, and Cerro Toco visible in the background on the right.

Light, reflected off the secondary mirror of the Atacama Cosmology Telescope, passes through silicon reimaging optics, and is coupled by feedhorns onto the three detector arrays. The pixels precisely measure deposited power in a range of frequency bands from 90 to 220 GHz, which are primary observing bands for microwave cosmology (and were selected to maximize the CMB signal while avoiding absorption bands from atmospheric absorption lines from water vapor and oxygen). These detectors enable precision measurements of the temperature and polarization fluctuations imprinted in the CMB, and through them, offer a window into physics at the earliest times and largest scales.

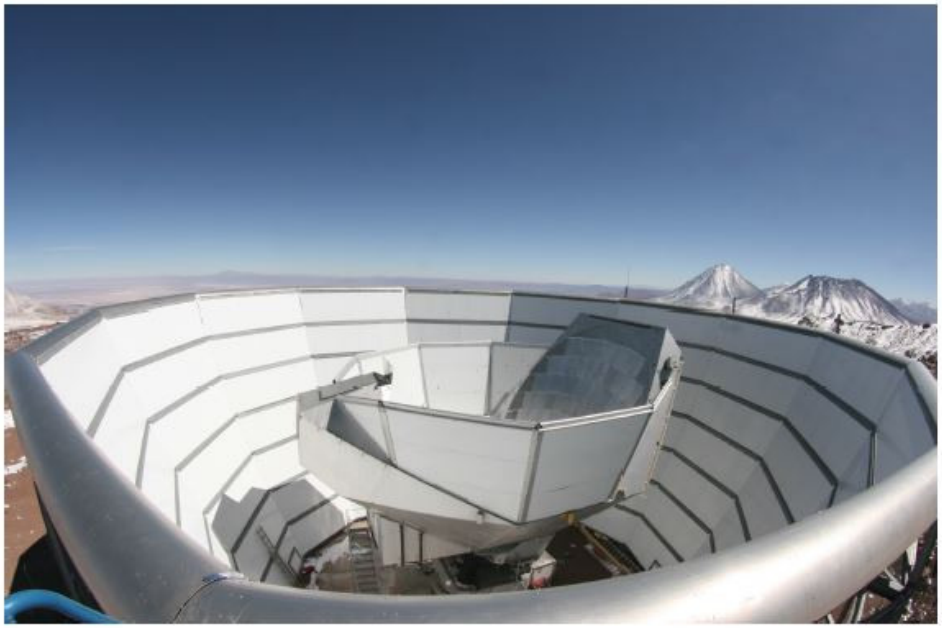

Figure 2.3: The Atacama Cosmology Telescope from the top of the stationary groundscreen. Visible in the center is the telescope structure, with the primary mirror at the right, and the secondary at the left (but hidden behind the comoving groundscreen). It is 12m from the ground to the top of the telescope. Figure courtesy of the ACT collaboration.

2.2 Science Goals

The Atacama Cosmology Telescope made improved measurements of the CMB temperature anisotropy spectrum at arcminute angular scales [49], and provided detections of clusters in the CMB sky via the Sunyaev-Zel'dovich effect [50], and the ACTPol project aims to improve upon these measurements while adding measurement of the CMB polarization anisotropies through the addition of polarization-sensitive receivers [47].

2.3 ACTPol System overview

ACTPol is a polarization sensitive receiver for the Atacama Cosmology Telescope (ACT) which aims to make precise observations of the polarization of the Cosmic Microwave Background (CMB). Through these, it will provide a detailed probe into the energy scale of inflation through measurement of large-angular-scale features, give improved constraints on the sum of neutrino masses through gravitational lensing, and shed light on the characteristics of early dark energy [47]. Improved sensitivity and

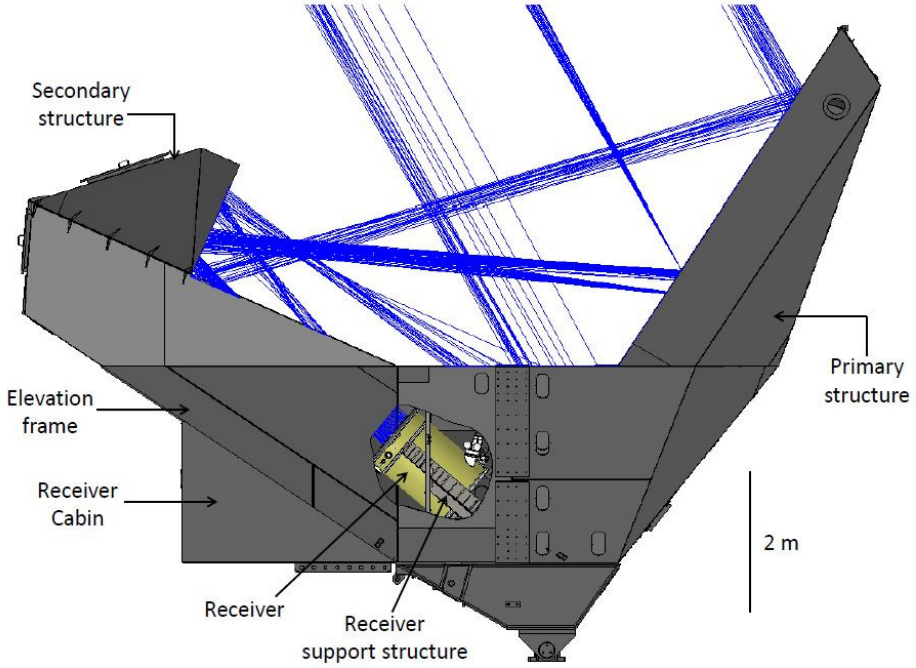

Figure 2.4: A ray tracing schematic of ACT. Light from the sky falls on the primary mirror, is focused down towards the secondary, which focuses it into the receiver. The receiver cryostat contains the reimaging optics, filters, and feedhorns necessary to couple the light onto the planar detector arrays, where it is absorbed and measured. The entire structure shown (mirrors, receiver cabin, frame, and groundscreen), move together as the telescope sweeps across the sky. Figure courtesy of the ACTPol collaboration [6].

the addition of polarization measurements enable significant progress towards these goals and improvement over the previous instrument. The ACTPol receiver consists of three feedhorn-coupled detector arrays coupled to the telescope via diffraction-limited optical paths populated by free-space filters and silicon lenses [48]. Two arrays are single-frequency detectors in the 150 GHz band while the third is an array of multichroics covering the 90 and 150 GHz bands. These multichroic detectors, which allow for simultaneous, high-sensitivity measurements in two frequency bands, offer a promising avenue for further improving the total sensitivity of CMB experiments through more efficient usage of limited focal plane area.

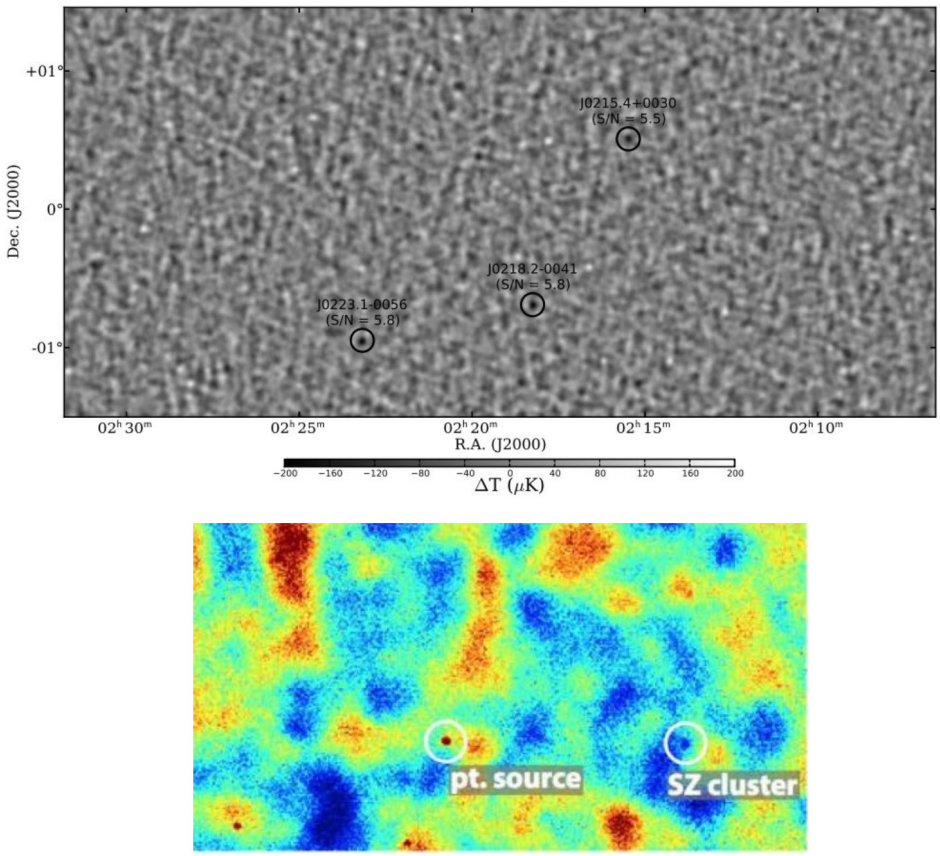

Figure 2.5: Galaxy clusters appear in the ACT (top) [7] and ACTPol maps (bottom) [8] as cold spots in the CMB. The ACT map (from the 148 GHz observing band) has been processed to remove point sources, and matched filtered, with high signal-to-noise objects called out. The ACTPol map (also from the 148 GHz band), has not had this processing, with a point source and SZ cluster called out. Figures generated by their respective authors.

2.4 Detector Arrays

As part of the ACTPol project, an array of dual-frequency detectors were developed, covering the 90 and 150 GHz observing bands simultaneously. These multichroic detectors allow for simultaneous measurement of two frequency bands with a given pixel and offer a promising avenue for improving CMB polarization measurements by increasing the total efficiency of a given focal plane area [51] up to 70% over a single-frequency array [52].

The multichroic array for ACT is composed of an array of 255 ring loaded corrugated feed horns fabricated from gold plated stacked silicon wafers (see Figure 2.7 for a discussion of the feedhorns) coupled to 255 multichroic polarimeters arrayed in 3

hex and 3 semi-hex tiles (see the left panel of Figure 2.6 for a diagram of the array). This array is optimized with the constraint of a 1024 channel readout and, accounting for dielectric losses in the detector achieves 1.3x the mapping speed of a single frequency array. Greater gains are possible in the future with an array optimized to maximize the mapping speed unconstrained by our existing readout.

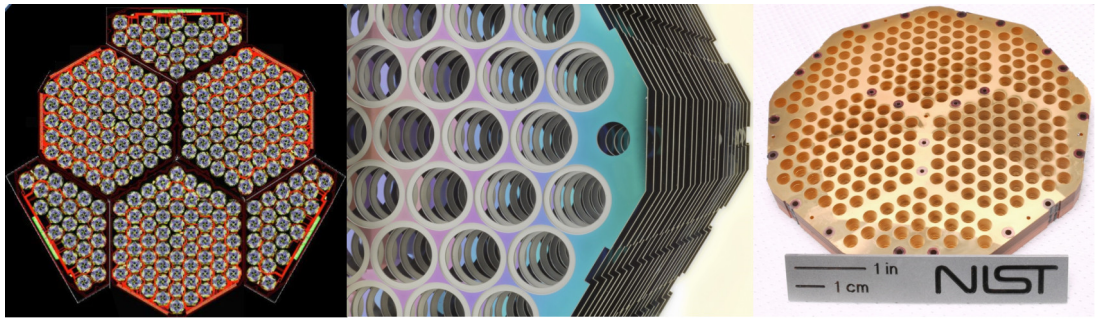

Figure 2.6: Left: A schematic diagram of the layout of the entire array, consisting of three hexagonal wafers tiled with three "semi-hex" wafers as required to fabricate the array on the 3" capacity machine being used by NIST. Center: The stack of individual etched silicon wafers forming the stacked platelet feedhorn assembly. Right: The full feedhorn assembly after being stacked and gold plated, in its final configuration for deployment. Figures courtesy of the ACTPol collaboration.

Light passes through one of these corrugated feedhorns and falls onto the orthomode transducer (OMT) in the center of the detector. The feedhorns serve to impedance match radiation from the free-space in the optics tube to the detector wafers, and are optimized to provide a suitable bandwidth for the multichroic detectors. A pair of opposing fins in the OMT couple to a linear polarization (the signal path for 150GHz, vertical polarization is highlighted in blue in the figure at right). The signal passes through a transition from coplanar waveguide (CPW) to microstrip (MS), then into a diplexer which splits the 90 and 150 GHz components using resonant stub filters. The passed signal gets run through a hybrid tee, which produces a sum and difference at the two output ports. The summing port is terminated on lossy gold, while the difference port (which passes the desired TE11 mode) is terminated on a transition edge sensor (TES) bolometer. These TES bolometers are then read out by a time-domain multiplexing system consisting of three stages of squid amplification, which is in turn read out by non-cryogenic readout electronics [6] (See the top panel of Figure 2.8 for an overview of a multichroic pixel).

Single multichroic pixels were thoroughly characterized using a Fourier Transform Spectrometer (FTS) to measure their passbands and rejection of undesirable modes. The 90 and 150 GHz bands respectively showed 65% and 50% total optical efficiencies

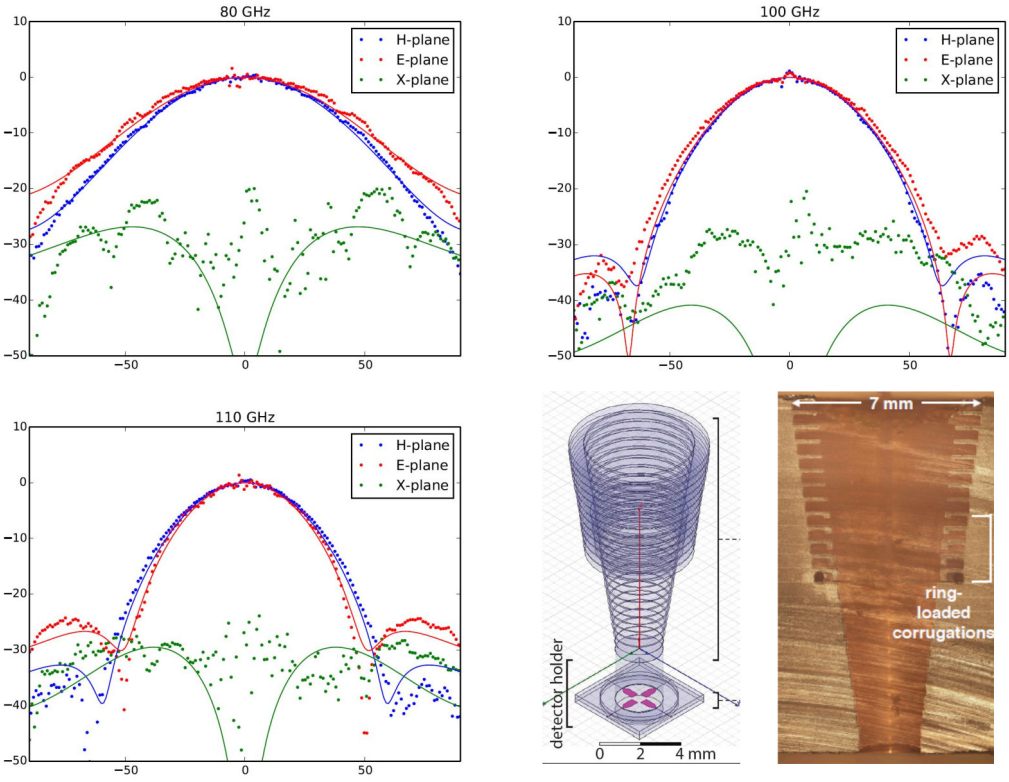

Figure 2.7: The ring-loaded stacked platelet construction of feedhorns for the ACTPol project. These feedhorns were optimized to provide symmetric beams, low sidelobes, and low cross-polarization, while maintaining the wide bandwidth necessary to enable the use of multichroic detectors. The upper panels and lower left panel show the feedhorn beams in two polarizations (red and blue) and in cross-polarization (green) for both measured (points) and simulated (lines) performance, showing beams that are symmetric and well-shaped across the necessary range of incidence angles and frequencies (for the 90 GHz band for these particular measuremnets). The lower right panel shows a model of the full feedhorn geometry and a cross-section of a completed feedhorn, in which the complex ring-loaded structure can be seen. This structure serves to improve the bandwidth over which the horn gives acceptable performance. Figure components courtesy of the ACTPol collaboration.

when measured in a cryogenic test setup (including ∼10% loss inherent in the test setup). These values are consistent with efficiency estimates derived from dielectric losses in the planar circuits (see the lower panel of Figure 2.8 for the performance of a prototype multichroic pixel) [9].

The first multichroic array was successfully deployed on ACTPol in 2014, marking the first deployment of a multi-frequency pixel on a CMB experiment and the completion of the ACTPol project deployment.

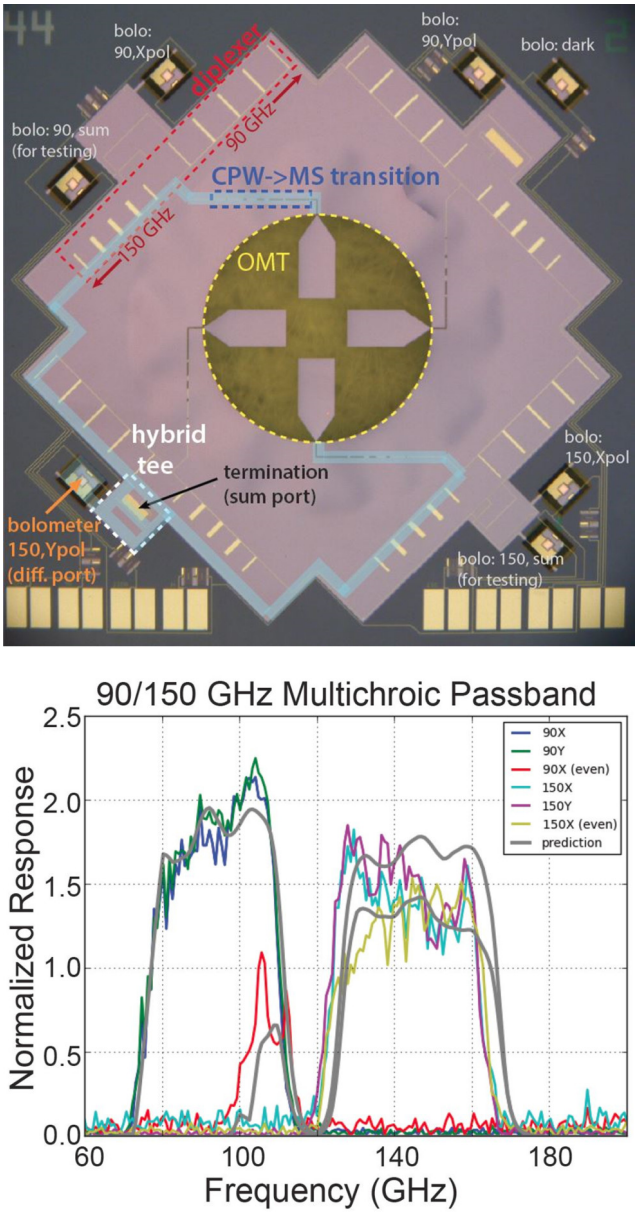

Figure 2.8: Top: an image of a prototype 90/150 GHz multichroic pixel. Light falling onto the orthomode transducer (OMT) fins in the center gives rise to a signal propagating along the planar circuit transmission lines. The 90 and 150 GHz bands are split with a diplexer, and the components from opposing fins are interfered to get the odd mode (the odd mode corresponds to the desired signal that makes it through the wavequide feeding into the pixel). This signal is then terminated on a transition edge bolometer (TES), where the deposited power is measured. Bottom: The measured passband of one of these pixel prototypes, showing good agreement with prediction (with a small shift in the lower band edge of the 150 GHz band). Figure components courtesy of Rahul Datta. [9]

Two single-frequency arrays at 150 GHz were also deployed as in the first stages of the ACTpol project, with a similar detector layout to the multi-chroics, but lacking the diplexer and filter components necessary to separate the two frequency channels.

2.5 Silicon Optics

The Gregorian focus of the telescope is reimaged onto the three detector arrays by a set of three independent optics tubes containing cryogenic refractive optics and free-space filters. The refractive optics are designed to maximize the optical throughput in order to maximize the total instrument sensitivity [6]. The reimaging lenses are composed of single-crystal silicon, offering low loss and high throughput when properly treated to reduce reflections. The metamaterial anti-reflection surface treatment technique used is discussed later in this thesis, and is one of my main contributions to the project.

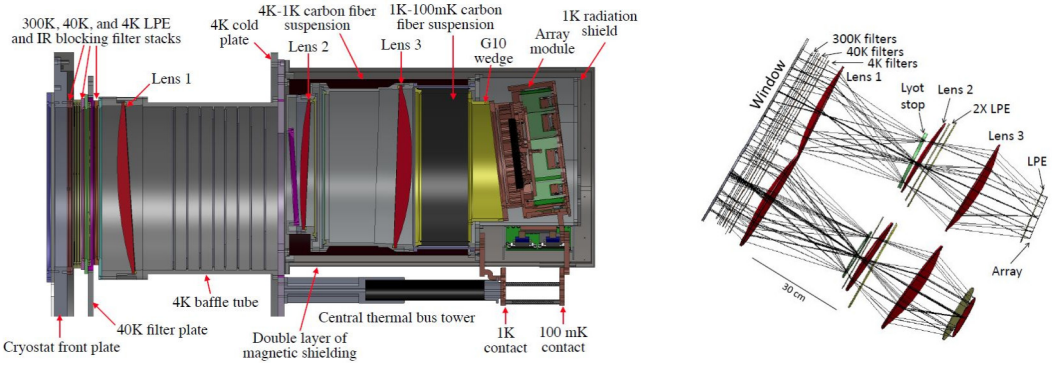

Figure 2.9: Left: a CAD model of one of the optics tubes, showing the assorted filters, lenses, and cryogenic components needed for the detector array (held in the array module at the right end) to properly function. Right: A ray-tracing diagram of two of the ACTPol optics tubes, showing the path taken from the window (at the top left, which points towards the telescope secondary mirror) to the detector array (bottom right). Figures courtesy of the ACTPol collaboration [6].

2.6 ACTPol Results

The ACTPol project has produced successful measurements of the CMB temperature and polarization over several seasons, with final science results from the first season of observing time. The results from the first observing season generated maps with noise between 11 and 17μK-arcmin covering a total area of 270 square degrees, and

yielding an excellent fit to existing best-fit cosmological model parameters derived from other experiments.[10] (See Figure 2.10 for the power spectra resulting from this analysis. Data from further observing time have been accumulated and results are forthcoming.

It has also provided evidence for the kinematic Sunyaev-Zel'dovich effect through combination with measurements from the Baryon Oscillation Spectroscopic Survey (BOSS) experiment, [53] evidence for lensing of the CMB by dark matter halos revealed by stacking on optically-selected galaxies[54], and a statistical measurement of lensing of the CMB through cross-correlation with the Cosmic Infrared Background (CIB)[55]. and even constraints on the upper limit of the sum of neutrino masses.

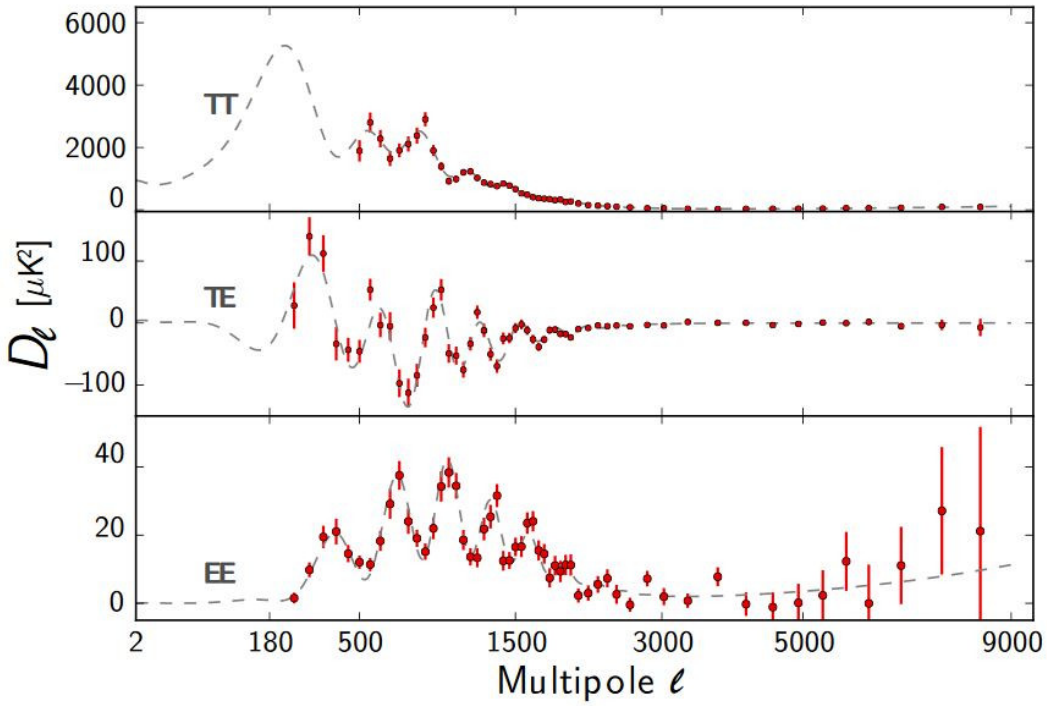

Figure 2.10: The ACTpol TT, TE, and EE power spectra, together with the best fitting ΛCDM cosmological model and foreground components. Figure from [10].

The additional observing data for two more seasons, with more arrays and greater total sensitivity, have been collected, and promises further exciting scientific results, including improved constraints on the sum of neutrino masses [56], better constraints on fundamental cosmological parameters, and improved mapping of large scale structure through detailed lensing and SZ measurements.

2.7 Advanced ACTPol

The next upgrade to the ACT telescope, called the Advanced ACTPol project, is funded and already underway. This upgrade will extend the scope of the original ACTPol project, increasing the sky coverage to give overlap of the entire Large Synoptic Survey Telescope (LSST) survey [1], expanding to additional frequency bands, giving coverage from 25 to 280 GHz over five different spectral bands, and give sufficient sky coverage and sensitivity to to search for both large-angular-scale effects (such as B-modes resulting from gravitational waves during inflation) and small-angular-scale effects (such as the SZ effect) across a large portion of the sky [57].

Advanced ACTPol will feature improved multichroic detector arrays, new readout electronics, and continuously-rotating metamaterial silicon half-wave plates, enabling the push to better sensitivity, greater spectral coverage, and improved large-angular-scale measurements [58]. This will enable the next generation of CMB science, including improved measurements of primordial B-modes, lensing, and the SZ effect, and will better probe the primordial CMB power spectrum and the epoch or reionization [59].

[1] www.lsst.org

Chapter 3

Metamaterial Silicon Optics

Increasing size and sensitivity for cryogenic millimeter and sub-millimeter wavelength detector arrays place increased demands on the optical assemblies feeding into the detectors. One specific requirement is for improved transmissive optical elements, such as the lenses (and filters) used in the ACTPol project. For lenses used in large-scale millimeter cameras, silicon offers an excellent material for these applications. Silicon has a high thermal conductivity and refractive index, and low loss in the millimeter and sub-millimeter regions of the electromagnetic spectrum, all of which make it an attractive material foe millimeter-wave optics. Its high refractive index poses a challenge in anti-reflection coating to maximize throughput, however, particularly in the context of large-diameter, cryogenic optics. In this chapter, I will describe silicon as a millimeter-wave optical material and the background and design of metamaterial anti-reflection surfaces (consisting of machined sub-wavelength features) on large-diameter single-crystal silicon lenses. These lens coatings were manufactured for the ACTPol project, in order to improve the overall sensitivity of the instrument and enable the deployment of broader-bandwidth detectors.

3.1 Silicon as a Material for Millimeter Wave Optics

Single-crystal silicon is a ubiquitous material in the fabrication of electronic devices. It can be purchased in large boules up to 460 mm in diameter[60] and with excellent purity and high resistivity. Figure 3.1 shows a photograph of a single-crystal boule of silicon.

With the exception of two narrow lattice absorption features at $\sim$15 and 16μm,

Figure 3.1: A single-crystal boule of silicon. Boules like this are generated by pulling molten silicon using a seed crystal (either via float zone or Czochralski processes, depending on desired size and required purity - Czochralski achieving larger sizes, but introducing oxygen impurities due to the silica crucibles used in processing). Image used under the creative commons license [11].

silicon has low dielectric loss from approximately 1μm to several mm wavelengths, making it suitably transmissive for refractive optics. In mm and sub-mm wavelengths, it has particularly low loss, with a measured loss tangent as low as 4x10^{-5} [61]. Additional measurements in support of developing silicon optics for the ACTPol project support this value, with an upper limit on loss tangent being measured at 7x10^{-5} [13].

Additionally, silicon has a high thermal conductivity [62], making it easy to cool (compared to plastics and other lower-conductivity materials) and thus an attractive material for cryogenic applications like the ACTPol project (where cooled optics reduce thermal emission onto the detectors). High thermal conductivity also makes it an attractive substrate for filters, where any absorbed power adds a source of heating, and can therefore lead to increased thermal emission without efficient heat removal.

3.2 Metamaterial Surfaces for Impedance Matching

The traditional approach to managing reflections at material interfaces is to create a stack of materials with intermediate refractive indices and specific thicknesses, such that the reflections off the surface interfaces cancel (or nearly cancel, in the case of broader bandwidth coatings). For traditional optical systems, these are usually thin

film coatings deposited on the optical surfaces.

Millimeter-wavelength systems impose the requirement of thicker layers than traditional visible-light optics (as the thicknesses scale with the wavelength of the desired pass-band), and the cryogenic environment present in bolometric detector cameras like ACTPol imposes the requirement that any anti-reflection coating be compatible with the silicon substrate under repeated temperature cycles spanning ∼300K. This means that the material must be a suitable match in both refractive index and coefficient of thermal expansion so as to not break or delaminate under the stresses induced by the transition from room temperature (where the optics are assembled) to temperatures as low as 4K (the operating environment for the coldest set of lenses in their steady-state on the telescope). Additionally, any material used in the optical path must be low-loss in millimeter wavelengths, ruling out many plastics and other coating materials. Plastics such as Cirlex (a Polyimide polymer sheet material [1]) have been used in previous millimeter-wavelength cameras [63], but introduce significant loss (in the case of the ACT project, loss at a level of approximately 15% per optics tube) through a multi-lens optical assembly, both due to reflection from the interfaces and attenuation in the material [45].

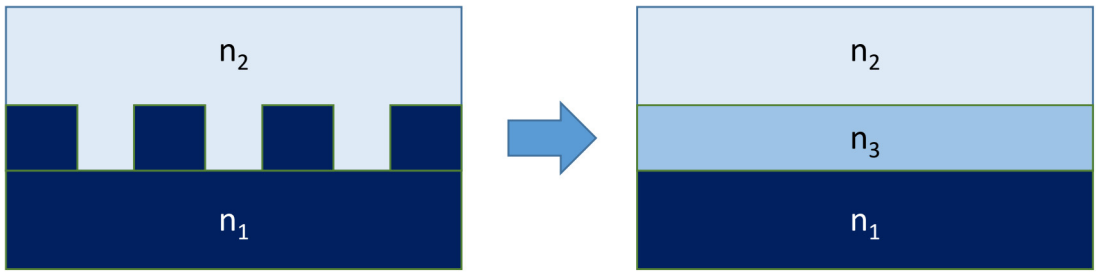

Figure 3.2: Left, a diagram of a surface structured with sub-wavelength features. Right, an electromagnetically equivalent structure consisting of three layers of different indices. The center "layer" is an effective index and thickness equivalent to the structured surface at left, where the features are averaged out by virtue of their small size compared to a wavelength [12]. For the ACTPol lenses, n_1 is the index of silicon (approximately 3.4) and n_2 is the index of vacuum.

An alternative approach to a traditional anti-reflection coating is the fabrication of layered meta-material structures, such as sub-wavelength holes [64], posts, or grooves [65], patterned into the substrate surface. By removing material at length scales much smaller than a wavelength, a substrate-vacuum meta-material can be created, with an effective refractive index between that of vacuum and the substrate, and dependent on

[1] www.cirlex.com

the geometry of the structured surface [12] [66]. These behave like dielectric layers but are fabricated from the same base material as the rest of the optic. Multiple layers of these meta-material structures can be used to create a number of intermediate indices and form a broad-band anti-reflective surface. Figure 3.2 shows a schematic of this concept.

These structures can also be non-uniform to create flat lenses and other novel optical behavior, characteristics that have been demonstrated before at THz frequencies [67].

3.3 Design of Metamaterial Anti-reflection surfaces for the ACTPol project

For the ACTpol project, anti-reflection metamaterial surface features were designed to reduce reflections through the silicon optics. These were designed using a multi-step process, ending with a final optimization of the structures using the measured dimensions from the actual fabrication process, and resulting in very low reflection (<1% per optic) lenses. The individual unit cell of the metamaterial structure is a pillar of stacked rectangular prisms (with square cross-sections in the plane of the surface), formed by cutting layers of nested cuts in perpendicular directions. These structures were chosen for their polarization-symmetric behavior [68] and for the ability to form them by a set of known machining operations.

The overall design process for ACTpol metamaterial surfaces was as follows:

1. An antireflection coating was designed via an analytic model consisting of layered sheets of dielectric material stacked on the silicon substrate. These layers each had a thickness and index of refraction that were varied to minimize reflectance across the desired transmission band. This gave target optical thicknesses and indices for the complete structure.

2. Each layer of the layered dielectric model was translated into a pitch, kerf, and depth for the cut surface geometry. This translation was done via a model developed by simulating pillar structures in Ansys HFSS (formerly High Frequency Structure Simulator) [69] over a large range of parameters, then fitting an analytic model to the results. These structures were simulated with periodic boundary conditions, giving results for an infinite 2-dimensional array of structures, a good approximation to the repeating pattern structured on an optic surface. See Figure 3.3.

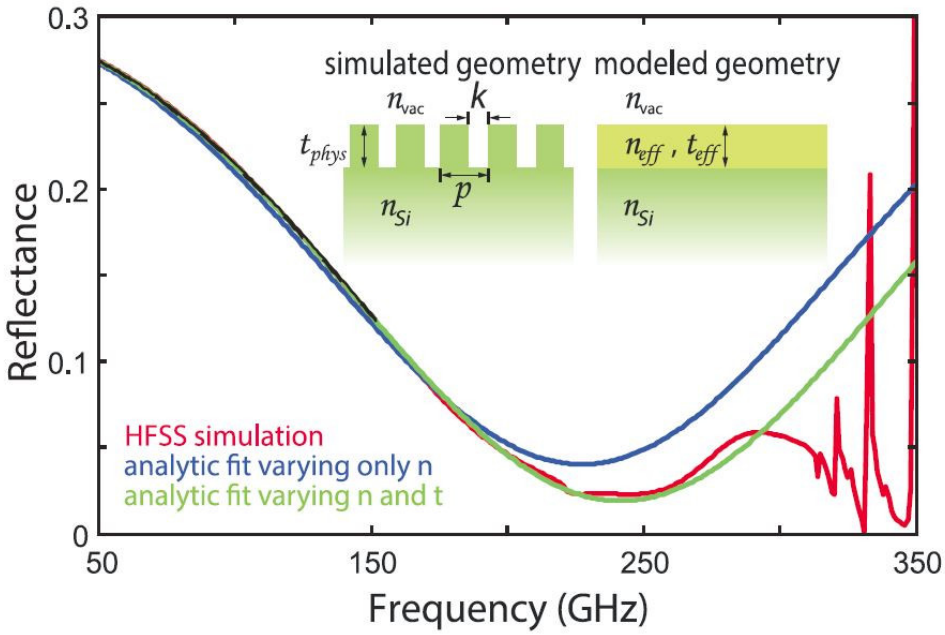

Figure 3.3: A comparison of the surface reflectance determined by an HFSS simulation of a pillar geometry compared to fits based on an equivalent layered dielectric model. This shows good agreement below the breakdown frequency, at which the structures no longer behave as a simple dielectric layer. Figure courtesy of Rahul Datta [13].

3. A multi-layer structure was modeled in HFSS based on the single-layer target characteristics, and optimized to minimize the reflections in the desired band. See Figure 3.4 for the geometry of these structures.

4. Cuts were made in silicon samples and the detailed cut geometry was measured. This gave an accurate representation of the as-fabricated pillar shapes, which was fed back into the model and re-optimized. This ensured better performance and improved the fidelity of the model as a representation of the structures as-fabricated. See Figure 3.5 for a modeled geometry as fabricated, and the predicted performance of this geometry.

5. The optimized structures were machined into the optic using a custom-built machining system. The following chapter covers my work designing, developing, and using this system and its performance in fabricating optics for ACTPol.

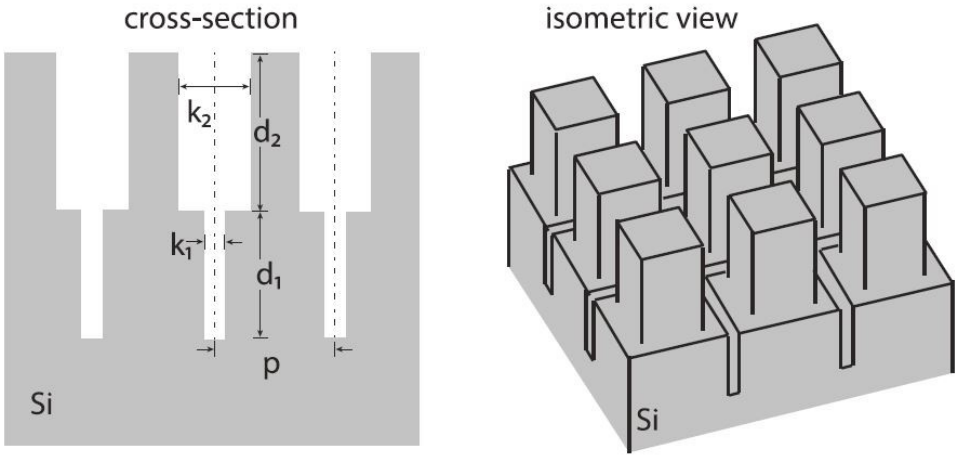

Figure 3.4: The modeled geometry for a 2-layer structured surface. Left, the cross section, showing the kerfs and depths of the two cut layers, and the period of the repeating structure. Right, an isometric view of a section of these structures. This geometry was modeled in HFSS to determine the dimensions needed to maximize performance. Figure courtesy of Rahul Datta [13].

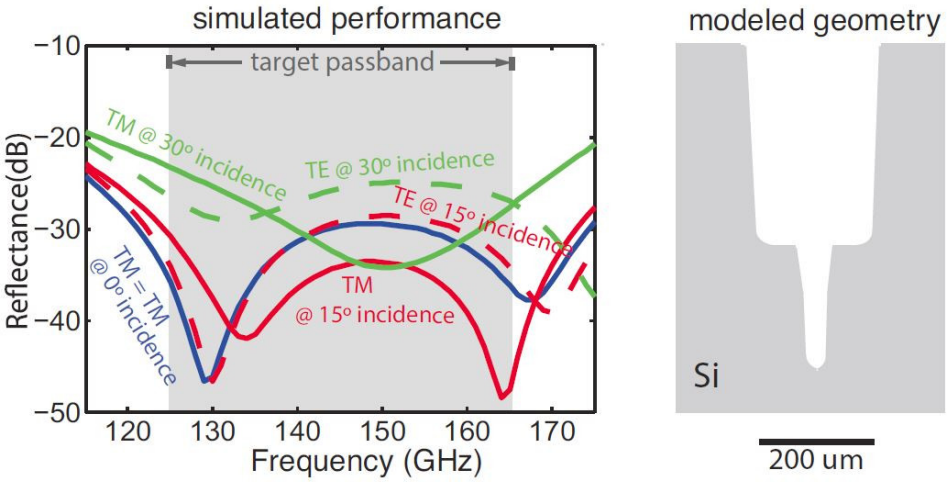

Figure 3.5: Left, the simulated performance of a 2-layer structured surface at several different angles of incidence. Right, a cross section of the modeled geometry that produced this performance. This modeled geometry took into account the measured profile of a set of cuts (note the rounding of the cut edges and tapering sidewalls), giving an accurate representation of the expected final geometry and improved simulation fidelity relative to a model not accounting for these features. Figure courtesy of Rahul Datta [13].

Chapter 4

A Custom Machine for Fabricating Metamaterial Silicon Surfaces

In order to fabricate these subwavelength features (referred to within the ACT community as antireflection coatings, and referred to here as metamaterial anti-reflection surfaces - or MARSs) on the silicon lenses for the ACTPol project, a custom piece of machining equipment needed to be designed and constructed. This chapter details the design, construction, integration, and testing of this equipment, including the measured performance of optics produced with it. These optics were critical for the deployment of ACT, and will be an important technology for the next generation of CMB observatories. Additionally, this technology provided the groundwork for the development of improved infrared blocking free-space filters (discussed in Chapter 5).

The basic machine consisted of a high-precision computer numeric controlled (CNC) gantry with a high-speed dicing spindle (an abrasive saw used in semiconductor manufacturing) attached. Fabricating the anti-reflection structures requires average cut depth precision of approximately 5 microns across the surface of the 30+ cm diameter lens (or better, for higher frequency coatings), which in turn requires the ability to accurately locate the lens surface, make repeatable and accurately placed cuts at better than this tolerance, and verify the absolute and relative placement of different cuts (as well as cut geometries) to ensure proper function of the resulting optics. This set of requirements necessitated a complex machine and operating procedure to ensure the necessary

precision, performance of the finished optics, and 100% yield rate necessitated by the expense and difficulty in obtaining replacement silicon. On the platform of the gantry and dicing spindle, supplemental systems were needed to make precision measurements of the silicon substrates, handle the flood cooling necessary to ensure consistent and reliable cutting, maintain a consistent temperature to prevent calibration drifts due to thermal expansion, and provide the necessary control, monitoring, compressed air, and power to the complete system. Figure 4.1 shows a CAD model of the entire system, and Figure 4.2 shows the assembled system during early performance tests.

This work enabled the successful (and on time) deployment of the second and third detector arrays on the ACTPol project, enabled the first deployment of a multichroic detector array on a CMB experiment, and enabled the successful development of the next generation AdvACT experiment (now funded and partially deployed). This work has also enabled the development of novel silicon waveplates, and will be an instrumental technology in the future of CMB experiments (including the future ground-based CMB-S4 experiment).

4.1 The Gantry

In order to achieve the initial precision requirements, a gantry with repeatability better than 5 microns was required. A gantry system was ordered from Aerotech Inc., with a specified repeatability of 2.5 microns over the 600mmx600mmx100mm movement volume. This amount of travel was chosen to accommodate the largest silicon boule diameter currently available (45 cm) held in the fixtures necessary to reliably locate and rotate the optic to the desired machining positions. Due to the sizeable body of the spindle and modest blade exposures allotted by dicing saw components (necessitated by the high rotational speeds used in silicon dicing), only half of a typically curved lens side could be cut in a single pass. This meant that cutting a single direction of cuts across a curved lens surface required two independent setups, and precision fixturing to facilitate this. A discussion of this fixturing is present in 4.7. The motion control system, stages, granite block, and mounting fixture for the dicing spindle were provided by Aerotech, including the initial alignment and verification of gantry performance. In the verification provided by Aerotech, the gantry system provided repeatability of 1 micron, exceeding the necessary specifications. The

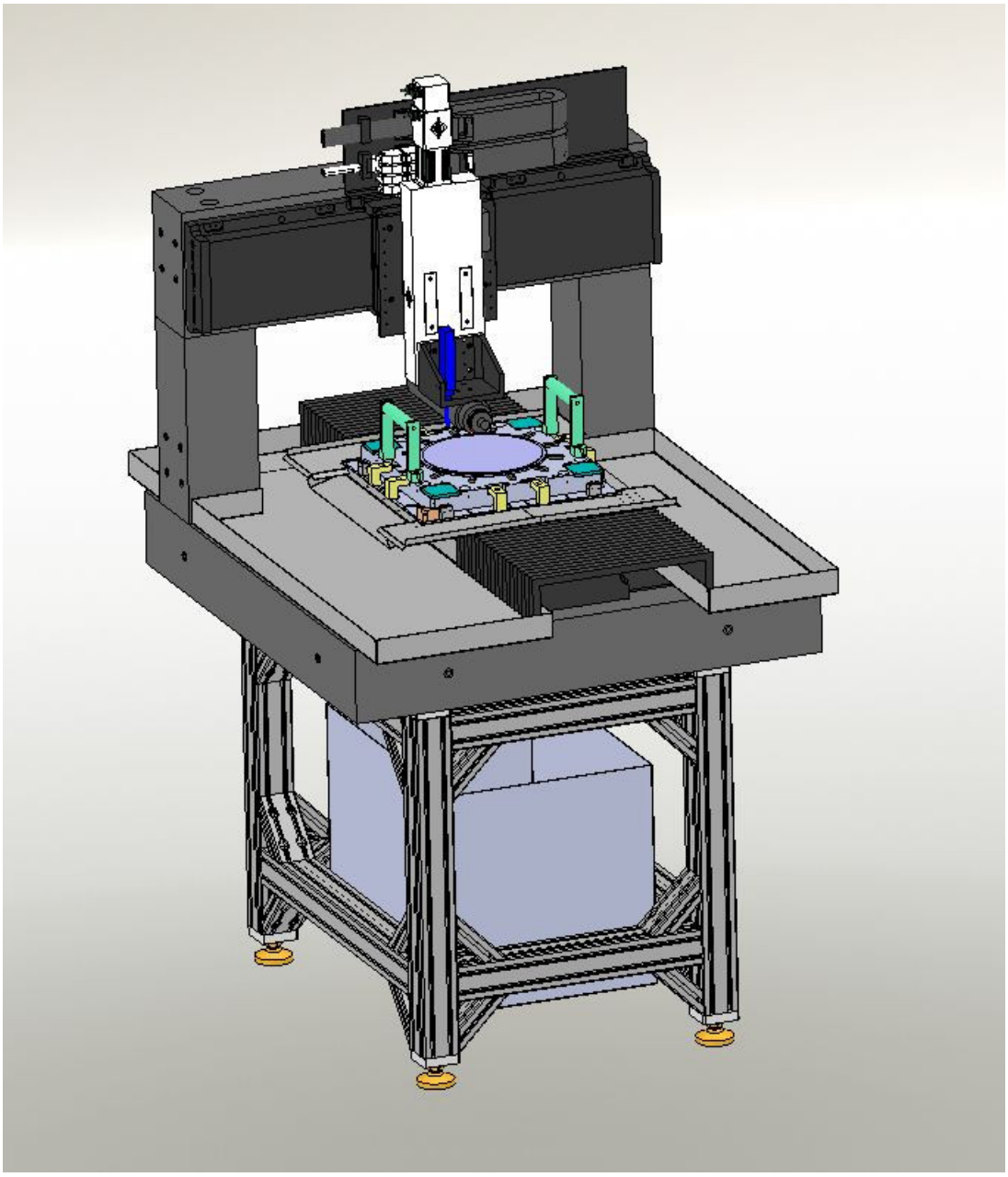

Figure 4.1: A CAD model of the complete dicing system, including table, stages, lens fixturing, and mounting for the dicing spindle and linear gage.

end-to-end machining precision of the gantry was verified after integration of the entire system, and met the necessary specifications to produce antireflection coatings across all current and future bands of interest for the ACTPol instrument. The X and Y stages were both high-load linear motor stages, capable of moving the combined weight of the lens, fixturing, and water handling (for the X stage) and the Z stage, spindle, and flood cooling equipment (for the Y).

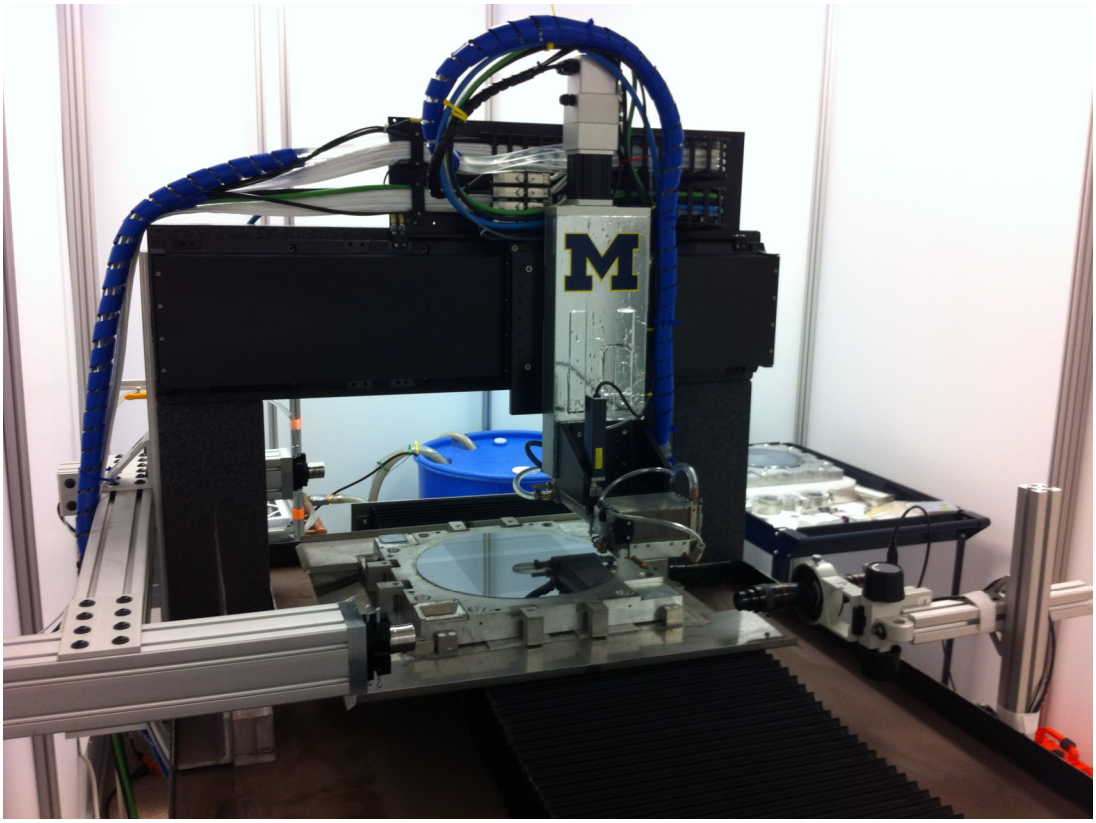

Figure 4.2: A photograph of the fully integrated dicing system, with a flat test piece mounted.

These stages were attached to a granite slab and bridge, and aligned so that the plane of the blade is vertical to within 40 arcseconds, and parallel to the travel of the Y stage (and therefore parallel to the cutting motion) to within 4.5 arcseconds [70]. This initial mounting and precision alignment was performed by Aerotech, and a remounting procedure has subsequently been developed. We designed a mounting interface for the spindle and measurement system, with input from Aerotech. This provided square mounting for the spindle to the Z stage, and allowed for mounting of the linear gage used as the measurement system. It additionally offered a grid of bolt holes to tie in any other parts that might be added in the future. This interface was then machined by Aerotech and integrated into the gantry system prior to delivery. This interface is visible in Figure 4.3 in black anodized aluminum above the spindle.

4.2 Flood Cooling and Blade Guard System

A flood cooling system was designed around the spindle, providing the necessary cooling flow to keep the blade cutting properly, provide lubrication for the cutting process, and remove the swarf generated by the cutting (this debris presents mostly as fine dust, and keeping the cutting submerged serves the dual purposes of keeping the blade clean and keeping the fine dust from becoming airborne, which would pose an inhalation hazard). This was surrounded by an enclosure to contain the spray from cooling water and dicing, as well as any debris generated by cutting or blade disintegration. The flood cooling system was originally designed to deliver approximately 2L/min of water, but this number was increased to 5L/min or greater to provide sufficient cooling and swarf removal at the full cutting speed of 25 mm/s. Figure 4.3 shows the flood cooling system in operation, and attached blade guard enclosure.

The system consists of a recirculating loop of water (along with KerfAid, a surfactant additive package designed for wafer dicing) that passes through a series of filters (to remove circulating silicon dust), and is forced through a set of nozzles around the blade enclosure. This water falls on the blade and workpiece, runs off (guided by a series of overlapping gutters), and drops into catch trays on the granite table on either side of the stage. These trays then drain back into the tank. The tank for this system is coupled, via a heat exchanger coil, to the room temperature control system (discussed in section 4.3). This ensures that the entire dicing system is kept at a uniform and stable temperature, preventing thermal drifts that would compromise its performance. An immersion pump circulates the cooling water through the loop, and its proximity to the heat exchanger ensures that the thermal disruption from its operation is minimal. Remote control of the flood cooling pump is handled by switching the pump power with a solid state relay controlled over ethernet by an Arduino microcontroller, and there is a flow switch present that halts cutting if the flood coolant flow drops below a threshold value.

4.3 Temperature Control System

The thermal stability of the enclosure and gantry were ensured by the construction of a temperature control system capable of maintaining $<0.5°C$ tem-

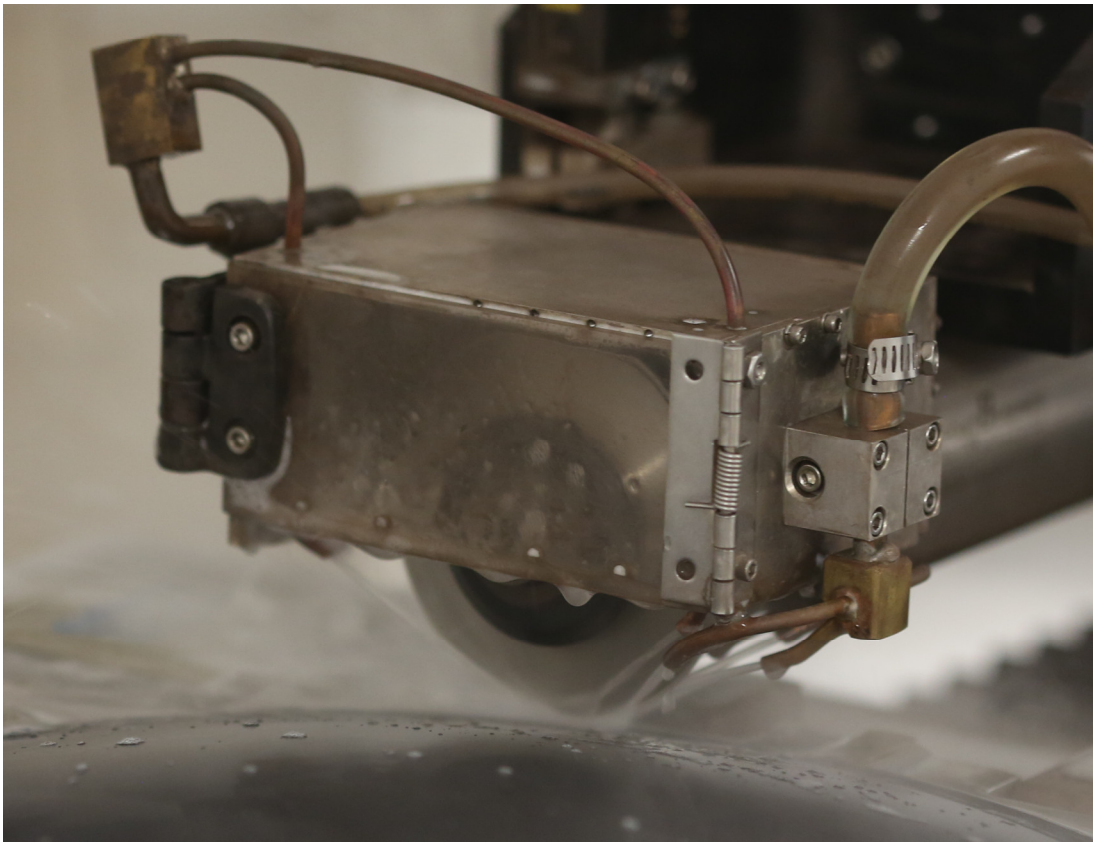

Figure 4.3: The blade guard and flood cooling system. The blade guard enclosure is constructed of machined aluminum plates, with a clear plexiglas front panel that opens to allow access for changing the blade. Nozzles direct the flood cooling water directly in line with the cutting, as well as onto the sides of the blade. This effectively removes the debris generated by cutting and keeps the blade material and substrate from heating excessively.

perature fluctuations. The lab, while typically controlled to $\sim 3°C$, is not sufficiently stable to grant the precision needed for fabricating metamaterial antireflection surfaces. To stabilize it further, an insulated enclosure was built around the AR coating machine, and a buffered temperature control system was created. This system consisted of a 55 gallon water tank, 3kW of immersion heaters, a heat exchanger to the building process chilled water, and a PID controller and temperature probe. This system was constructed and tuned to buffer against the temperature fluctuations in the building climate control and improve the stability of the environment directly surrounding the AR coating machine. This system reduced the temperature fluctuations by a factor of 3, providing the thermal stability necessary to achieve micron-precision machining. The temperature control performance was monitored with a temperature

logging system consisting of an Arduino microcontroller board and an LM35 integrated circuit temperature sensor. A typical set of temperature measurements are shown in Figure 4.4.

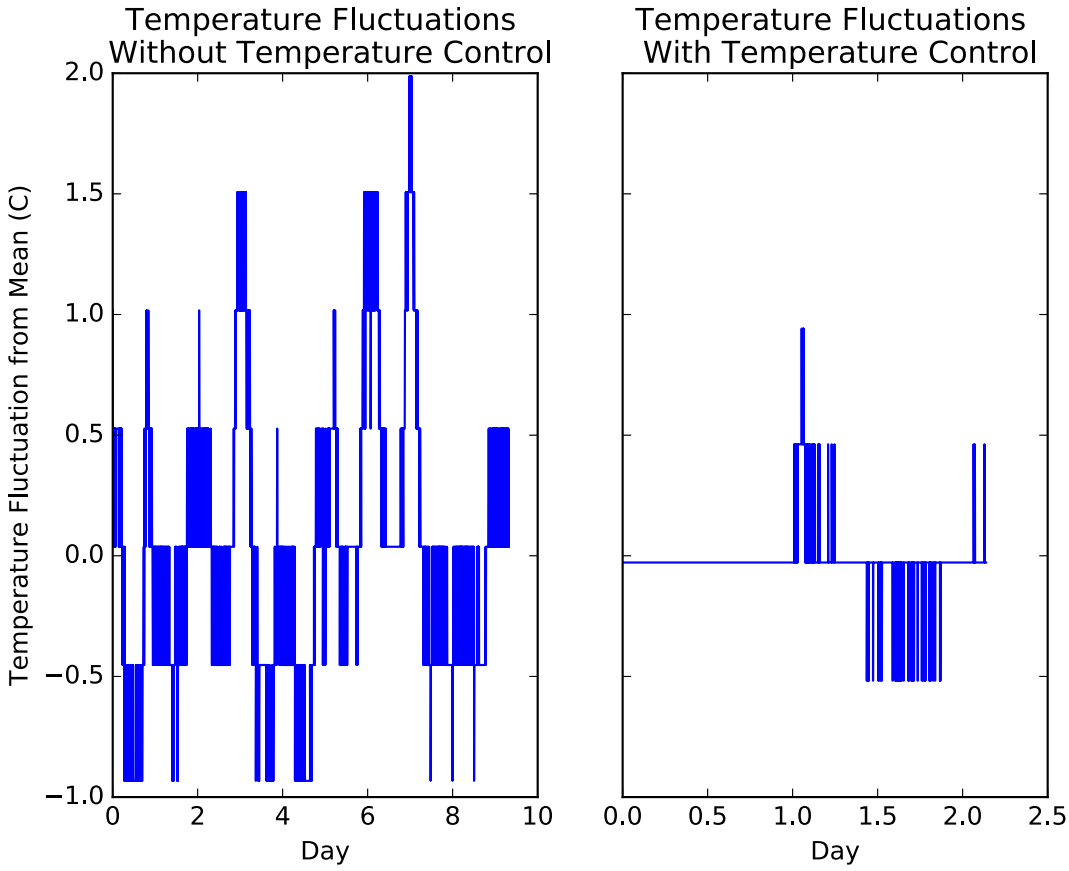

Figure 4.4: A comparison of the enclosure temperature fluctuations with temperature control (Right) to typical lab temperature fluctuations (Left). With the temperature control system running, the dicing saw enclosure maintained typical fluctuations of below $0.5°C$, compared to $1.5 - 2°C$ for the typical lab environment. These measurements have been baseline-adjusted for ease of comparison.

A detailed schematic diagram of this system is present in Appendix A.

4.4 Metrology System

In order to accurately locate the lenses and verify their shape and positioning, a precise measurement system was needed. The required machining tolerances necessitated a measurement device with precision of $\sim 1\mu m$, enough travel to accommodate the curvature of the lens and enable measurement without the

spindle body contacting the optic, and a water and dust resistant construction suitable for exposure to the cutting environment (one of consistent splashing from the flood cooling flow). An Ono Sokki GS-3830 linear gage and readout electronics, with $< 1\mu m$ precision over 30mm of travel and IP67 ingress protection was used for this application. Coupled to a high-speed readout and pneumatically driven lifting attachment, it allowed for the necessary precision measurement of the substrates. The repeatability of the integrated measurement system was tested by repeatedly measuring a single point over a time course. These measurements displayed variability of approximately 300 nm, better than specified and better than necessary for our purposes. This gage was tipped with a 1mm diameter ruby measuring ball, to allow for a precisely known measuring tip dimension and good dimensional stability over time. the gage was connected to a pneumatic lifter designed to retract the gage from its fully extended to fully retracted position, and this system was controlled by an Arduino microcontroller tethered to the computer via a UDP ethernet connection and driven by custom python code. The gage system was mounted parallel to the gantry z-stage, and the parallelism of this was checked by comparing the measured gage difference to the stage readout for a series of descents across the functional range of the gage (>25mm of drop). The gage was located as close to the blade as feasible to minimize the offset between the measurement and cutting coordinate systems. Figure 4.5 shows the measurement gage making a measurement of a silicon test wafer, and Figure 4.6 shows the results obtained from a measurement across several cuts on a lens surface.

4.5 The Dicing Spindle

Central to the entire system was a high speed dicing spindle. This piece is a high-rigidity tool spindle designed for holding commercial dicing blades used in the dicing of silicon wafers. These spindles are precision air bearings with a stiffness such that the cutting forces present in wafer dicing lead to minimal (sub-micron) displacement of the blade, while retaining the low-friction rotation necessary to spin to tens of thousands of revolutions per minute without damaging the spindle body. For this system, we used a spindle purchased from Loadpoint Bearings (a D03411 dicing spindle), designed to accommodate standard hubbed and hubless dicing blades up to $\sim 80mm$ in diameter. Figure 4.7 shows the

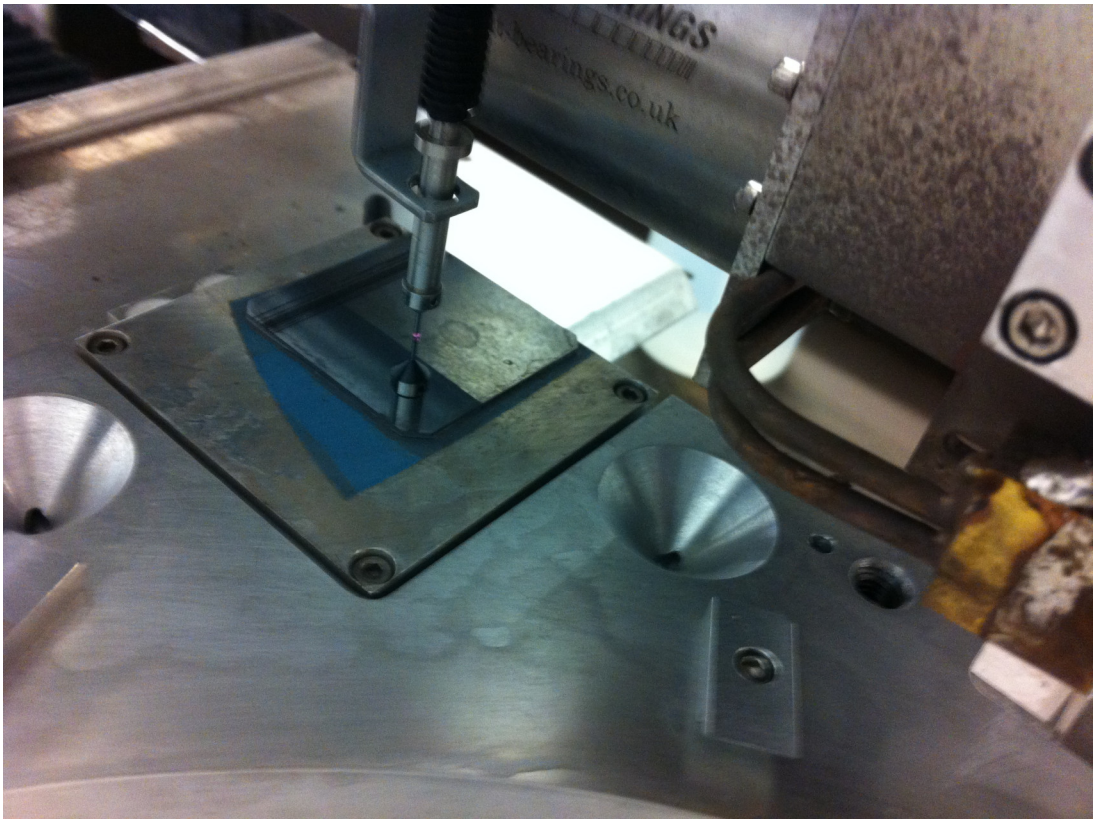

Figure 4.5: The measurement gauge mounted next to the spindle and engaged in measuring a silicon test wafer. The 1mm spherical ruby tip is visible in red in the center of the picture. This gauge provided sub-micron measurement repeatability.

dicing spindle, mounted on the gantry.

4.6 Compressed Air System

Several critical components of the dicing system require a clean, pressurized air supply. Most importantly, the dicing spindle requires >2.5 standard cubic feet per minute (scfm) of air at 75 pounds per square inch (psi). This pressure is higher than that allowed by building codes to be routed through standard walls, so a dedicated compressor system was designed and installed. This system consists of a 5 HP reciprocating pump compressor, a regenerative dessicant dryer, and the full set of particulate and oil coalescing filters needed to remove oil vapor, water, and particulate matter that could damage the spindle air bearing (filtering down to $0.01\mu m$, and removal of all oil vapor and water vapor down to a $-40°C$ dewpoint as specified by the spindle manufacturer). The

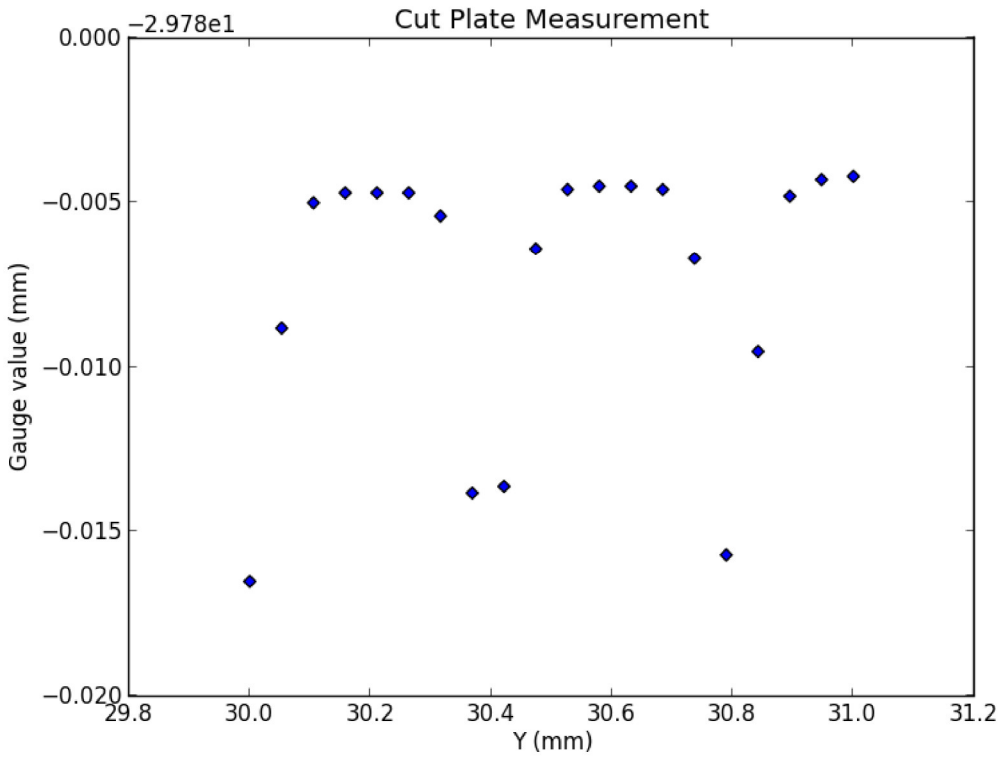

Figure 4.6: A measurement across three cuts on a partially cut lens. The high precision gauge and small (1mm) measuring tip enabled directly measuring the profiles of the cut surface. The measuring ball drops into the grooves slightly, allowing for direct location of features of the cut surface. This capability was used to properly locate the piece after rotation (after a set of cutting operations), and was also used to determine the offset between the blade and measuring ball in one direction.

compressor, dessicator, and filter system is shown in Figure 4.8.

4.7 Fixturing

A set of aluminum fixturing plates were designed to reliably and repeatably hold the lenses in position on the machine X-stage (fixed horizontally to the table). These fixtures were needed to provide a stable base and hold the silicon lenses fixed during the machining process. In addition, these plates needed to offer rapid, precision rotation of the lens both 90° and 180° to allow for machining the 4 necessary orientations of the lens surfaces. Due to the limited blade diameter and large envelope of the spindle body, there is limited clearance below the spindle. The curved sides of many lenses needs to be machined in two stages,

Figure 4.7: The dicing spindle, mounted to the Z-stage interface plate and covered in the hard-earned dirt from many successfully cut optics.

only cutting half the surface at a time to avoid collisions, which necessitates precision rotation in the fixture scheme. The fixtures consisted of two main and several ancillary components. The main components are a base fixture plate, permanently affixed to the x (table-mounted) stage, and individual lens-holder plates. Figure 4.9 shows the lens mounting scheme with individual parts called out, and Figure 4.10 shows the assembled mount, holding a lens and attached to the gantry.

4.7.1 Base Plate

The base plate was machined from a single piece of MIC-6 aluminum tooling plate, 1 inch in thickness. This plate was machined with the appropriate bolt pattern to interface with the stage carriage, and was additionally machined with recessed sections on the top, leaving a set of pads for the lens-holding plates to rest on and be clamped to. A set of 8 clamps were designed to fasten the lend-holding plates down to the base plate securely during machining. The base plate also has a set of stainless steel contact posts, a set of three for each of the 0° and 180° orientations, to precisely locate the lend-holding plate in the XY-plane. The surfaces of these posts were cut with a single pass on a high-precision CNC mill, with the post faces providing an identical three-point mount

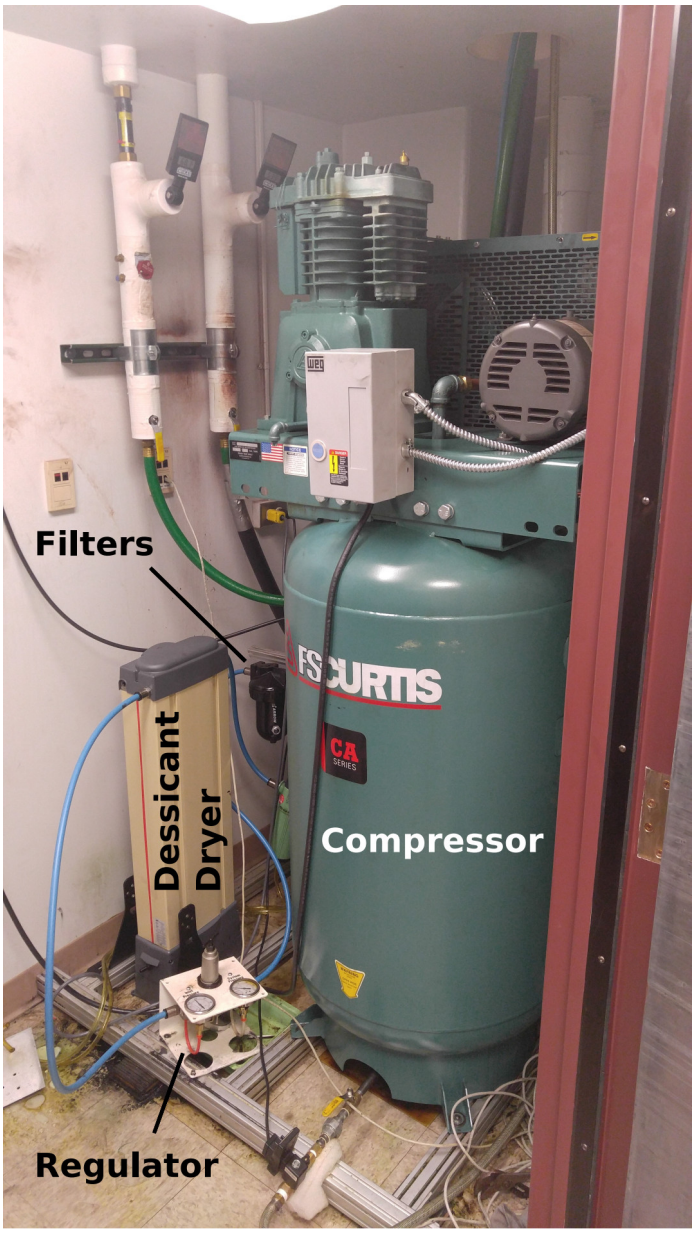

Figure 4.8: The compressed air system feeding the AR coating machine. Visible in this image are the compressor (right), dessicant dryer and regulator (left), and filters (center back). This system provides sufficient quantity and quality of air to run the dicing spindle and ancillary pneumatic components necessary for the machine's proper functioning. A schematic of the complete system can be found in the appendix.

in two orientations that are 180° rotated from one another. This allows for the precise rotation needed at the center of every lens. The base plate also had the mounting points necessary for the flood cooling water management components discussed in Section 4.8.

4.7.2 Lens Plates

The lens plates were also manufactured from MIC-6 aluminum tooling plate, with a necessary thickness of 1.5" to accommodate the thickest curved lens profile from ACTPol. All of the lens plates were designed following a standard template, with adjustments to the hole and mounting diameters necessary to accommodate the three different lens sizes used in ACTPol. A fourth plate was also fabricated to hold flat workpieces and test wafers used in integrating and qualifying the machine performance.

These plates were designed to support the flange around the outer diameter of the different sized lenses, with a set of clamps that engaged on a small (0.5 mm) bevel around the edge. Engaging the bevel was necessary to keep the top clamp surface below the blade to prevent breakage and blade fouling caused by cutting the aluminum fixture material. A section of the central hole was cut through the bottom of the plate to enable lifting of the lens by the bottom surface during mounting and unmounting. The edges of the lens plates held mounting pockets for auxiliary plates used to hold test wafers and dressing blocks needed to calibrate the setup, verify the cut profiles, and dress the blade prior to cutting (a process that entails running the blade through a ceramic substrate to remove lose abrasive and excess material).

Mounting pockets for a set of retaining clamps were also machined into the edges of the lens plates, to provide rigid clamping of the lens plates to the base plate, preventing movement during the machining process. Bolt holes and alignment pins were included to allow for mounting of carrying handles, necessary for removing the fixturing from the machine and rotating it.

Two corners of the plates were beveled to allow for pressure from a screw to ensure seating against the contact posts on the base plate, and all four edges of the plates were numbered with a lens number and orientation to remove any ambiguity in the mounting process.

A set of cones of varying sizes were cut into the plate corners, with the intention

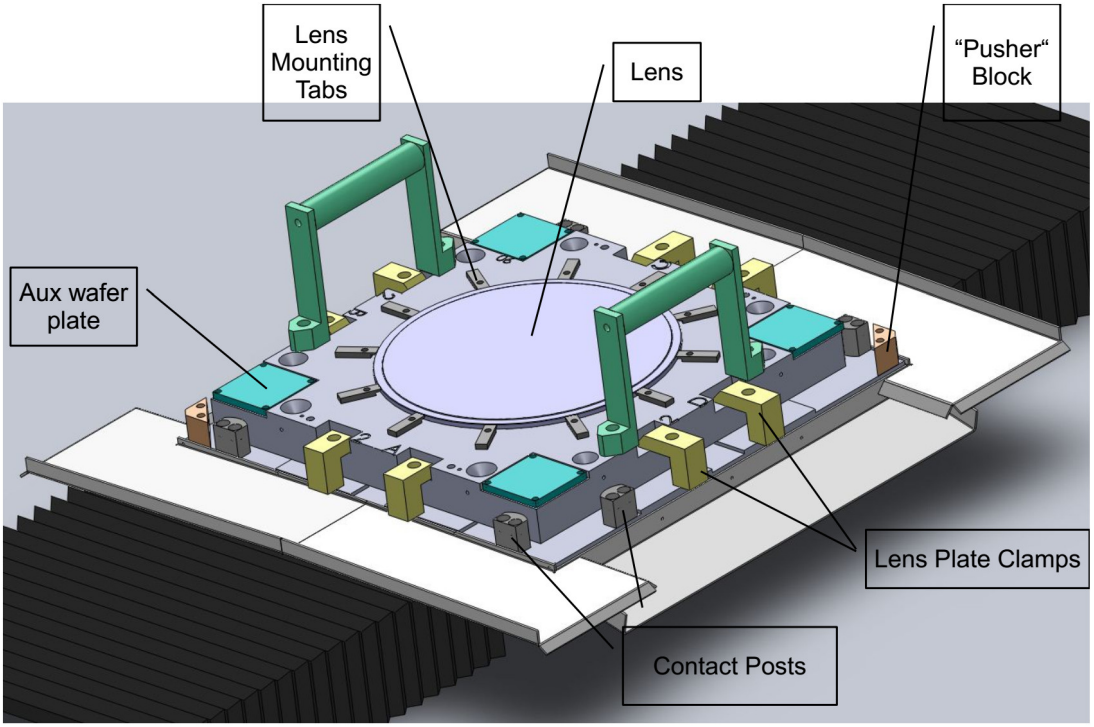

Figure 4.9: A CAD model of the mounting plates for one of the ACTPol lenses. The lens can be see in the center of the fixture, with clamps, auxiliary mounting plates, and the base plate contact posts called out around the edges of the plate. Also visible in this model are the bent metal water deflection gutters and the bellows for protecting the X-stage (on the table surface) from the flood cooling water.

of serving as reference features for locating the fixturing after rotation. It was discovered that the machining was insufficient for these to serve their intended purpose, so the idea was abandoned in favor of directly locating the lens surface (a process that was possible, even on the cut surface, due to the precision of the measuring probe and strength and rigidity of silicon). See Figure 4.6 for the measurement data from a direct cut surface measurement, and Figure 4.11 for a photograph of the center of a cut lens (showing cuts from four separate mountings, and demonstrating the precision with which the direct measurement system can locate a lens).

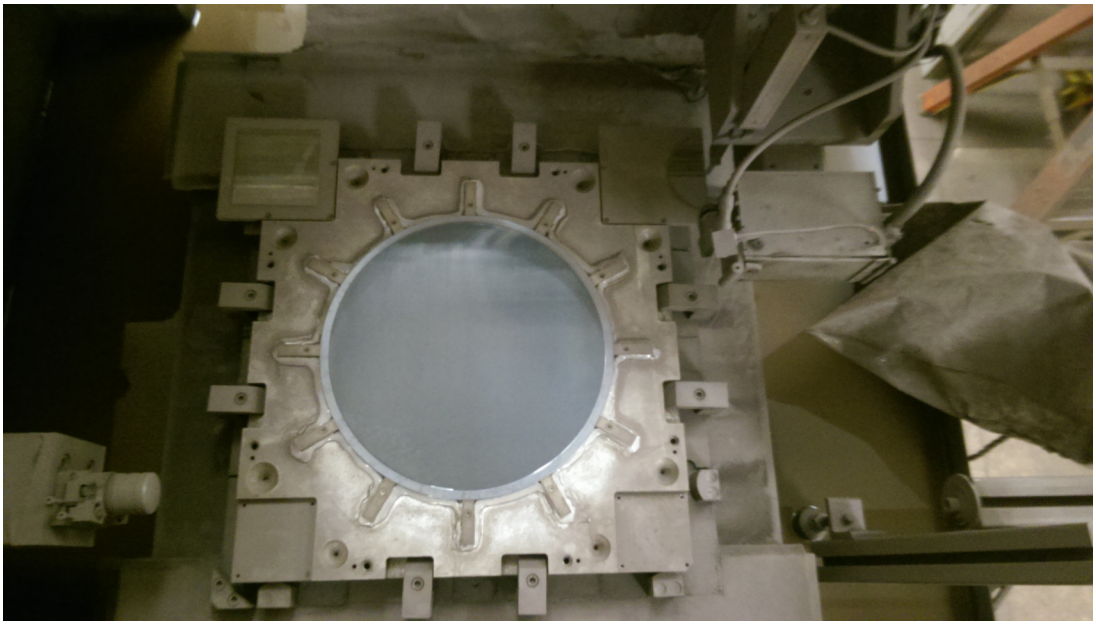

Figure 4.10: The fixturing mounted on the machine and holding a lens.

4.8 Water Management

The abundance of flood cooling water necessitated implementing an extensive water management system. This system consisted of several layers of passive ingress protection and water redirection. The first layer of water management occurred at the base plate mounted on the table (X) stage. This plate had the mounting holes (connecting it to the stage carriage) completely sealed with silicone sealant, and a series of overlapping gutters connected to the outer edges. This channeled the flood cooling runoff over the edges of the plate and into the catch trays that sat on either side of the stage. Splash guards were installed along the sides of the stage that overlapped the edge of the catch trays, preventing water ingress via the gap between the gutter and catch tray. In addition to the gutters, along the travel of the stage, a pair of covers (made from coated HDPE fabric, similar to Tyvek ^{TM}) were run to divert any direct water. Below the gutters, a pair of custom bellows were attached as a final passive barrier over the stage. Compressed air was also run into the stage, both for cooling and as a final protection against ingress of water and cutting debris.

Water collected in the catch trays falls through drain hoses into the flood cooling tank, where it is filtered and recirculated. Figure 4.12 shows the primary water management components in place on the fully integrated system.

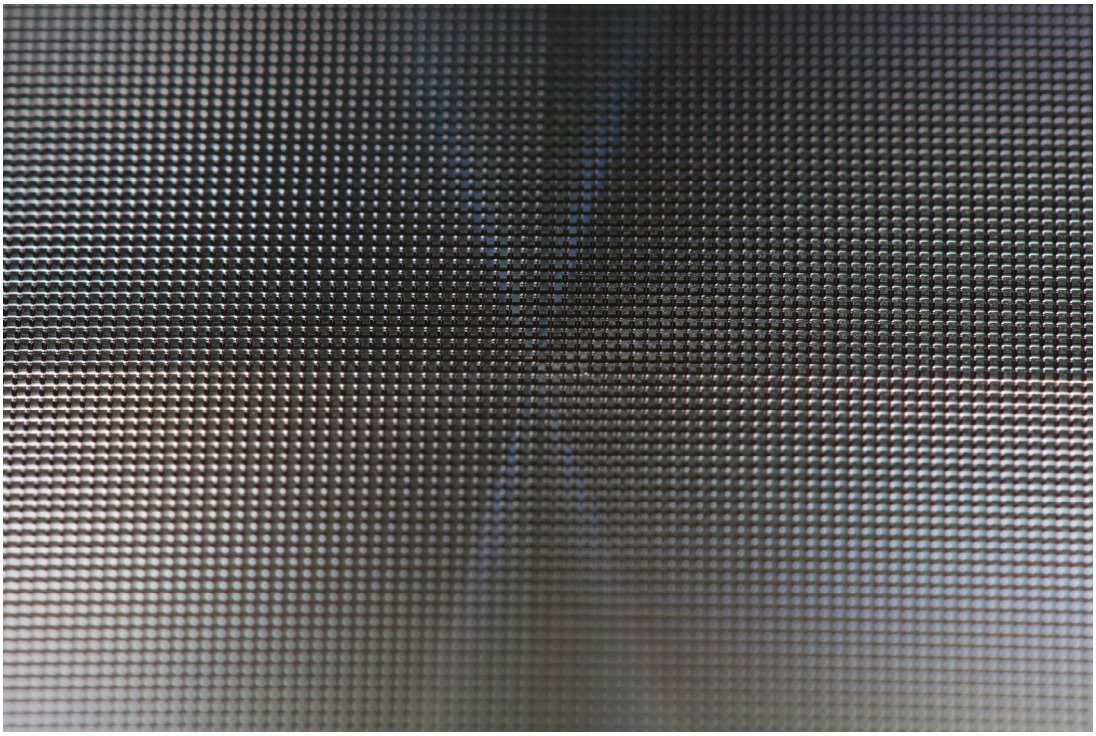

Figure 4.11: The center of one of the lenses, after being completely surface treated. A slight difference in cuts is visible when crossing the center line due to the light reflecting off the cut floors. The consistency in pillar size across the lens center demonstrates the successful rotation of the lens and measurement of the lens in the various orientations. Ultimately, this demonstrates the successful performance of the fixturing throughout an entire set of machining operations spanning the course of approximately one month.

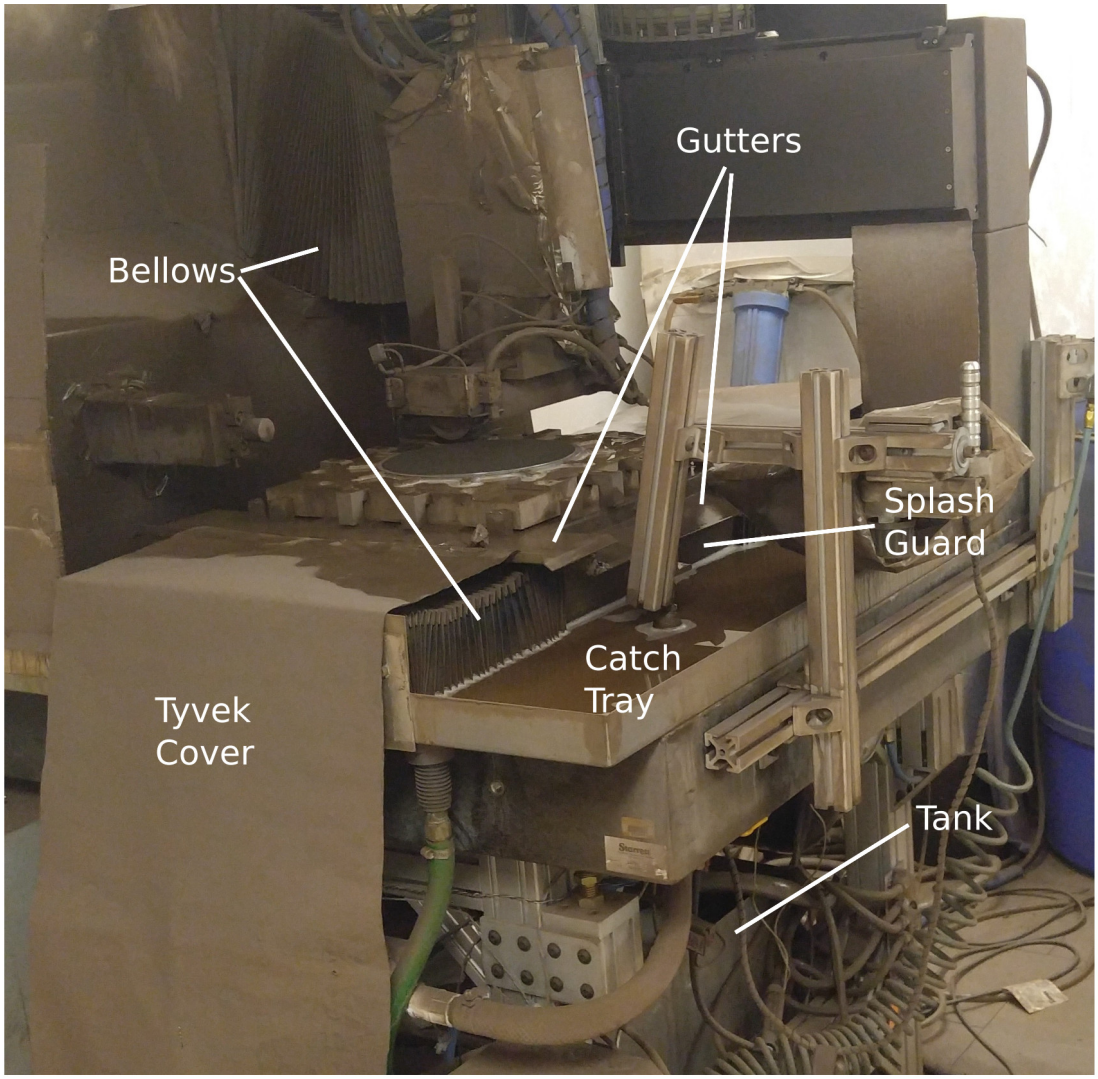

Figure 4.12: The AR coating machine, well used, illustrating the various water management methods in place. In this photo, the gutters, covers, bellows, and catch trays are all called out, as is the flood cooling tank underneath the machine table.

4.9 Table and Enclosure

In order to enable careful control of the temperature and environment of the machine (necessary to achieve the desired tolerances), an enclosure had to be constructed. An enclosure constructed from a frame of extruded aluminum"T-Slot" fixturing was designed to accommodate standard 4x8 foot panels in the walls and ceiling. This allowed for easy construction with readily available materials. It was sized with a height of of approximately 8 feet, a with of approximately 8 feet, and a length of approximately 12 feet, which allowed it to fit in available space in the lab while providing enough room to contain the gantry, all ancillary equipment (such as the temperature control system), and room to work on the machinery and fixturing.

The walls were constructed of double-walled corrugated plastic, which provided good thermal insulation while being inexpensive and easy to acquire and work with. The roof was constructed from similarly corrugated polycarbonate, to allow for light from the room to enter the enclosure. There was a desk at the front end of the room, with a double-paned window formed by two layers of acrylic sheets. This desk contained mounting provisions for the control electronics and a dedicated computer that ran the entire machining system. It allowed for the machine operator to be seated outside the enclosure with full visibility of the operation of the machine. Additionally, a section of one wall was also made from double-paned acrylic to allow for visibility from the remainder of the lab. This brought the machine into compliance with applicable fire code. This section of wall was also made removable to allow for removal of the gantry if necessary for future service or modification.

A sliding door at the front of the room allowed entry. A chimney in the back of the room was built to mount the water-to-air heat exchanger, filter, and fan that circulated the air in the room to control its temperature via the system discussed in Section 4.3.

A table to support the granite base of the gantry was also designed and built from T-Slot extrusions. This table was designed to support a total weight significantly greater than the $\sim$ 4000 pounds of machine (inclusive of granite, stages, and fixturing). It sits on a set of adjustable feet and heavy duty casters that allow for movement of the entire machine. These were necessary for the initial transport of the machine to the lab and to allow for movement of the

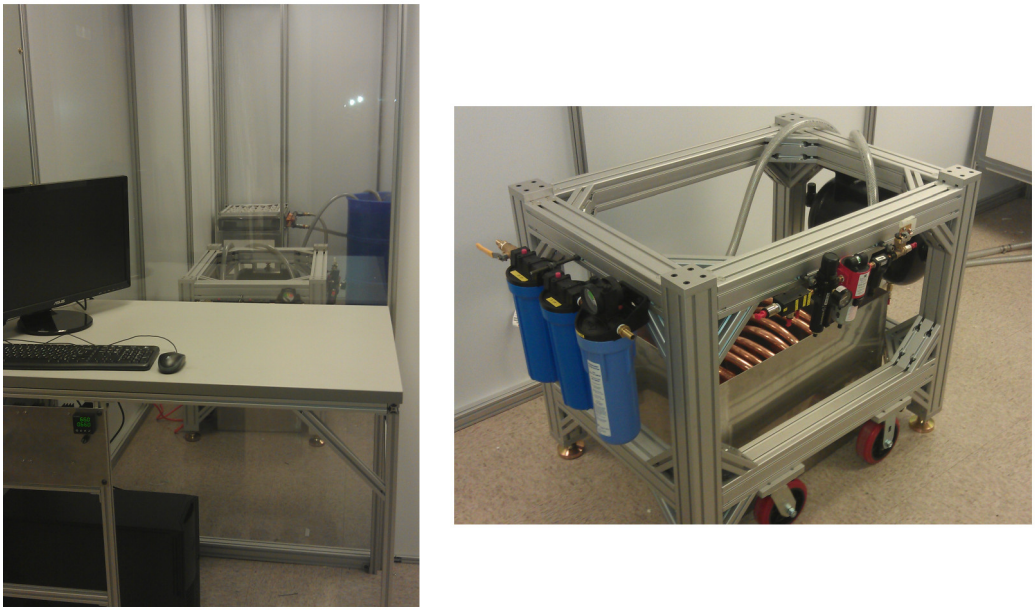

Figure 4.13: Left. the machine subroom, viewed through one of the transparent acrylic viewing walls. At the front of the room is a desk where the machine operator sits and where the control electronics are located. The machine table is visible in the center of the enclosure, and the water-air heat exchanger and temperature control system are visible in the back. Right, the machine table with pieces of the flood cooling system (blue filter housings on the left, copper heat exchanger in tank in center), and compressed air system (filter and regulator visible on front side of table, ballast tank on rear right).

machine as needed. The table also encloses the water tank used for the flood cooling system, and supports pieces of the flood cooling, compressed air, and control systems tied into the T-Slot extrusions.

Figure 4.13 shows the machine table and enclosure, prior to integration of the gantry and control electronics.

4.10 Control Electronics and Software

4.10.1 Control Electronics

The machine was controlled with a mixture of commercially provided and custom designed electronics. The gantry was controlled by an Aerotech A3200 motion controller, provided with the system. This was controlled via a Firewire interface by a computer running Windows 7 (necessary for properly interfacing

with the A3200 controller) and a mixture of python code and AeroBasic (a proprietary language used by Aerotech). This code is explained in greater detail in Section 4.10. The low-level control software (handling communication between the computer and drive controller, and control system commands within the controller) was provided by Aerotech, and all higher-level control software was developed in-house by me.

The spindle was controlled by a Sieb & Meyer SD2S drive amplifier, as provided by Loadpoint Bearings.

The temperature control system was run by a standalone PID controller.

The air lifter and flood cooling were controlled by an Arduino connected to the computer via ethernet. A custom python application gave a graphical interface to control the switching of these functions, and the Arduino drove switching circuitry that handled control of the physical devices (via a solid state relay for the flood cooling pump, and a solenoid driven valve for the air lifter).

Several failsafes were designed and built into the system. A pressure switch attached before the buffer tank feeding the spindle was set to automatically stop the spindle in the case of low pressure in the air supply. Additionally, the spindle shutting off triggered a rapid stop of the stage controller, ensuring no damage to the workpiece in such a circumstance.

A flow switch was placed in the flood cooling system, with a check in the controller code to ensure the flood cooling is functioning during all cutting operations.

A diagram of these systems can be found in Appendix A.

4.10.2 Control Software

Control software was written to perform the tasks necessary to locate the lens, determine the position of the blade relative to the metrology coordinates, determine the desired cut paths, and cut the features into the lens surfaces. A brief overview of this software is presented here, and an overview of the machining procedure is located in Appendix A.

(a) Locating the workpiece was done by first measuring the surface with the metrology probe. The probe was extended, and the machine rastered over the surface, dropping to engage the probe at the desired locations. The

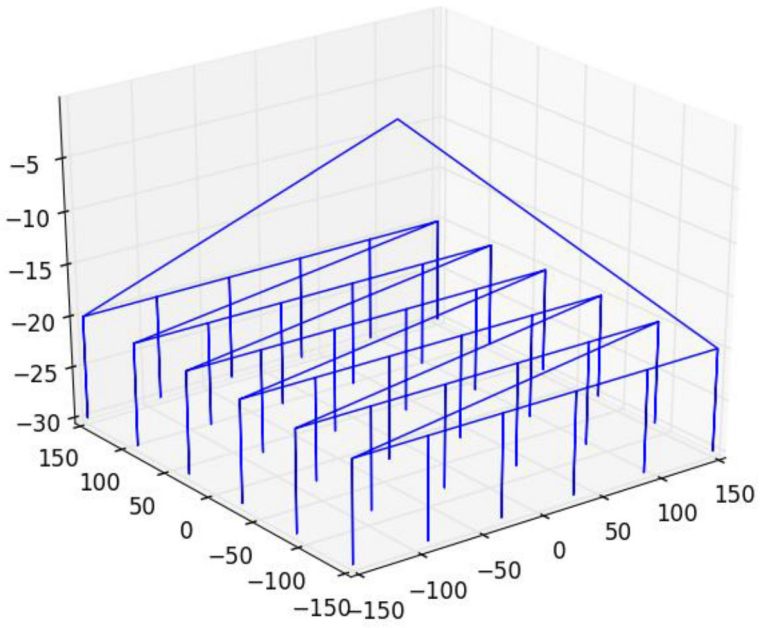

Figure 4.14: The motion path logged by the machine during a standard workpiece measurement operation. By rastering over the surface and dropping down to engage the measurement probe, we are able to measure the full workpiece to the precision needed to locate and cut with micron accuracy.

machine location and gauge readout were stored to a data file for later processing. On cut surfaces, a set of fine-pitch points were measured at each location, with the highest point being selected to ensure measurement on the tops of the cut pillar features (corresponding to the surface of the original optic). Figure 4.14 shows the machine path as it rasters over the surface during workpiece location.

(b) The blade location in measurement coordinates was determined by cutting a circular feature and two shallow cuts into one of the test wafers mounted alongside the optic. The circular feature allowed for determination of the blade center and radius in the plane of the blade (the YZ-plane), and the two shallow cuts allowed for location of the blade in the perpendicular direction (X direction). These features were then measured at high resolution and the measurement data was fit to determine the center position in blade coordinates. The diameter obtained here was checked against the

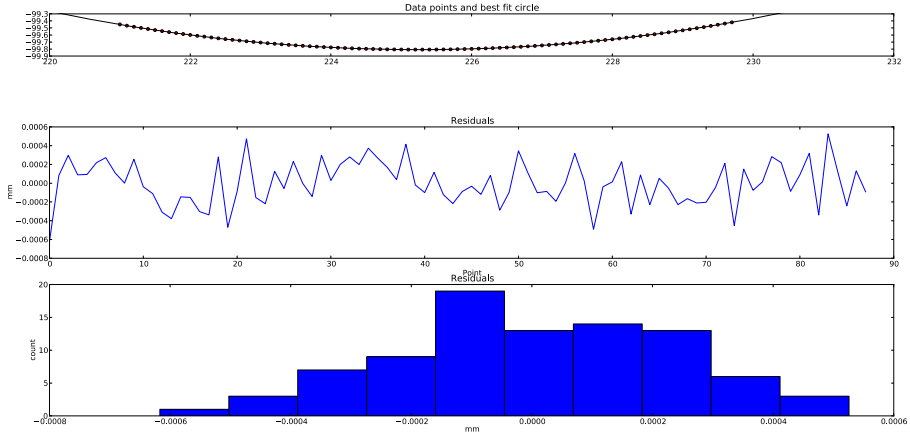

Figure 4.15: The fitting of the YZ-plane calibration feature. The blade cut a circle into a test wafer, which was then measured with the probe. These data were fit to determine the offset and blade diameter. The top panel shows the data and the best fit circle, the center panel shows the residuals from the fit, and the bottom panel shows the distribution of the residuals. Residual distribution widths of less than 1μm were typical for the measurement setup.

diameter specified by the manufacturer, and the location and diameter were additionally checked through a set of test cuts and test touches on workpiece surfaces to ensure proper alignment. Figure 4.15 shows a measurement of the blade radius and center, used to determine the necessary offsets in the YZ-plane. Figure 4.16 shows a test wafer with several sets of calibration features and test cuts visible on the surface.

(c) The raw measurement data was then fit with the appropriate shape to determine the optic location in the measurement coordinates. For the convex surfaces of ACTpol optics, this shape was a modified asphere adjusted to account for the effect of measuring the surface with a spherical probe tip. For the flat surfaces, this shape was a plane adjusted in the vertical direction to account for the offset from the probe tip. Once the location of the optic was fit, the fit residuals were checked to ensure that the deviations from the expected surface were smaller than required by the tolerances for the coating. In later modifications to the software, these surface residuals (attributed to deformations induced by the fixturing) were fit out and removed. Figure 4.17 shows the residual errors after fitting an ACTpol

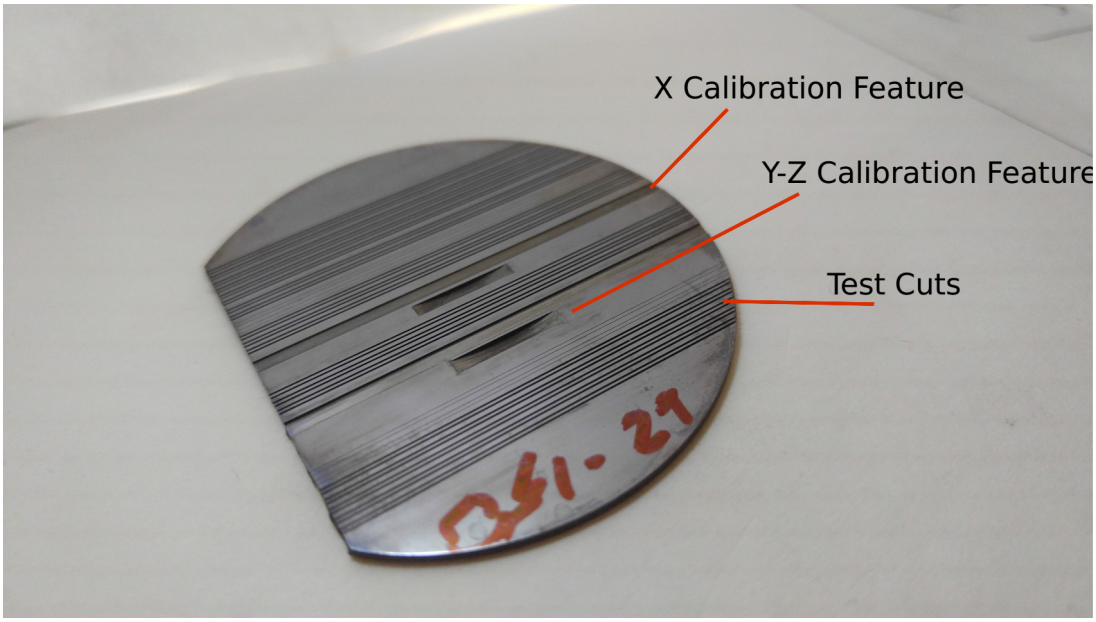

Figure 4.16: A test wafer with a set of calibration features cut into it. The shallow cut "X-feature" allows for precisely measuring the position (in the X direction) of a set of cuts, and the circular "Y-Z feature" allows for determination of the saw blade center position and diameter.

lens.

The optic location information, blade offset, and blade diameter were then used to generate a set of toolpaths for the saw to follow. These toolpaths were generated by sampling the model surface at a fine pitch across each desired cut, then shifting the coordinates outward in the direction normal to the surface in the YZ-plane (in the plane of the blade). The motion control was configured to take these toolpath points in and move through them, linearly interpolating. The pitch was set so the maximum deviation from the model surface was below 0.1 μm. Figure 4.18 shows a sample toolpath for a single cut, with the blade profile and lens surface overplotted.

(d) The code running on the motion control hardware was configured to sequentially read in each cut's path information, move to the start of the path, verify that the machine condition was acceptable by checking that the spindle is still running properly and flood cooling flow was normal, then cut along the defined toolpath for the cut. When the full set of cuts was completed, the machine stopped and created a file to signal the completion of cutting (and to prevent running of the same set of cuts again).

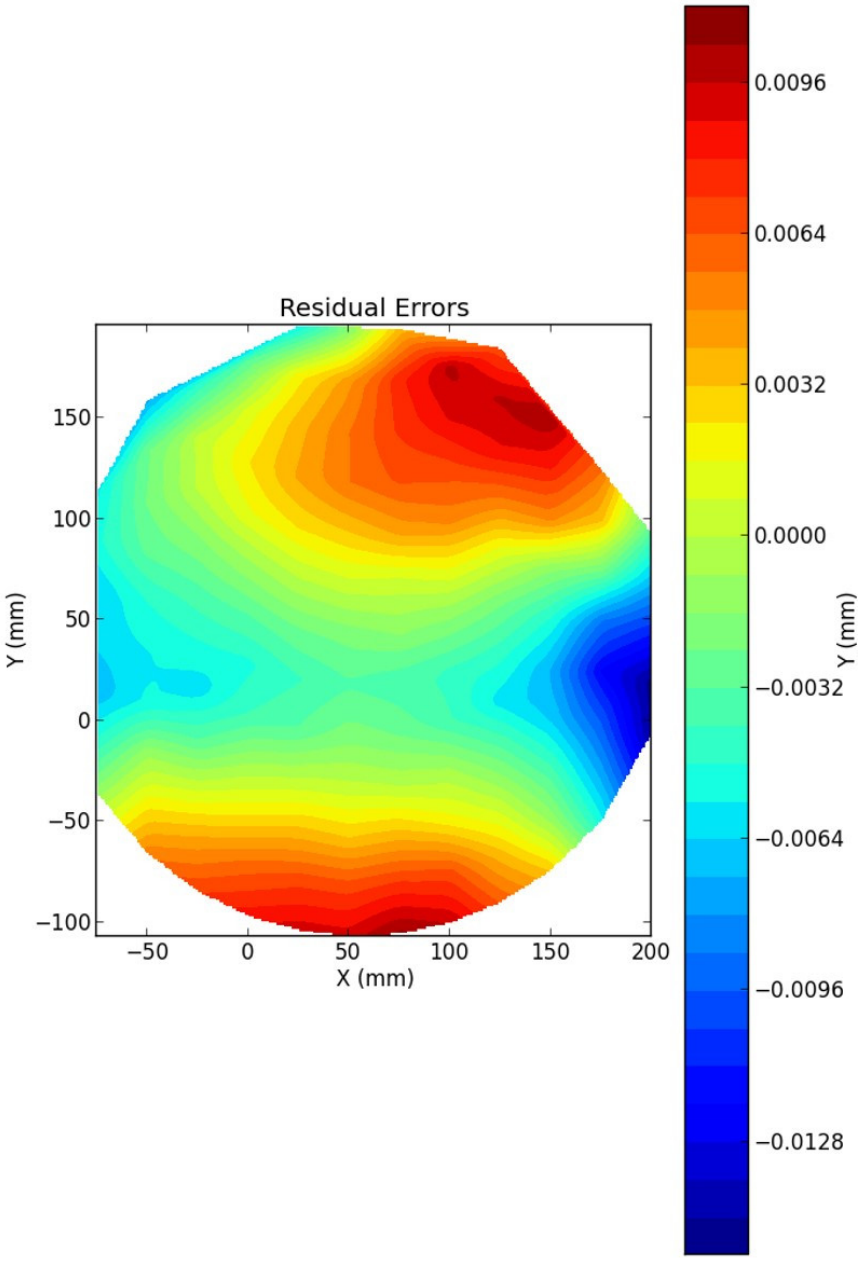

Figure 4.17: the residual error left after fitting one of the ACTPol optics. The $\sim 20\mu$m saddle shape is characteristic of all measurements and is attributable to machining errors in the fixturing. It can be fit out separately and compensated for if necessary for a specific optic.

4.11 Microscope

A microscope was added, looking in from the side to the edge of a test wafer. This allowed for in-situ characterization of the cut shapes, allowing for opti-

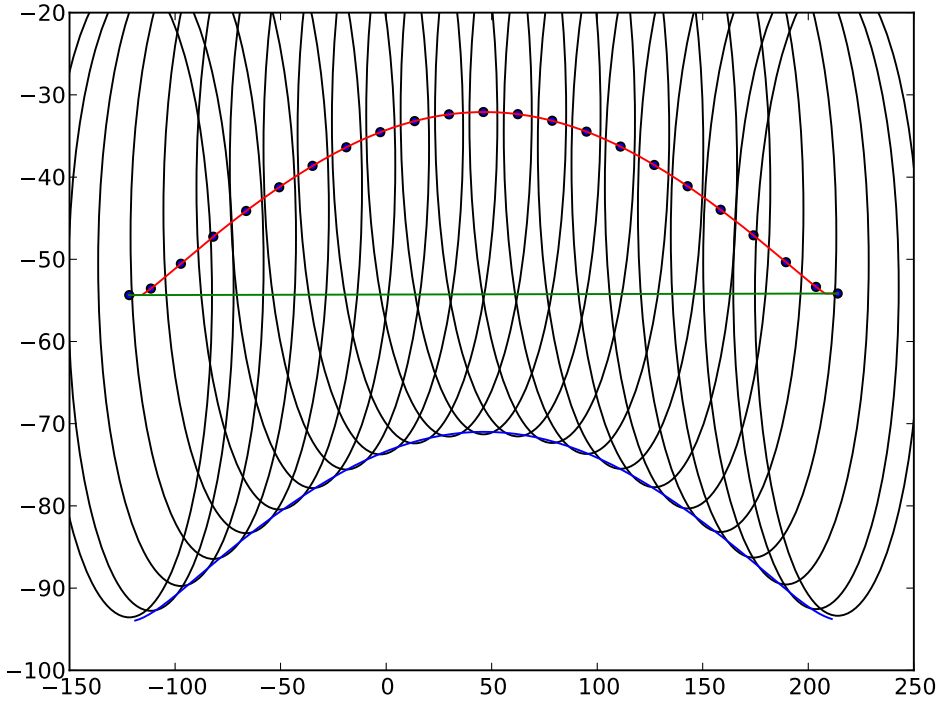

Figure 4.18: A plot of the toolpath (red) and lens surface (blue), with circular blade positions overplotted (black). This shows the path followed by the saw over the surface of the lens for a single cut.

mization of the design around the actual cut profiles. This microscope is shown in Figure 4.19, and a cut profile measured with it is shown in Figure 4.20.

4.12 Testing and Qualification

Following integration and commissioning of the AR coating system, careful testing was needed to ensure acceptable performance, reliable operation, and to develop a procedure for successfully fabricating AR surfaces on the necessary lenses. There were several phases of testing and qualification that verified the performance and proved the machine capabilities, culminating in the successful fabrication of numerous optics for the ACTPol project. The testing was broken up into an initial testing phase, to verify the functionality and performance of the individual systems, and characterize the cutting performance and stability of the complete system. This testing concluded with the successful cutting of a

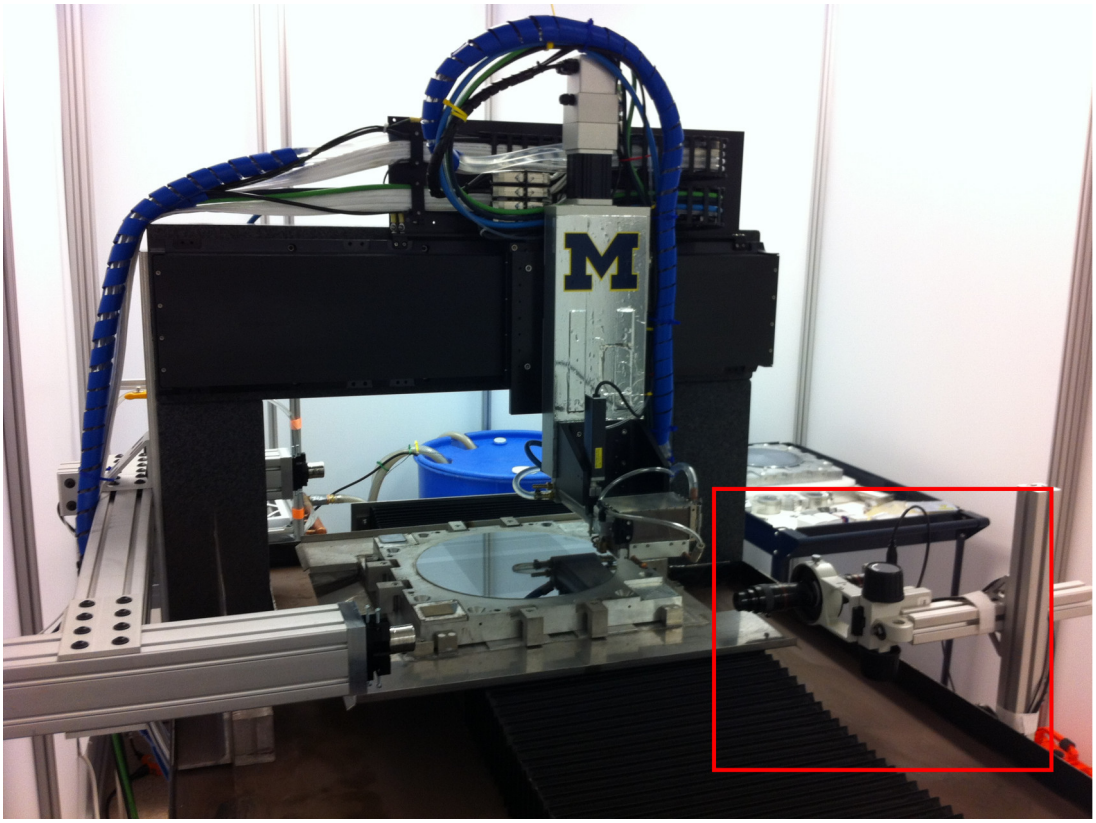

Figure 4.19: The gantry system with the side-looking microscope outlined in red.

mock AR surface into a polycrystalline silicon lens blank (a mechanical mockup from the ACT project with unknown shape). This was followed by testing and characterization during the fabrication of various optics for the ACTPol project in the form of checks during the machining process and optical reflectance tests of the finished pieces.

4.12.1 Initial Testing

The initial testing of the dicing system consisted of:

(a) A set of initial cuts to verify the proper function of the saw

(b) A series of cuts with increasing cutting speed that established a set of sensible cutting parameters and allowed for dialing in of the necessary flood cooling rate. Sets of cuts were made at a variety of speeds between 3 mm/s and 51 mm/s (the limit imposed by the motion control software provided by Aerotech). All speeds below 51 mm/s cut cleanly and successfully (with a single chip occurring at a 51 mm/s speed), and a standard cutting speed

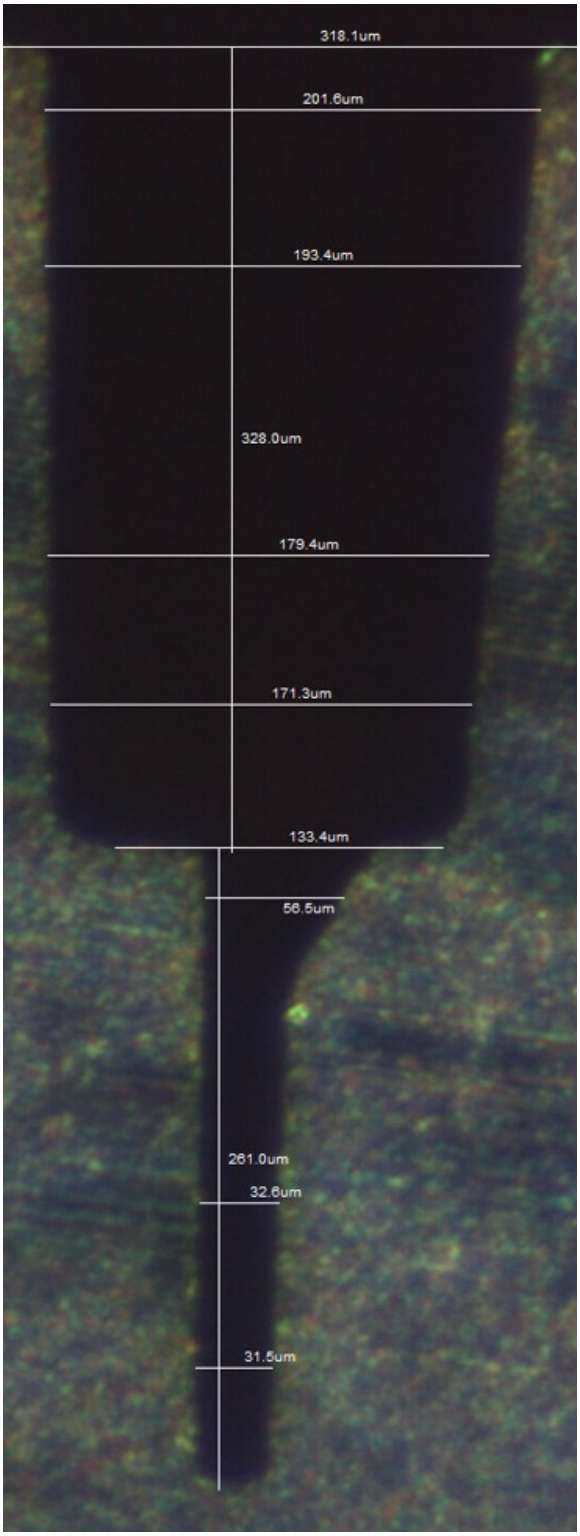

Figure 4.20: A set of cut profiles observed via the side-looking integrated microscope.

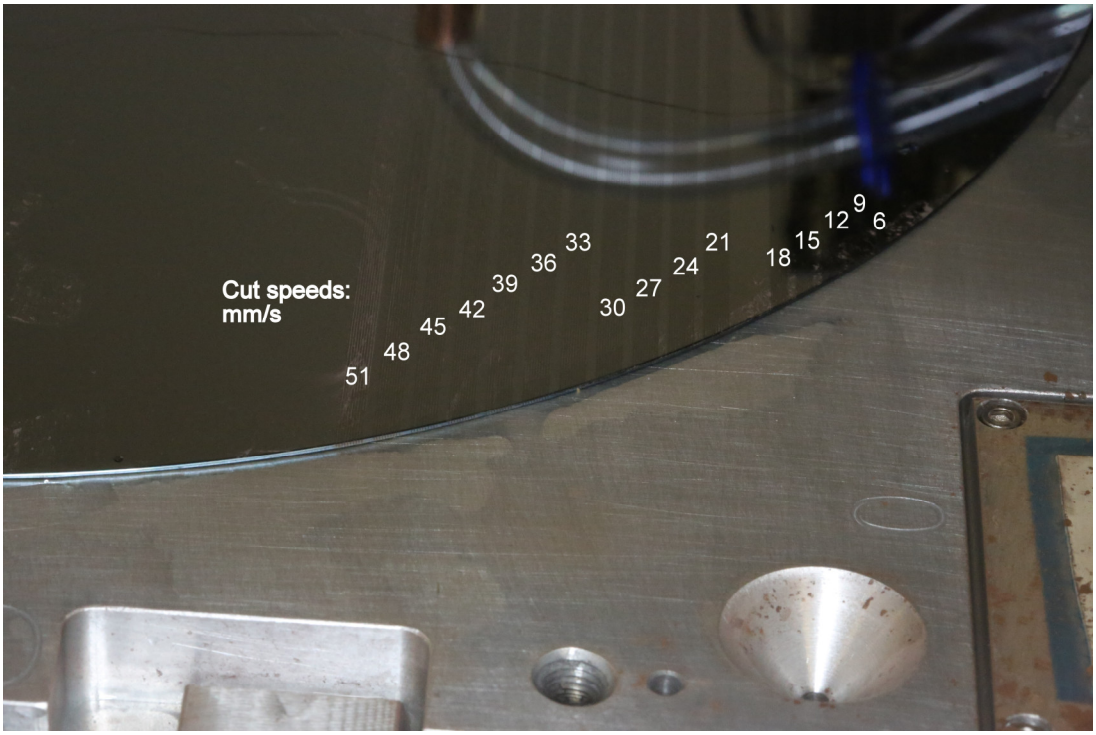

Figure 4.21: Sets of the initial cuts, with the cutting speed increasing between successive sets. This helped establish the acceptable cutting parameters and dial in the volume of flood coolant needed for proper operation.

of 25 mm/s was adopted for all future operations. A set of these cuts are shown in Figure 4.21.

(c) A grid was cut, demonstrating the precise rotation of the fixtures and providing verification that the necessary square features could be cut with the hardware configuration that was designed. Figure 4.22 shows the first test grid cut.

(d) Long duration run tests, to demonstrate that the cutting was stable over the time period of typical machining operations and to track and characterize the evolution of a blade over a full set of machining operations. The cutting was found to be stable and repeatable, with excellent performance over a set of several 12" diameter wafers, and the blade evolution was found to be measurable, but minimal. The ultimate design approach takes the initial blade shape and projected wear into account in optimizing the design, and shapes before and after cutting are recorded to maintain records of the dimensions as cut. Figure 4.23 shows the change in blade shape over a long-duration test run.

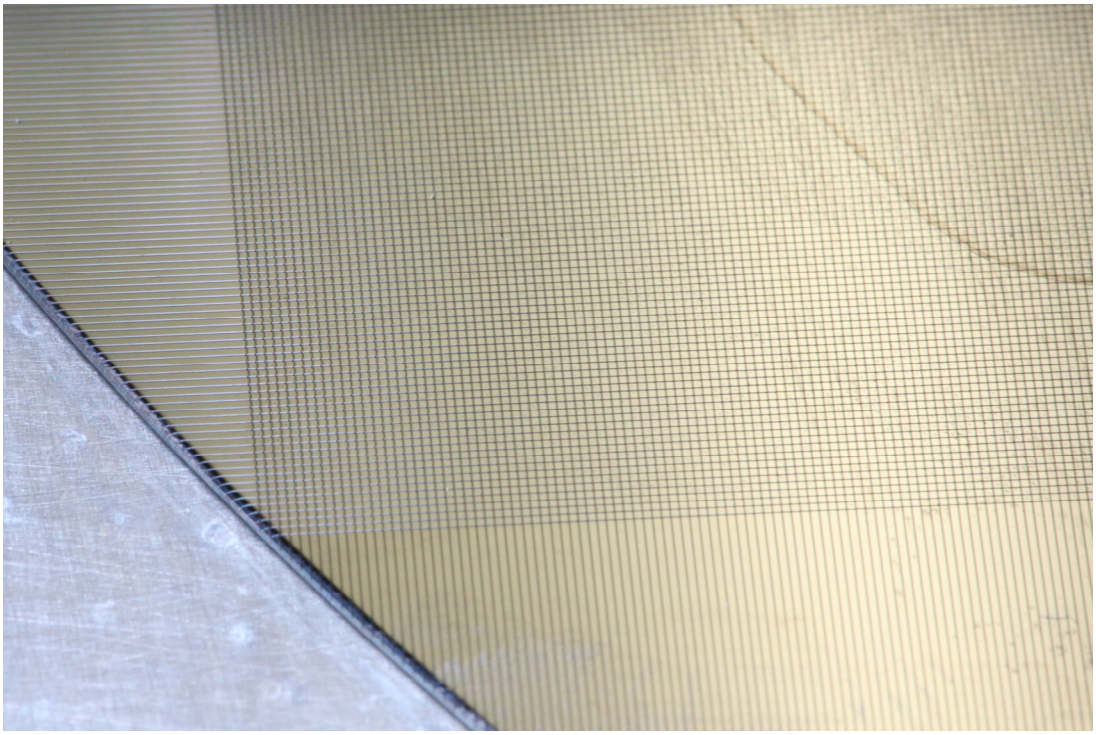

Figure 4.22: The first full test grid, demonstrating the successful operation of the fixturing and saw for cutting square features.

(e) Cutting of a curved lens mockup. A polycrystalline silicon lens blank left-over from the mechanical commissioning of the ACT project was used as a demonstrator for the ability to cut curved surfaces. This test was successful, with a single-layer coating cut into the surface in all four orientations with good control and minimal unintended damage to the (fragile, due to its polycrystalline nature) lens surface. Figure 4.24 shows the curved lens mockup used to demonstrate the ability to cut curved surfaces.

4.12.2 Integrated Testing

This was followed by a set of integrated tests in which a full workpiece was cut and the characteristics of the resulting surfaces were carefully measured to ensure the proper operation of both the machine and, in later pieces, the coating design process being used. This more involved integrated testing consisted of:

(a) Cutting a set of complete MARSs on mechanical test wafers, and characterizing the cut profiles and depths on an Olympus LEXT confocal microscope. These measurements confirmed correct cut widths and depths to

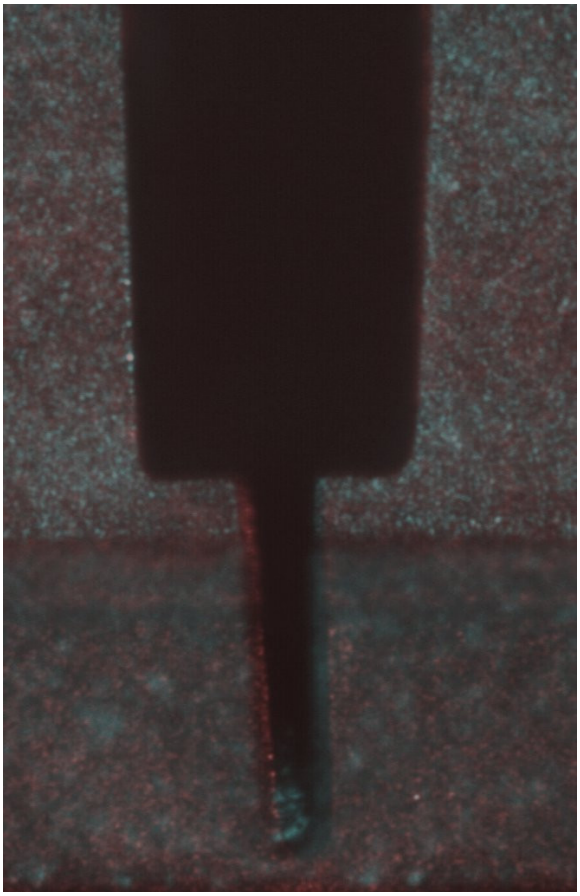

Figure 4.23: A set of cuts before (blue) and after (red) long duration cutting, overplotted to show the slight change in blade shape. The top (wide) cuts are aligned, showing a thinning of several microns. In this setup, there was also a shift of ~ 10 microns in the thin blade (lower cut). These were both acceptable values, with the change in thickness accounted for in optimization of the coating. The shift does not change the coating performance at all, provided it stays within the boundaries of the upper cut.

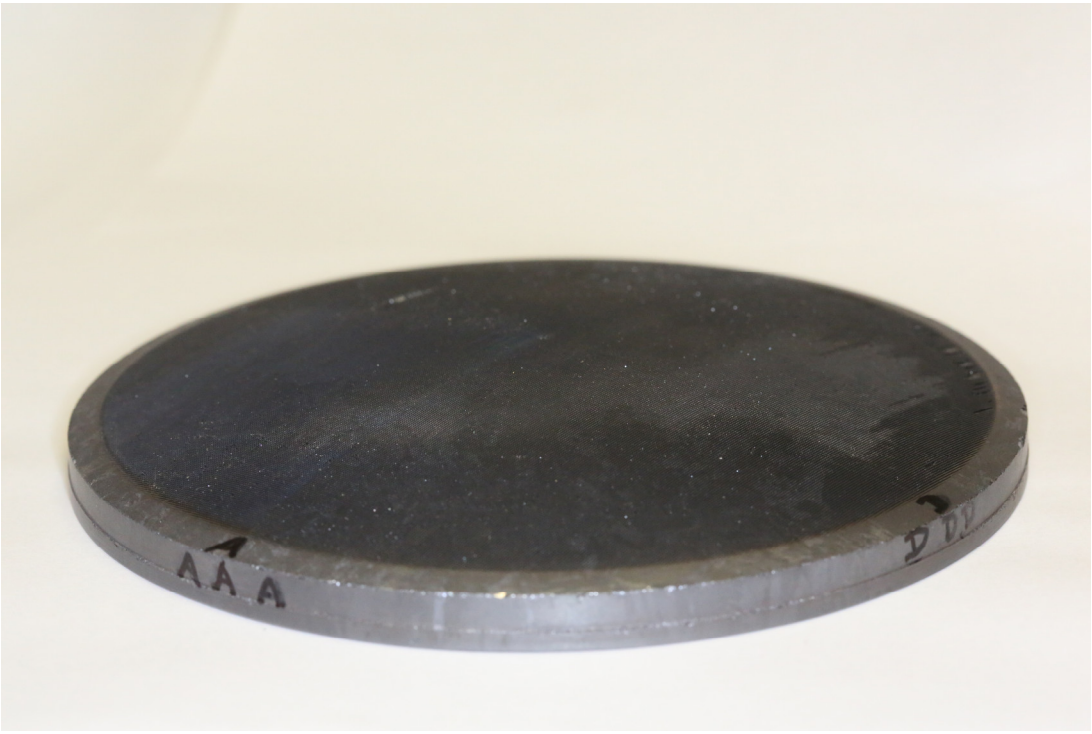

Figure 4.24: A polycrystalline silicon lens mockup. This piece was a mechanical blank from an earlier stage of the ACT project, and was used as a demonstration piece for cutting a curved surface. A single structured layer was cut into the surface successfully. There is a small amount of chipping along one edge due to the polycrystalline material being weak enough along grain boundaries to flake apart from the force of cutting. This problem was not observed in actual optics consisting of monocrystalline silicon.

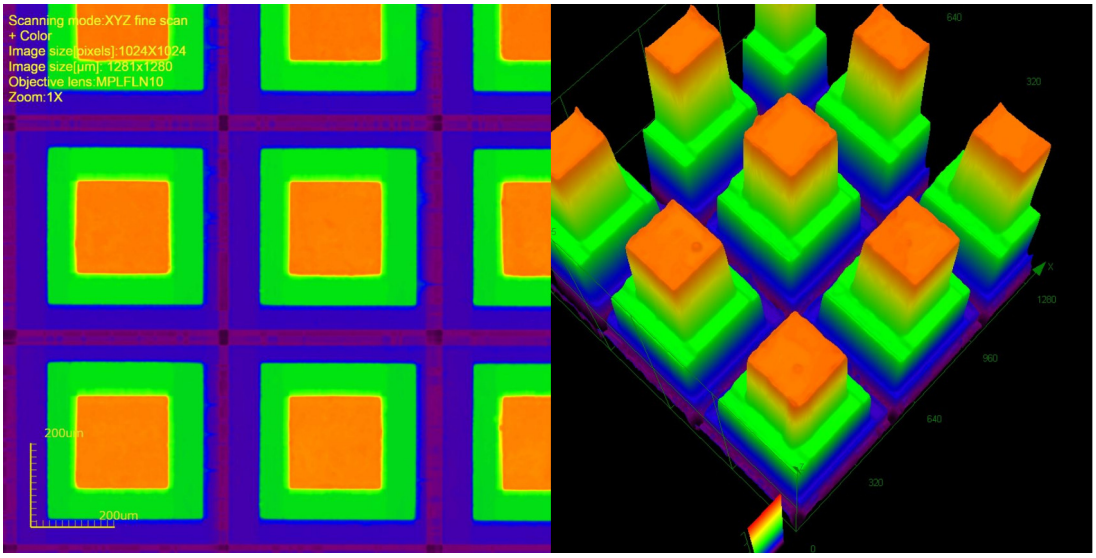

Figure 4.25: False-color images of a 3-layer metamaterial taken with an Olympus LEXT confocal microscope. The color corresponds to the measured height of the surface at a given point. These measurements were used to confirm the cut depths and widths, and to verify that the cut profiles did not change substantively across the surface of a given optic.

within $2\mu m$ (the precision of depth measurement on the LEXT for high thickness objects) in places where the surface was accurately measured. Figure 4.25 and Figure 4.26 show images obtained from LEXT measurements of several sample metamaterial structures.

(b) Cutting a set of full MARSs on mechanical test wafers, separating sections of the wafers, and measuring them on the integrated side-looking microscope. These confirmed that the measurements on test wafers of the cut profiles corresponded to the actual cut profiles in the test piece.

(c) Cutting a 2-layer 150 GHz MARS on a small 2" wafer of high resistivity silicon, giving a fully anti-reflection coated optical test sample. This sample was then measured on a reflectometer consisting of a swept frequency source, frequency multiplier chain, feedhorns, and detector diode. These initial measurements provided confirmation that the optical performance of the surfaces was suitable (by establishing a limit of <1% on reflectance of a double-sided sample, limited by the measurement) to begin fabrication on ACTPol optics.

(d) Cutting a full 2-layer MARS on the first ACTPol lens, providing a complete test of the process on a real optic, and demonstrating the reliability of the

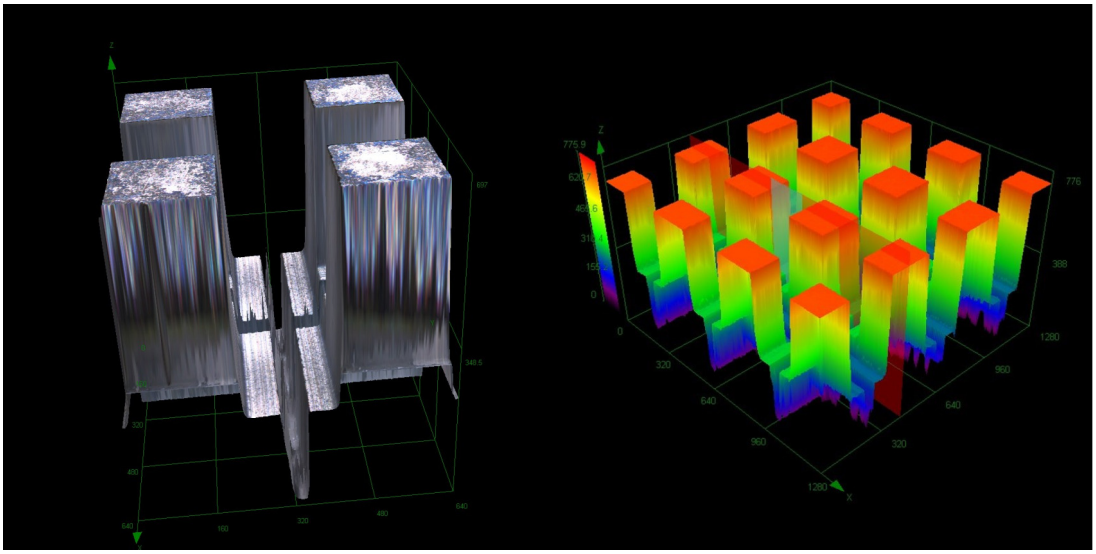

Figure 4.26: Real- and false-color images of a 2-layer metamaterial taken with an Olympus LEXT confocal microscope.

process and equipment during the production of one of the final products. This lens was also measured on the reflectometer to confirm a suitably low reflectance for deployment on ACTPol. The detailed performance of the real optics is discussed in the following section. Figure 4.27 shows a photograph of this lens, with the structured surface clearly visible.

4.13 Machine Performance and Capabilities

After the initial mechanical and optical tests were completed satisfactorily, there was enough confidence in the machine's function to fabricate the real deployed optics for ACTPol. These optics ranged in size between 25 and 35 cm in diameter, with varying curvature on their aspherical sides (and flat surfaces on their other sides).

Optics were successfully fabricated for the single-frequency and multichroic arrays for the ACTPol project, with antireflection surfeaces tailored for the 150 GHz single-frequency pixels and the 90/150 GHz multichroic pixels. These optics were all successfully fabricated and thoroughly characterized before being deployed on the ACTpol project. The multichroic lenses enabled the deployment of the first multichroic detector array on a CMB experiment, with the deployment of the 90/150 GHz array on ACTPol.

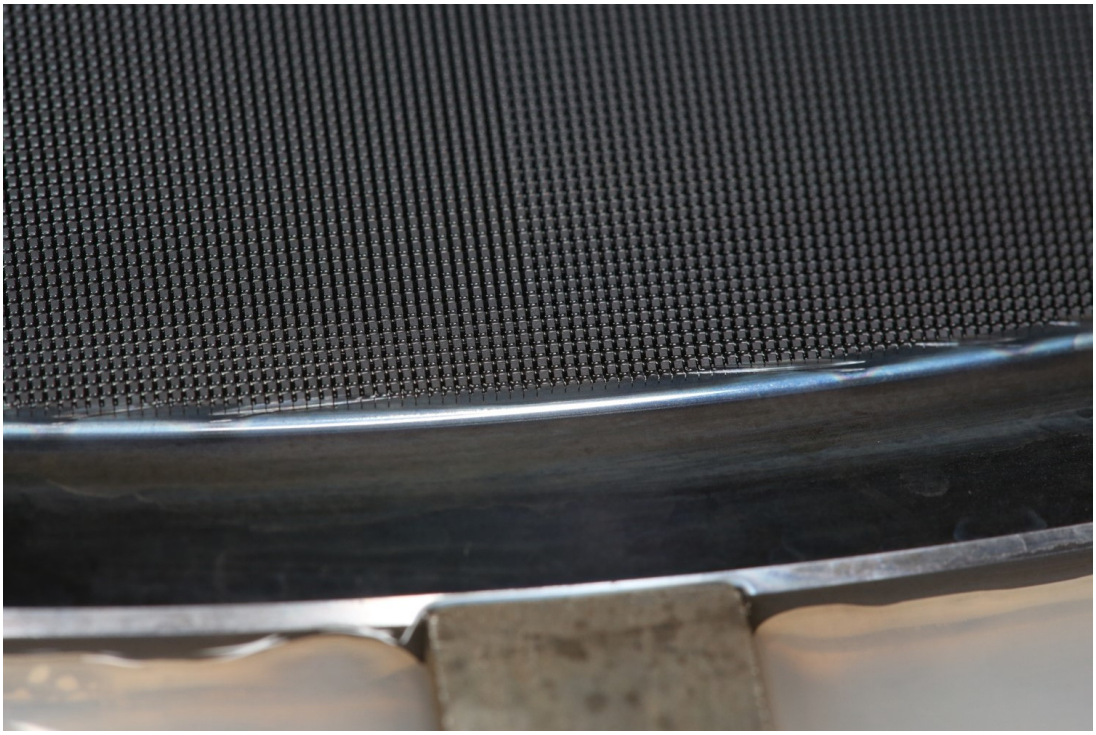

Figure 4.27: One of the ACTPol lenses with a complete 2-layer MARS cut into the surface. These structures were designed to pass the 150 GHz band.

4.13.1 ACTPol Optics

The ACTPol project required two sets of three lenses to complete the deployment of the full camera. A single set of three lenses was manufactured under contract by a commercial machine shop, with mixed results. The lenses were completed, but with a significant number of defects that compromised their ultimate performance. Additionally, the cost of outsourcing the fabrication (due to the high level of precision necessary) was ultimately unfeasible for the project, necessitating the development of the approach described here.

These two sets of lenses were successfully completed well in advance of the deployment deadlines imposed by the project, and their anti-reflection performance was excellent, in keeping with the predictions from modeling.

Further lenses and other optics for the Advanced ACTPol project (AdvACT), as well as experimental designs and optics for third parties have been successfully fabricated since the completion of the ACTPol optics, and will be briefly discussed later in this chapter.

The first set of lenses completed was for the 150 GHz single-frequency camera.

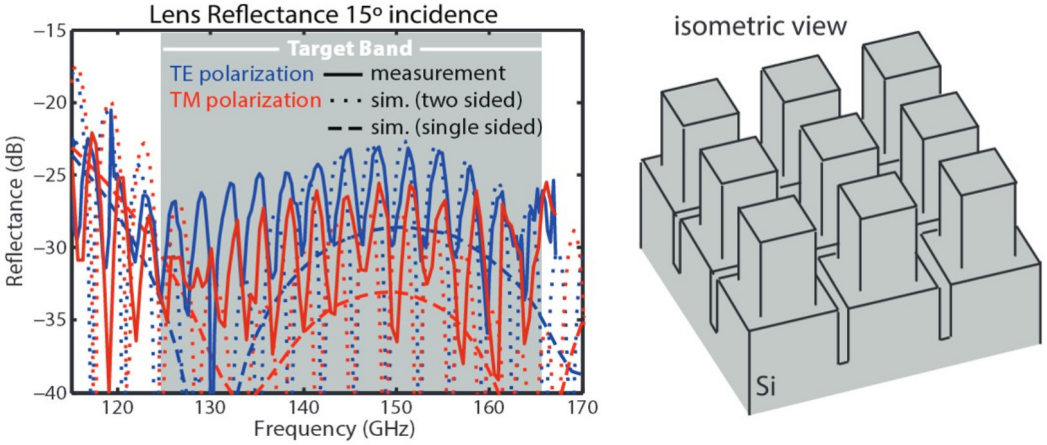

Figure 4.28: A CAD model of the 150 GHz 2-layer coating (right), and the measured and simulated performance of a complete 2-layer design (left). The performance for this coating was excellent (sub-percent across the entire band), and consistent with simulations. This measurement was taken on an early coating, with subsequent measurements setting the reflectance limit lower. Figure courtesy of Rahul Datta.

These lenses consisted of a 2-layer coating with a target central frequency of 148 GHz. Reflectometer measurements established the band-averaged reflections for this structured surface design at $\sim 0.3\%$. A model of this design, as well as a measurement of the performance, are shown in Figure 4.28. An improved measurement is shown in 4.29.

Following the successful completion of the first set of lenses, a final design was developed for a broadband coating to pass both signal bands of the 90/150 GHz multichroic pixels. The goal of this coating was high transmission between 70 and 170 Ghz, in order to maximize the sensitivity of the array in both channels simultaneously. This was achieved by adding another layer of cuts to the design, creating a structure that behaves like three stacked dielectric layers applied to the silicon surface. With this structure, we were able to achieve initial reflectance of $<1\%$ averaged across the band. Subsequent versions improved slightly over this, giving averages closer to 0.3%. These optics enabled the deployment of the first multichroic CMB instrument with the successful deployment of the 90/150 GHz ACTPol array.

The modeled and measured performance of a 3-layer structured surface is shown in Figure 4.30, and a photograph of a finished lens is shown in Figure 4.31.

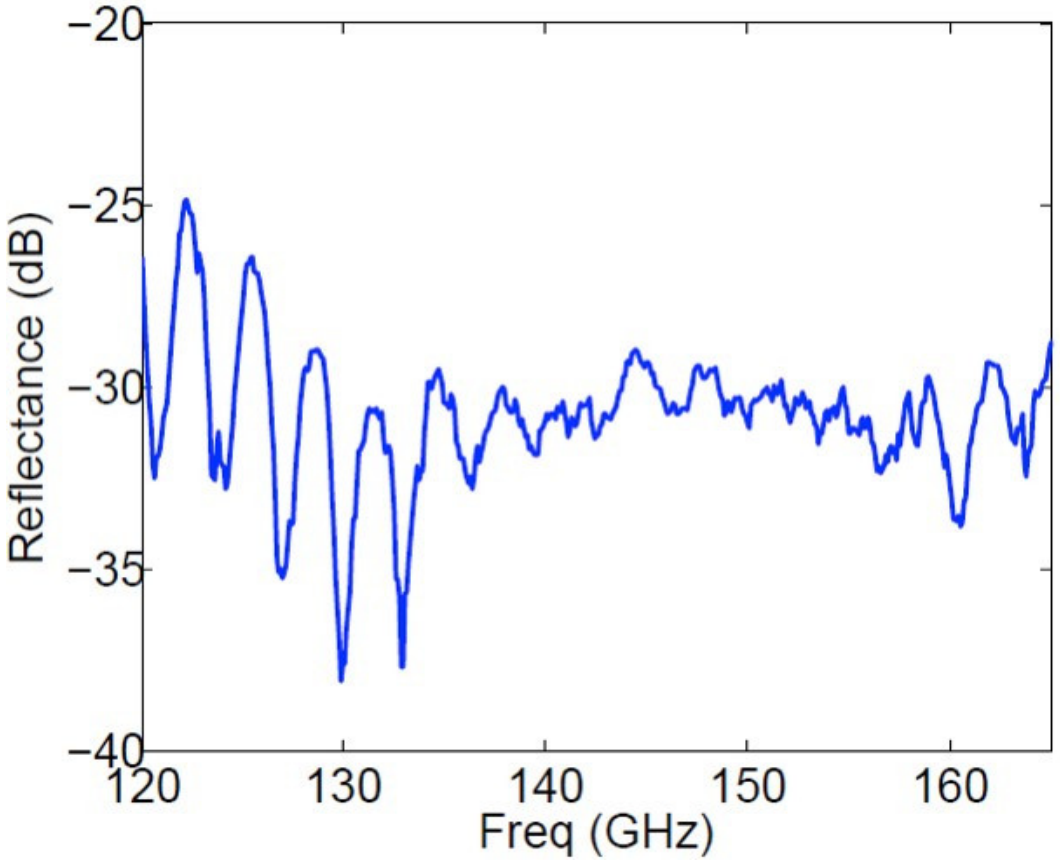

Figure 4.29: A cleaner measurement of one polarization of a 2-layer 150GHz coating. This shows typical reflectance across the band of $\sim 0.1\%$ (-30 dB) with a peak reflectance below $\sim 0.5\%$.

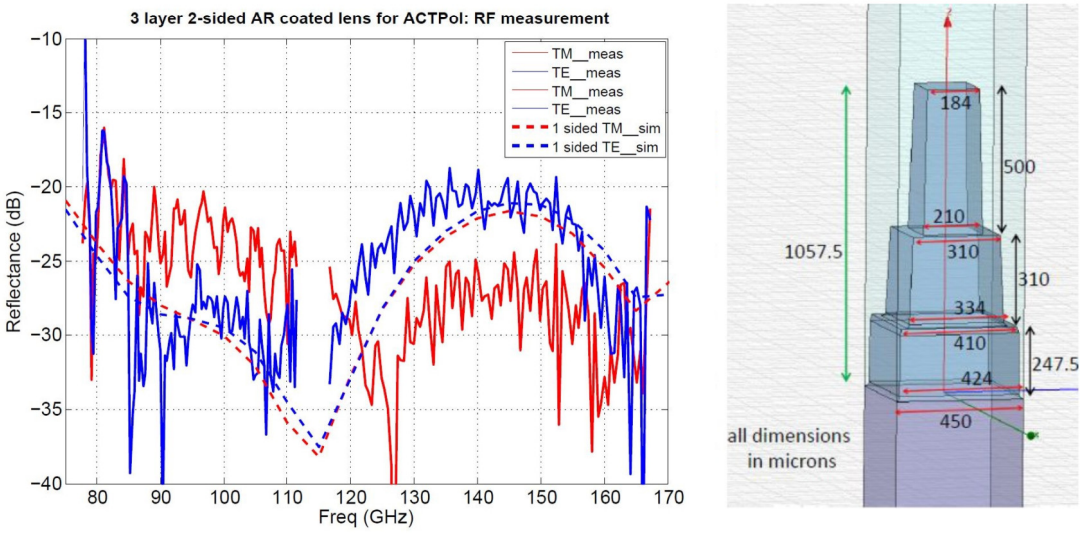

Figure 4.30: The modeled geometry (right) and measured performance (left) of a 3-layer AR surface. This coating gave $\sim 1\%$ band-averaged reflectance for the 90 and 150 GHz bands. Model and simulation courtesy of Rahul Datta.

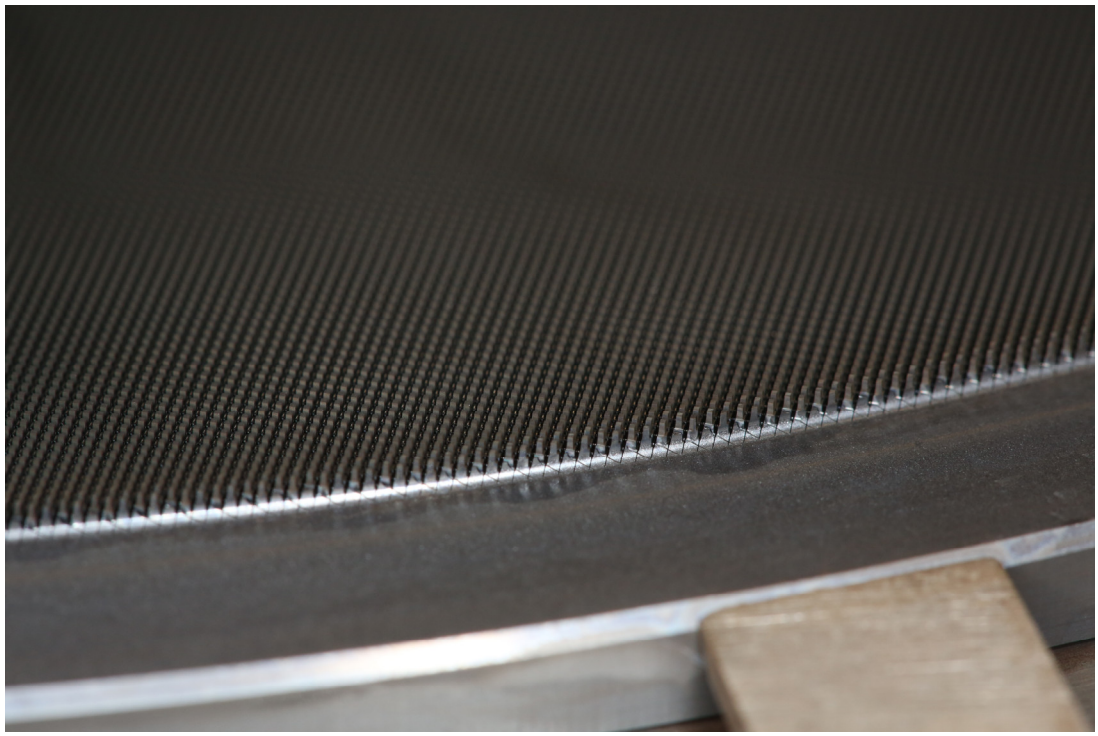

Figure 4.31: One of the ACTPol lenses coated with a broadband 70-170 GHz AR surface. These lenses enabled the deployment of the first multichroic array on the ACTPol project.

4.14 Enabling Future Technologies

The ability to fabricate subwavelength features in silicon enables a wide range of possible future technologies. The ability to couple light into and out of silicon enables the creation of complex structures via conventional lithographic techniques and machining of appropriate metamaterials. A basic exploration of this concept is the infrared blocking filters discussed in the next chapter. These surface features can also be scaled to different wavelengths, including the infrared (up to the 1 micron absorption cutoff that exists in silicon), and can be cut without rotational symmetry, so as to induce birefringence in the resulting metamaterial.

4.14.1 High Frequency MARSs

A natural extension of the AR surface treatment work required to deploy ACTpol was the development of metamaterial antireflection surfaces testing the limits of the AR fabrication system. The first experimental coating pursued was a high-frequency quarter-wave coating. The gantry was capable of delivering 1 micron precision across the full range of motion, which corresponded to the acceptable tolerances for a 1.5 THz transmission band. A sample MARS was designed and fabricated with a target transmission frequency of 1.5 THz, and its structure and performance are shown in Figure 4.32. This structured surface behaved as expected and demonstrated the applicability of this AR fabrication approach to Thz radiation. These high-frequency applications are a promising direction for future research. A design and simulated performance for an even higher frequency MARS is shown in Figure 4.33.

4.14.2 Ultra-broad band MARSs

The next natural extension of the AR surface treatment framework was to increase the number of layers, giving broader bandwidth to the final optic. A structured surface consisting of five layers was attempted, necessitating development of a modified machining procedure. A five-layer MARS was successfully manufactured covering a bandwidth from 70-350 GHz. The structure of this five-layer MARS is shown in Figure 4.34. Its simulated and measured performance are shown in Figure 4.35.

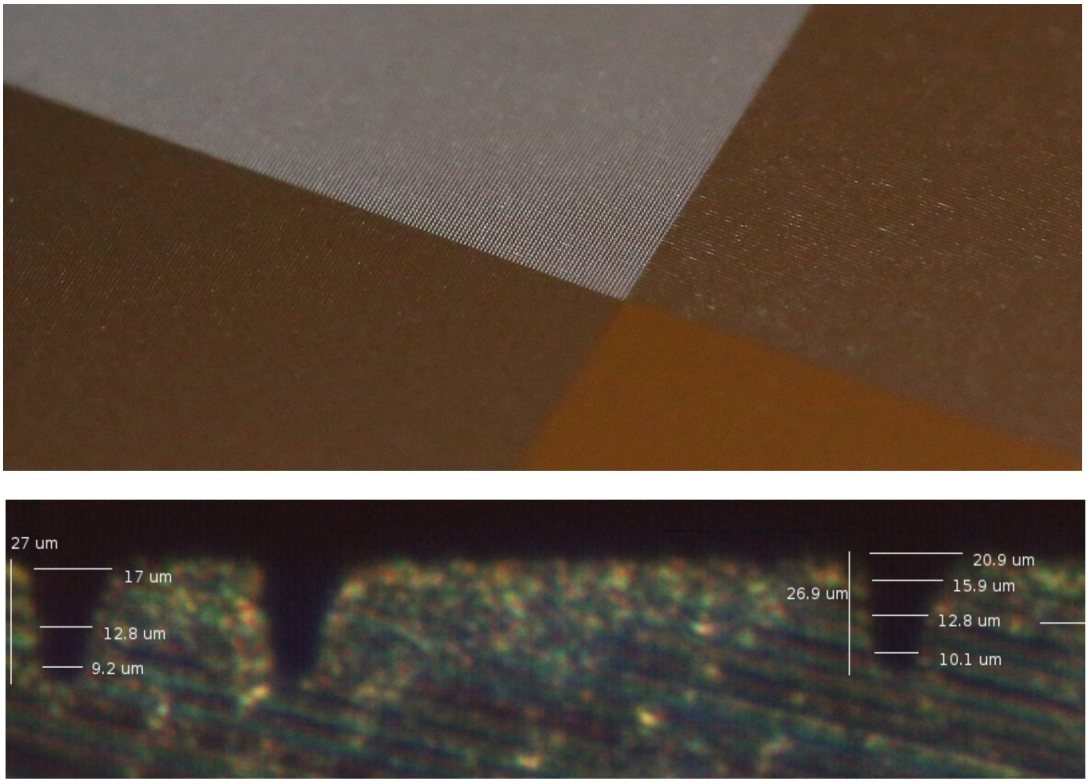

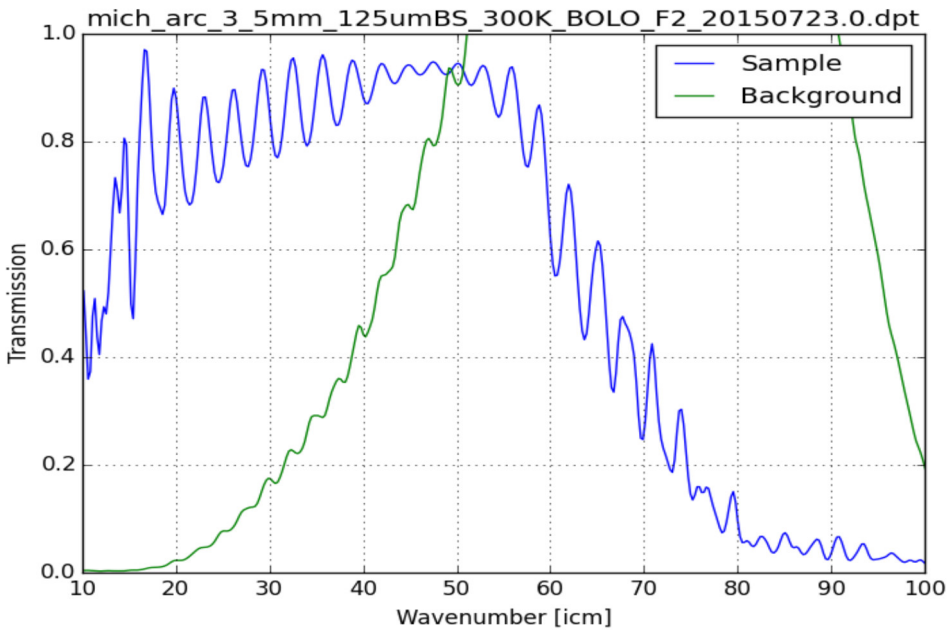

Figure 4.32: A prototype quarter-wave surface treatment designed to transmit 1.4 THz. This was made as a test of the machine capability to fabricate higher-frequency (and therefore smaller) structures. A sample is visible in the top panel, with the cut profiles in the center, and the measured performance below. This structured surface functioned as expected, demonstrating the ability to successfully fabricate THz-band structures. Measurement courtesy of Kevin Miller, NASA Goddard Space Flight Center.

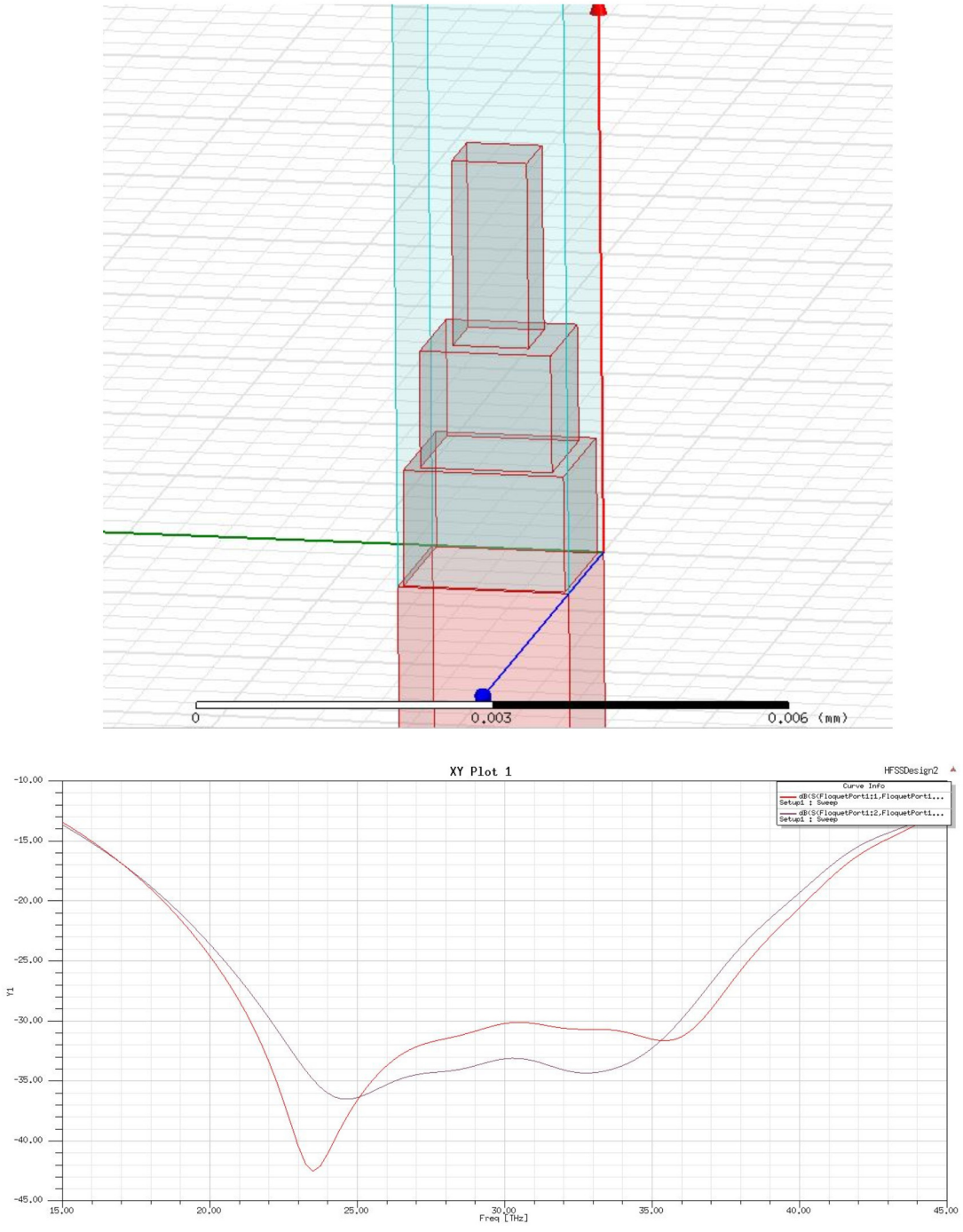

Figure 4.33: Top, a model geometry for an AR structured surface transmitting long wavelength IR radiation (in the 8-14 μm range (21-37 THz). Bottom, the simulated performance of this AR coating. Extending to much shorter wavelengths by exploring alternate fabrication techniques (such as deep reactive ion etching (DRIE) or ion beam machining) could enable variants of this technology through the infrared, and down to wavelengths of 1 micron (where silicon becomes absorptive). This particular design has feature sizes in the hundreds of nanometers, which is achievable with current nanofabrication techniques.

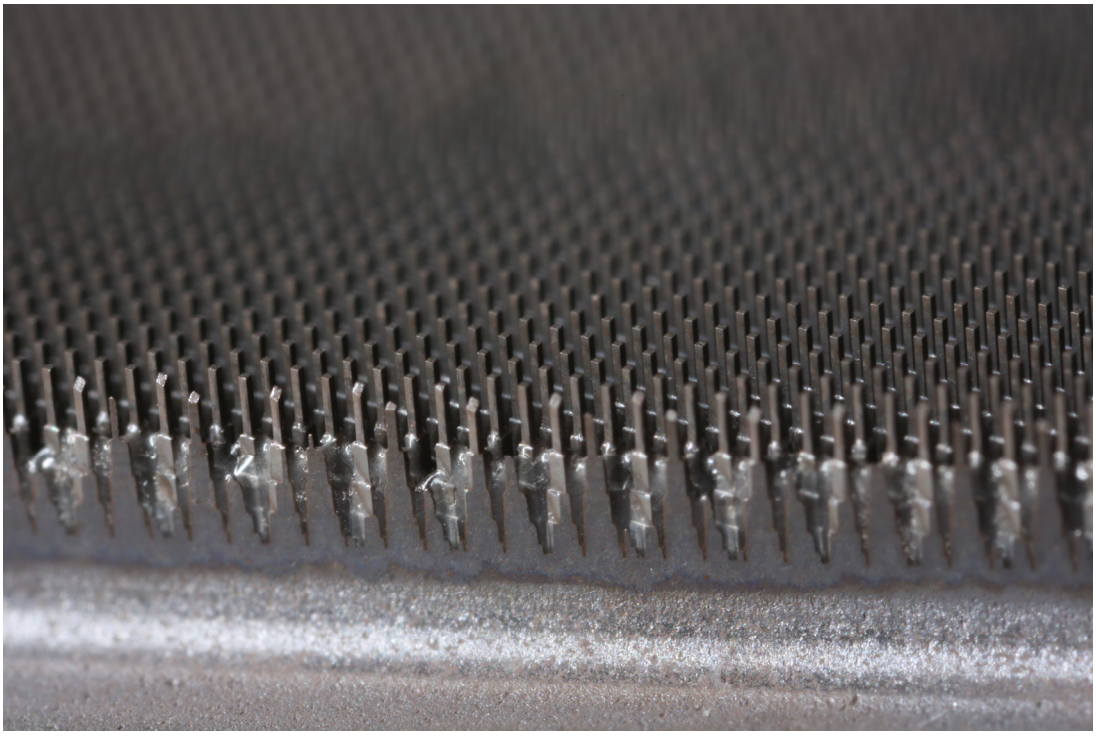

Figure 4.34: A broad bandwidth 5-layer AR structured surface prototype. This piece was made to demonstrate surface treatment approaches with additional layers, allowing more complex frequency responses and broader bandwidth than previously fabricated versions.

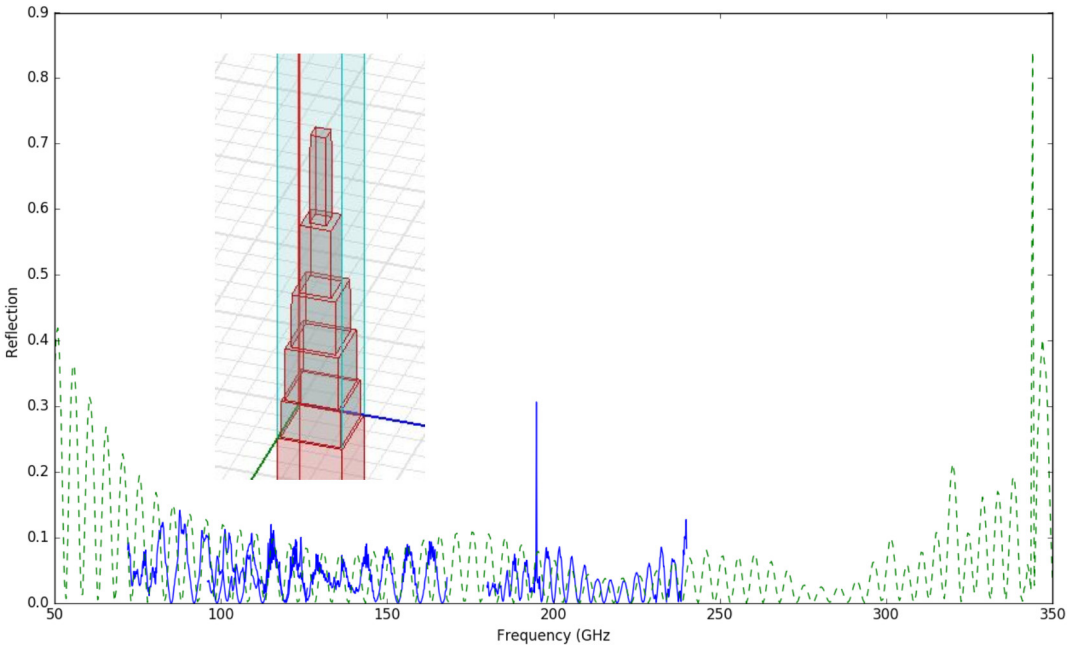

Figure 4.35: The measured (blue) and simulated (green dashed) performance of the 5-layer metamaterial antireflection surface, showing excellent performance from 70 to 350 GHz, and good agreement between measurement and simulation. Inset, the HFSS geometry used for modeling. Figure components courtesy of Kevin Coughlin.

4.14.3 Anisotropic Metamaterials

This approach to sub-wavelength surface modification also provides the capability of creating anisotropic materials. By cutting patterns that aren't symmetric under a 90 degree rotation, one can create a material that exhibits effective birefringence, giving fast- and slow-axis indices covering a wide range of values. This concept has been explored by Kevin Coughlin with excellent results, and will be important to the next-generation of CMB telescopes using rotating waveplates to probe large-angular scale polarization.

Chapter 5

Composite Reflective/Absorptive IR-Blocking Filters Embedded in Metamaterial Anti-Reflection Structured Silicon

The development of effective metamaterial anti-reflection silicon enables a wide host of derivative technologies, due largely to useful characteristics of the silicon substrate (low loss, high strength, and high thermal conductivity)and well-developed silicon fabrication capabilities derived from the semiconductor industry. In this chapter, I describe the development of a infrared-blocking filter based around metamaterial silicon. This serves as both a demonstrator for silicon-substrate filters and addresses limitations of current infrared filters that believed to limit the sensitivity of the ACTPol project.

5.1 Introduction

Infrared (IR) blocking filters are critical for optimizing the performance of bolometric detectors in the millimeter and submillimeter regions of the electromagnetic spectrum. In these bands, the IR power emitted from the telescope and surroundings (typically 250-300K for ground and balloon-based in-

struments) is significantly brighter than the sky background at mm wavelengths. It is therefore crucial to significantly attenuate this out-of-band power. Filters serve to substantially reduce what would be a dominant source of detector noise and minimize the radiative loading on the cryogenic system. In addition, filters must not radiate noise in the band of interest or significantly absorb or scatter the incoming signals. This requires high thermal conductivity and good heat sinking for any filter containing absorptive components.

Meeting these requirements has repeatedly proven itself to be a difficult instrumental challenge. This challenge has been approached in several different ways, most commonly with reflective frequency selective surfaces (patterned onto thin plastic substrates and stacked, as pioneered by Ulrich [71], [72], and summarized by Ade [73]) and bulk filters of absorptive materials (such as Alumina [74]). Scattering filters have also been used [75]. These filtering approaches, however, are not without their complications. The reflective filters patterned on plastic substrates are subject to the intrinsic limits of multi-layered reflectors (i.e. that additional reflective layers decrease the total rejection only incrementally) as well as heating due to absorption of the plastic (which in turn leads to reradiated power that falls onto detectors)[73]. Absorptive filters, such as those made of bulk Alumina, present difficulties with anti-reflection coatings, requiring the use of lossy materials that reduce the overall transmission in the desired pass-band [74]. In this work we present an example of a hybrid approach based on a combination of reflective frequency selective structures patterned on silicon substrates, scattering and absorptive layers based on composites of powdered crystals exhibiting the Reststrahlen effect embedded in an epoxy binder, and metamaterial antireflection coatings to control the in-band reflections from the vacuum-silicon interfaces. We present a particular example of the construction of a blocking filter designed to pass the 70-170 GHz band in Section 5.2, and discuss its performance in Section 5.4. We conclude with a discussion of the scalability and applicability of this design in Section 5.6.

5.2 Composite Filter Construction

Figure 5.1 shows the anatomy of our composite absorptive/reflective IR-blocking filter. This filter consists of lithographically defined frequency selective surfaces

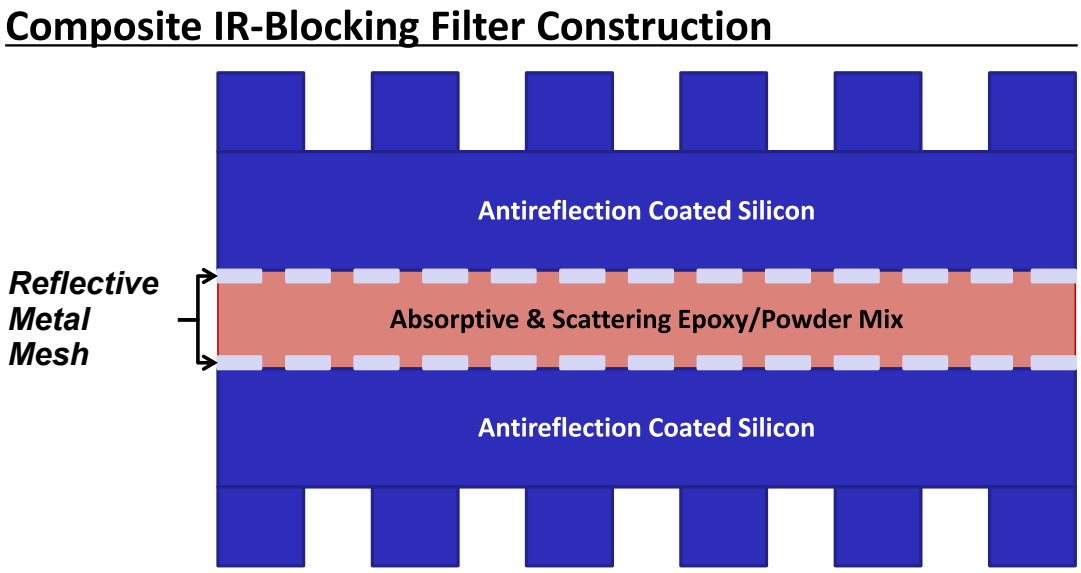

Figure 5.1: Our silicon-substrate composite filter is composed of several components. In the pass-band, the metamaterial antireflection coated silicon couples light into and out of the filter stack from free space. In the stop-band, a set of lithographically patterned reflective metal features reflect a significant portion of the incident light, and an absorptive and scattering layer of optical epoxy loaded with powdered Reststrahlen materials blocks much of the remaining light.

patterned on two silicon wafers, a $25\mu m$ layer of an absorptive mixture of epoxy and reststrahlen powders placed between the two patterned surfaces, and a metamaterial antireflection coating on both vacuum silicon interfaces. At IR wavelengths, light is reflected off the front silicon wafer and frequency selective surface. The front metamaterial surface scatters light both specularly and diffusely for frequencies above the single-moded limit of the structure. For the metamaterial surfaces described here (tuned to pass 1-2mm wavelengths), this falls well below the infrared emission from a 300K blackbody, which peaks at $10\mu m$. Infrared light that passes the frequency selective metal mesh is subject to both scattering and absorption by the reststrahlen-epoxy composite. An additional metal mesh layer reflects most of the remaining light back into the epoxy-powder layer, boosting absorption and (to a lesser extent) reflection. This approach reduces the load on the cryogenic stage by reflecting a significant portion of the IR power, and uses an absorbing layer to further attenuate IR power passing the first reflective layer at arbitrary angles of incidence.

At millimeter and sub millimeter wavelengths the frequency selective surfaces have a high transmission, and the absorbing layer is inconsequentially thin leading to low absorption. Thus in the bands of interest, this structure behaves nearly as if it were a slab of solid low loss silicon treated with a high quality antireflection coating [13].

In the remainder of this section we describe the design and performance of the frequency selective surfaces, powder-epoxy mixes , metamaterial antireflection coatings, and conclude with predictions for the integrated performance of our filters.

5.2.1 Frequency Selective Metal Mesh Filters

The first filtering component of these composite IR-blocking filters is a low-pass frequency selective surface formed by a mesh of resonant metal squares separated by gaps. These squares act as a grid of capacitive elements and pass low frequencies while reflecting high frequencies. In the low frequency limit, the metallization layer is effectively nonexistent giving nearly perfect transmission, and in the high frequency limit, these features reflect according to the fill factor of the metallization. In the resonant region between, there is some additional reflection, with the cutoff frequency set by the grid spacing. We selected the

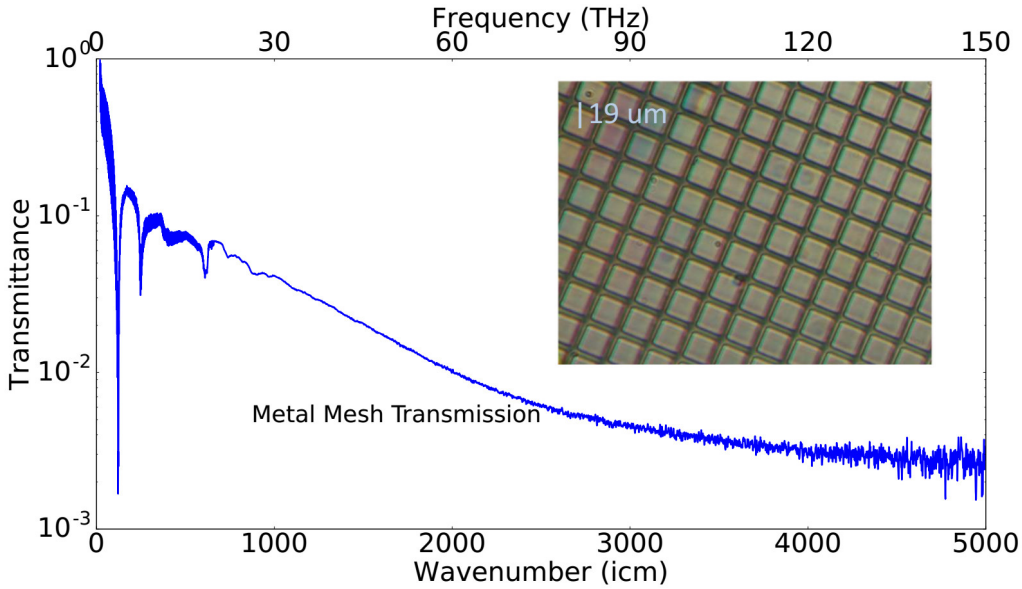

Figure 5.2: The reflectance of a frequency selective surface formed by lithographically patterned aluminum squares on a silicon substrate. Inset, a photograph of this sample.

grid parameters to place the cutoff frequency well above the upper end of our desired signal band (170 GHz), but below the peak of a 300K blackbody (18 THz). We selected a grid period of $23.75\mu m$ and gap widths of $5\mu m$, for a cutoff frequency in silicon of 3.6 THz (corresponding to a freespace wavenumber of 120 icm [72], clearly visible as the first resonance in the measurement in Figure 5.2). These dimensions were additionally constrained to be within the capabilities of large-diameter liftoff lithographic techniques (limiting us to minimum features of few micron scales). A prototype of this design was thoroughly characterized (see Figure 5.2), and the performance is in good agreement with our theoretical expectations, with a total reflectivity of 83% for a 300K blackbody.

These features are straightforward to tune to a desired cutoff frequency and can be fabricated on the silicon using standard lithographic techniques. Design of these features was carried out via the techniques described by Ulrich [71], with additional design and verification via modeling in Ansys HFSS [69].

5.2.2 Reststrahlen Materials and Powder Filters

The Reststrahlen Effect, from the German for "residual rays," is the absorption of light at characteristic frequencies [76] of the bound ion pairs in crystalline materials that falls in the infrared [77], [78]. These structural resonances prevent light in the Reststrahlen band from propagating through the material, and effective low-pass filters have been previously demonstrated by suspending powdered Reststrahlen filters in sheets of polyethylene [77]. Reststrahlen materials have also been used, as large crystals, as both transmissive and reflective filters in other applications [78].

Powder Filters, formed by Reststrahlen powders mixed into a polyethylene carrier, were demonstrated as IR blocking filters by Yamada et al. [77] These filters, due to their plastic carrier, suffered from heating and reradiation. We fabricated similar powder filters by mixing Reststrahlen powders into a mixture of toluene thinned Epotek 301 optical epoxy and applying thin layers through a commercial spraygun mounted on a robotic gantry. This allowed for application of thin ($25\mu m$) uniform layers of the epoxy-powder composite. The powders were chosen from the assortment of materials characterized by Yamada [77] to provide good blocking coverage for wavelengths from $<10\mu m$ up to $150\mu m$ (corresponding to 67-1000+ icm), overlapping transmissive regions of one powder with absorptive regions of another. Additionally, the powders were chosen for ease of use and acquisition, limiting us to non-hazardous materials (excluding materials such as thallium and beryllium salts, which have been previously used [77]) that are common chemical reagents. As a result of these constraints, our filters consist of magnesium oxide (MgO) and calcium carbonate ($CaCO_3$), both with 5-20μm typical particle sizes. See Table 5.1 for the composition of the reststrahlen composite layer. The measured optical transmissions for these powder filters are shown in Figure 5.3. These measured transmissions exhibit the characteristic absorption features expected for both materials (see [77] and [78]). We combined these powders in equal parts (by mass) to toluene thinned Epotek 301 and applied it with the spraygun. For the full composite filter, this epoxy layer also adhered the two silicon wafers together. The particle size is sufficiently small that the epoxy layer can be treated as a dielectric mixture that is well described by mean field effective medium approximations [79] in the instrument band of 70-170 GHz (see Figure 5.6).

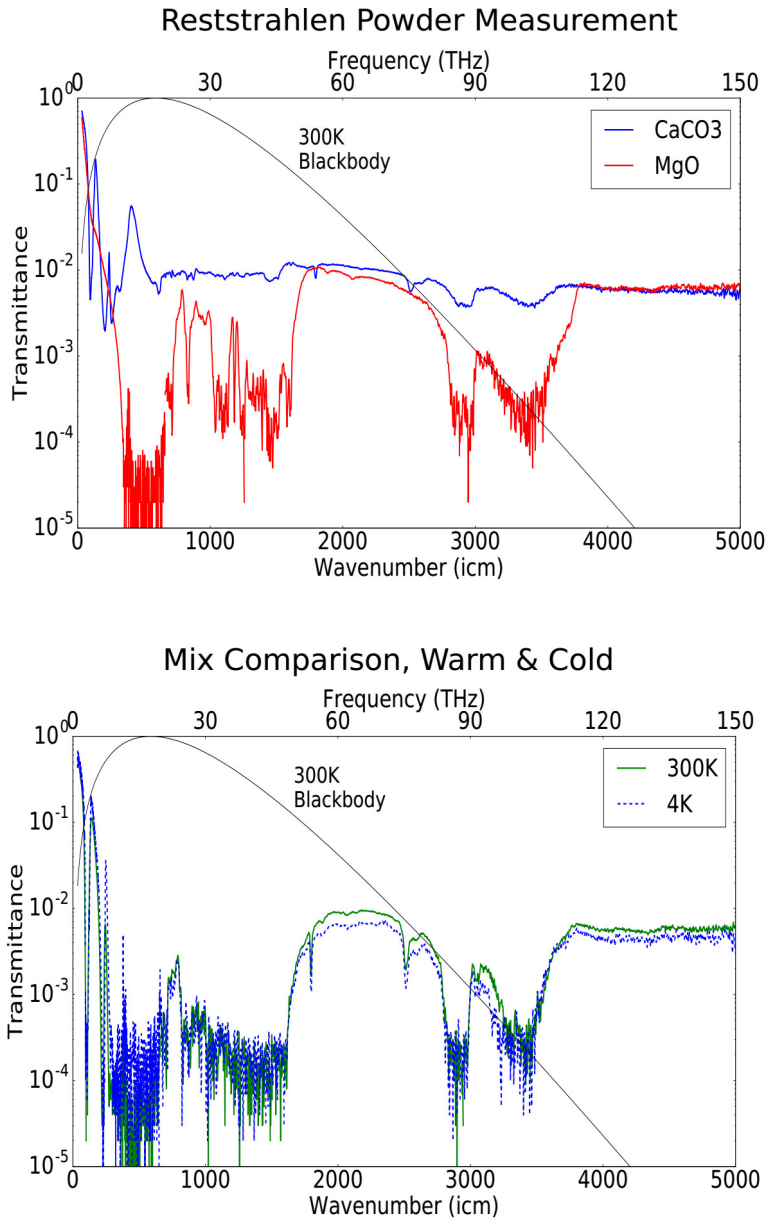

Figure 5.3: Top: An FTS measurement of $CaCO_3$ and MgO powder filters, demonstrating good blocking performance and reproduction of the characteristic Reststrahlen absorption bands at the appropriate frequencies. Bottom: The measured performance of a $CaCO_3/MgO$ mix powder filter warm (at 300K) and cold (at 4K) showing minimal changes to the absorption characteristics and demonstrating suitability of this technology for cryogenic IR blocking filters.

Material	Particle Size	Volume Fraction	ϵ_r
$CaCO_3$	5-20 μm	0.092	8.45
MgO	5-20 μm	0.073	9.8
Epotek 301	N/A	0.835	3.7 + 0.1i
Mixture	N/A	1.00	4.35 + 0.095i

Table 5.1: The composition of the epoxy composite layer.

The Cold Performance was characterized to ensure proper cryogenic functioning of these filters. It is known that some Reststrahlen materials have absorption bands that open up when the material is cooled down. In particular, alumina (Al_2O_3) is known to have a section of its absorption band (between 30 and 300 microns) open up at temperatures of tens of Kelvin [80], [81]. To explore whether this would be problematic with our chosen Reststrahlen materials, a powder filter consisting of our mixture of $CaCO_3$ and MgO was measured in an FTS at a range of temperatures between 4K and 300K. Plots of the extremal temperatures are shown in the right panel of Figure 5.3. From this, it is apparent that changes in the absorption spectrum are minimal, and do not compromise the filtering performance of a 300K blackbody significantly.

5.2.3 Metamaterial Antireflection Silicon Surfaces

High resistivity silicon is an excellent material for millimeter and submillimeter wave optics. The very low loss (tan δ <7e-5) [13] and high refractive index allows for refractive optics with negligible loss. High purity, single-crystal silicon is available in large diameters and can be readily obtained. Additionally, silicon has a high thermal conductivity ($>$ 2 kW/m/K [62]), which prevents filters with an absorptive component from heating up. The high refractive index of silicon presents the problem of high reflectivity for optics, but this problem has been successfully managed by the application of a machined sub-wavelength anti-reflective surface to the outer surfaces of the optics. These features allow for the creation of anti-reflection "coatings" with simulated dielectric layers. These metamaterial anti-reflection surfaces allow for high transmission optics (>99% transmission across a 70-170 GHz band for a three-layer simulated dielectric coating [9]) to be fabricated from entirely silicon. A thorough discussion of this anti-reflection surface treatment approach is given in Datta et al [13]. Figure 5.4 shows a photograph of a three-layer "coating" as well as a comparison of the simulated and measured reflection for two orthogonal polarizations.

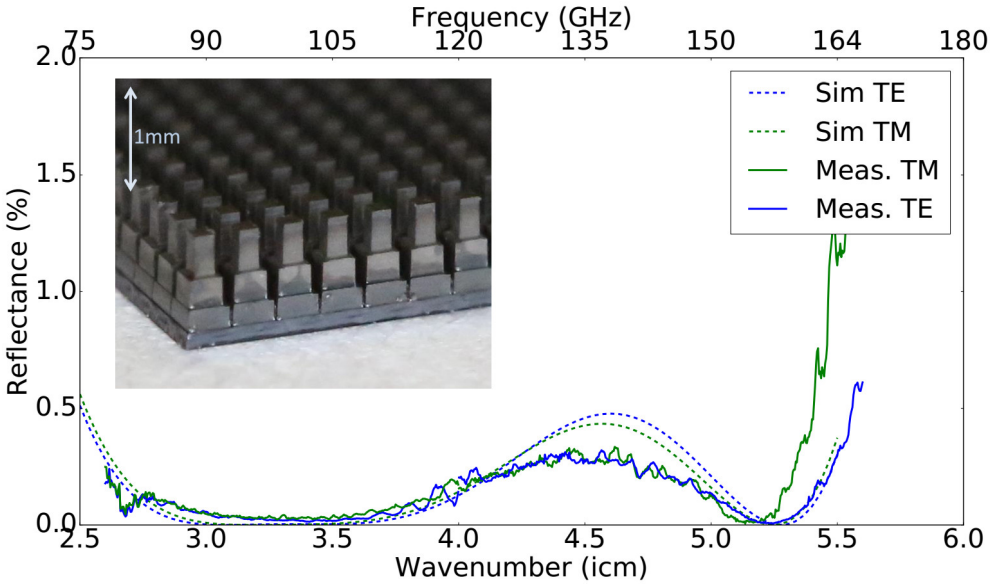

Figure 5.4: The performance of a three-layer metamaterial surface for the 90 GHz and 150GHz Cosmic Microwave Background observing bands, demonstrating good agreement with simulated performance (from HFSS) and reflections below 0.5% averaged across the signal band. Inset: A photograph of a sample of metamaterial anti-reflection silicon, consisting of three simulated dielectric layers of machined subwavelength features. Measurement courtesy of Kevin Coughlin.

5.3 Composite Filter Fabrication

Prototype filters were fabricated using facilities at the University of Michigan. Sample filters were made to test the full range of constituent components, as well as combinations thereof. Lithographic fabrication was done at the Lurie Nanofabrication Facility [1], and the absorptive layers were sprayed using a custom spray-coating machine made from linear stages and a pneumatically controlled High Volume Low Pressure (HVLP) spraygun fed by a continuously mixing pressurized tank. This system was able to successfully spray both the straight epoxy (a mixture of just Epotek 301 and toluene), and the epoxy loaded with scatterers.

5.4 Composite Filter Performance

The performance of our composite filters was evaluated using Fourier Transform Spectrometer (FTS) measurements, as well as integrated measurements made in a cryostat open to a 300K blackbody. The spectrometry of the filter components and composite filter were carried out using a Bruker IFS 125 Fourier Transform Infrared Spectrometer[2] (FTS), while the integrated test was carried out using a carbon loaded disk bolometer in a custom cryostat setup. The performance of the individual components was measured across both the low-frequency signal band (down to 10 icm (300 GHz) limited by the low frequency capability of the FTS) and high-frequency blocking band (up to 5000 inverse cm, 150 THz). Additionally, the overall performance of a full composite was measured across the blocking band.

Measurement Methods: The reflectance and transmittance in the range 10-5,000 icm (0.3-150 THz) were measured with the Bruker 125 FTS using the following two combinations of source-beamsplitter-detector: Hg arc lamp-multilayer mylar-liquid helium cooled bolometer (30-700 icm), and globar-Ge-coated KBr-DLATGS (500-5,000 icm) (Potassium Bromide - Deuterated Lanthanum α Alanine doped TriGlycine). The spectral response in the overlap region agreed to within 0.5%. The data sets were merged into one spectra by

[1] lnf.umich.edu

[2] This instrument is located at the NASA Goddard Space Flight Center, and measurements were made as part of the NASA Space Technology Research Fellowship

equating the areas underneath the curves in the overlap region using a weighted average. The reflectance was measured in a collimated beam geometry with an 8° angle of incidence. The transmittance was measured in a focused beam (f/6.5) geometry at normal incidence. The total hemispherical transmittance in the range 500-5,000 icm was collected using a Bruker-made integrating sphere (75 mm diameter) accessory for the FTS with its own internal DLATGS detector. A diffusely reflecting gold surface, which matches the inner surface of the sphere, was placed over the sample port to collect the reference scan.

For integrated testing, a 3-stage cryostat was used to measure the radiative properties of the composite filter. A 5.8 cm diameter disk bolometer was held at a base temperature of 5K. The filter was mounted on the 20K stage directly above the bolometer, and blocked light being emitted from a blackbody at 300K visible through a hole in the lid of the 100K stage. The total power blocked by the filter was then estimated by measuring the bolometer temperature with and without the filter. Additionally, the heating of the 20K stage was measured to estimate the power absorbed by the filter, and the filter temperature was measured at several points to measure localized heating in the center of the filter (relative to the edge) and heating of the entire filter relative to the 20K stage. See Figure 5.6 for a schematic of the cryostat.

IR Blocking Performance: The infrared blocking performance of these filters was measured on an FTS up to 5000 icm (2 um wavelength, 150 THz), giving a full characterization of the transmission across the spectrum of a 300K blackbody. These measurements reproduce the characteristic Reststrahlen powder filter shape in thicker (75 um) layers [77], and demonstrate excellent IR blocking in layers as thin as 25 um.

In the FTS measurements, the composite filter specularly reflected >40 % of the light incident from a 300K blackbody (indicating reflection off the front silicon surface and metal mesh features), and diffusely reflected another 10%, indicative of backscattering off the powder layer. The overall reflectance was lower than would be naively expected from the single reflector measurements in Section 5.2.1. This is likely explained by coupling of fields from the reflectors into the lossy epoxy composite below. Should higher reflectivity be needed, the reflective layers could be separated from the lossy composite and multiple reflective layers could be employed.

Low Frequency Performance: The low frequency performance of a 75um layer of the powder filter component was measured down to 10 icm (300 GHz) using an FTS. These data were then fit with a simple transmission line model. The index of the powder layer was estimated via a Maxwell-Garnett effective medium approximation [66], and treated as a layer of continuous material of an unknown thickness. The thickness of this layer and the underlying silicon layer were then fit using a standard least-squares approach. For a 75um mix layer (consisting of a binder of Epotek 301, $\epsilon_r = 3.7 + 0.1i$ as measured in the 1-10 THz range with a sample etalon formed by silicon wafers, loaded with powdered MgO, $\epsilon_r = 9.8$, and $CaCO_3$, $\epsilon_r = 8.45$ in 0.073 and 0.092 volumetric fractions respectively) on 500um thick silicon ($\epsilon_r = 11.67$), the model accurately reproduced the measured total thickness. This model was then used to extrapolate to lower frequencies and simulate the effect of adding a three-layer antireflective surface treatment to a filter made using this material. This model shows that the Reststrahlen powder filter introduces minimal loss (dominated by the epoxy carrier) in a signal band from 70-170 GHz, and that an instrument-band transmission of >99% should be achievable for a filter using this technology (with the total transmission limited by the antireflection coating performance). In the low frequency region, the filter performance is well represented with a simple transmission line model, taking into account the effective index of the composite determined from an effective medium approximation. The measured and modeled low frequency performance is shown in Figure 5.6.

Thermal Performance and Cryostat testing: An integrated test of the composite filter performance was carried out in a cryostat, to measure the total blocking efficiency of a 15cm diameter prototype. A drawing of this test setup is shown in Figure 5.6, in the right panel. For a 15cm diameter sample composite filter, there was negligible heating of the center of the filter (with thermal gradients of less than 1K from center to edge) when the filter was cooled to 20K and used to block the power from a 7cm diameter window open to 300K. The filter as a whole heated to 2K above the stage temperature, demonstrating effective heatsinking and power removal from the filter as well. In this configuration, the power deposited on a carbon disk bolometer at 5K was measured, and this measurement established a lower limit on the blocking of >98% of a 300K blackbody. This lower limit is in agreement with the FTS measurements of the full composite filter.

5.5 Frequency Range of Applicability

The components of this style of silicon substrate composite filters all have applicability across a broad range of frequencies. The limiting frequencies for the different components vary, but filters can be constructed using these techniques and some subset of the components for frequencies ranging from tens of gigahertz to hundreds of terahertz depending on the components used. The frequency scaling of each of the 4 important components is discussed in this section. The combination of several of these components can form effective filters across a wide range of frequencies.

5.5.1 Frequency Selective Metal Features

The frequency selective metal mesh features can be fabricated across the full range of sizes available with modern lithographic techniques. This results in applicability across the full range over which silicon is transparent, up to the beginning of the absorption band at 1 micron wavelength (300 THz). Silicon, as a rigid substrate, offers better control and repeatability of lithographic features than existing plastic substrates, which mean that smaller features (and therefore higher frequencies) can be attained. Additionally, the metal features can be formed with both high- and low-pass frequency responses, as well as with anisotropy, which enable a range of filtering characteristics, including band-defining filters, and filters with polarization dependence.

5.5.2 Silicon Substrate

The silicon substrate offers excellent transmission performance from low frequencies up to the beginning of its absorption band in the near-infrared. It begins to become absorptive at a wavelength of approximately 1 micron (corresponding to a frequency of 300 THz). At frequencies lower than this (longer wavelengths), it remains highly transmissive and very low loss.

5.5.3 Antireflective Coatings

The metamaterial antireflective surfaces have applicability to a similarly broad range of frequencies. At lower frequencies, the structures can be machined

into the surfaces using a dicing saw or conventional grinding techniques. This approach to the antireflection coatings has been successfully demonstrated for frequencies up to 1.5 THz with excellent performance.

At higher frequencies, higher precision fabrication approaches become necessary. Using laser machining to cut smaller features is one option, up to the limits of current laser machining capabilities. Additionally, lithographic techniques involving the patterning of the surface and etching of features, such as deep reactive ion etching (DRIE) offer a solution to still higher frequencies, with attainable feature sizes of tens of nanometers that would be suitable for antireflection coatings well above the 1 micron absorption cutoff of silicon.

For higher frequency and non-cryogenic applications, conventional antireflection coating approaches can also be used, substituting layers of bulk dielectric materials (or applied thin films of dielectric materials) for the simulated dielectric formed by the metamaterial silicon.

5.5.4 Scattering and Absorptive Powder

The scattering and absorptive powder layer has a relatively low high frequency limit. the particulate size of the powders can be selected to move the scattering peak to higher or lower frequencies as needed, but the absorption bands of the materials are fixed by the material choice. For some applications, suitable materials are available that will enhance the overall light rejection of the filter. For filters where blocking in these bands is not desired, the scattering and absorptive powder can be removed from the design. The epoxy binder can likewise be removed in favor of direct bonding the wafers, for applications where the epoxy would increase the loss and is not needed as a carrier for scattering and absorptive powders.

Comparison to Competing Filter Technologies Compared to existing reflective filters, built of reflective frequency selective surfaces patterned onto plastic substrates and stacked, our filters offer several distinct advantages. The high thermal conductivity of silicon and low absorption means that there is negligible heating of the filter center relative to the heatsunk edge. Additionally, silicon is a stiffer, more mechanically robust substrate, which allows for better control of lithographic features and finished filters that are stronger and less

susceptible to deformation and wrinkling due to thermal cycling. The composite construction of our filters additionally integrates absorptive components to improve the overall out-of-band rejection beyond what can be attained with a reasonable number of stacked reflective components.

Compared to bulk absorptive filters such as alumina, our filters offer the ability to reflectively reject a significant portion of the power, reducing the load on the cryogenic system. The Reststrahlen materials used (being simple reagent grade powders) are easier to source than the specific sintered alumina needed to get sufficiently low in-band loss. The use of multiple Reststrahlen materials allows for selection of complementary sets of materials that improves the frequency coverage and prevents sections of the band from becoming transmissive (such as happens with alumina when cooled). Silicon is a lower loss material than alumina and the antireflection coatings, being metamaterial silicon, are significantly lower loss than the epoxies used to antireflection coat bulk alumina filters. Finally, the composite filter offers a number of adjustable parameters not present in bulk filters that allow better tailoring of the filter characteristics to achieve the desired performance.

5.6 Potential Applications

In addition to forming effective free-space IR blocking filters, this filtering approach offers several novel possibilities for silicon-substrate optical elements. Lower frequency-selective metal elements can be incorporated into these filters to aid in defining the instrument signal band. Anisotropic application of these filtering techniques can form birefringent materials. These filters can be easily and inexpensively integrated into other optical components, such as silicon lenses.

Filters with higher cutoff frequencies and better uniformity can also be constructed for effectively blocking higher frequencies (into the mid-IR and higher) due to the high quality of silicon substrates available (superior material properties and surface finish allow for finer lithography, leading to better high frequency performance, a current limit of plastic-substrate filters [73]). The frequency range can be tuned by adjusting the reflective grid parameters, the scattering particle size, and the specific material used for scatterers, and multi-layer reflective structures can be formed to increase the overall reflectivity. Direct

wafer bonding can reduce or eliminate the necessity for lossy epoxy components, and reflective layers can be very precisely spaced using standard lithographic techniques to set the layer thicknesses. Collectively, these techniques will further improve control of the filter properties, enabling higher performance and better customization of the filter characteristics to the desired application.

Finally, more complex metamaterial behaviors can be added through more complicated lithographic features and machined subwavelength features. This enables a wide array of novel optical characteristics with potentially broad consequences for future imaging systems.

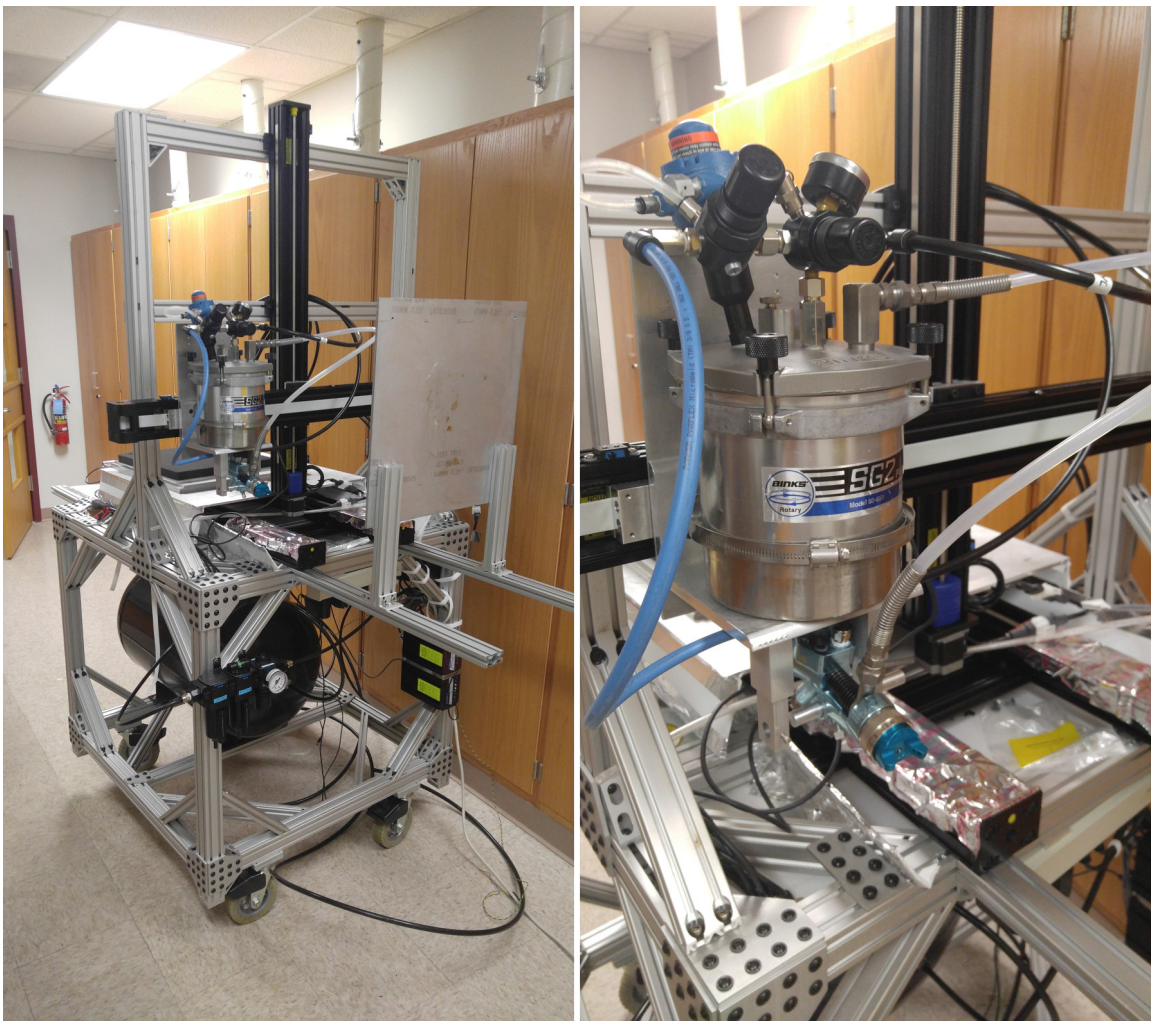

Figure 5.5: A custom spray coating machine (left: full machine, right:sprayer detail), constructed from linear motion stages and a pneumatically actuated HVLP sprayer. This system takes the mixture of epoxy, toluene, and powders, continually agitates it in a pressure vessel (right picture, center of frame), then sprays it out of an HVLP spraygun (in blue, below the pressure vessel) to achieve carefully controlled layers.

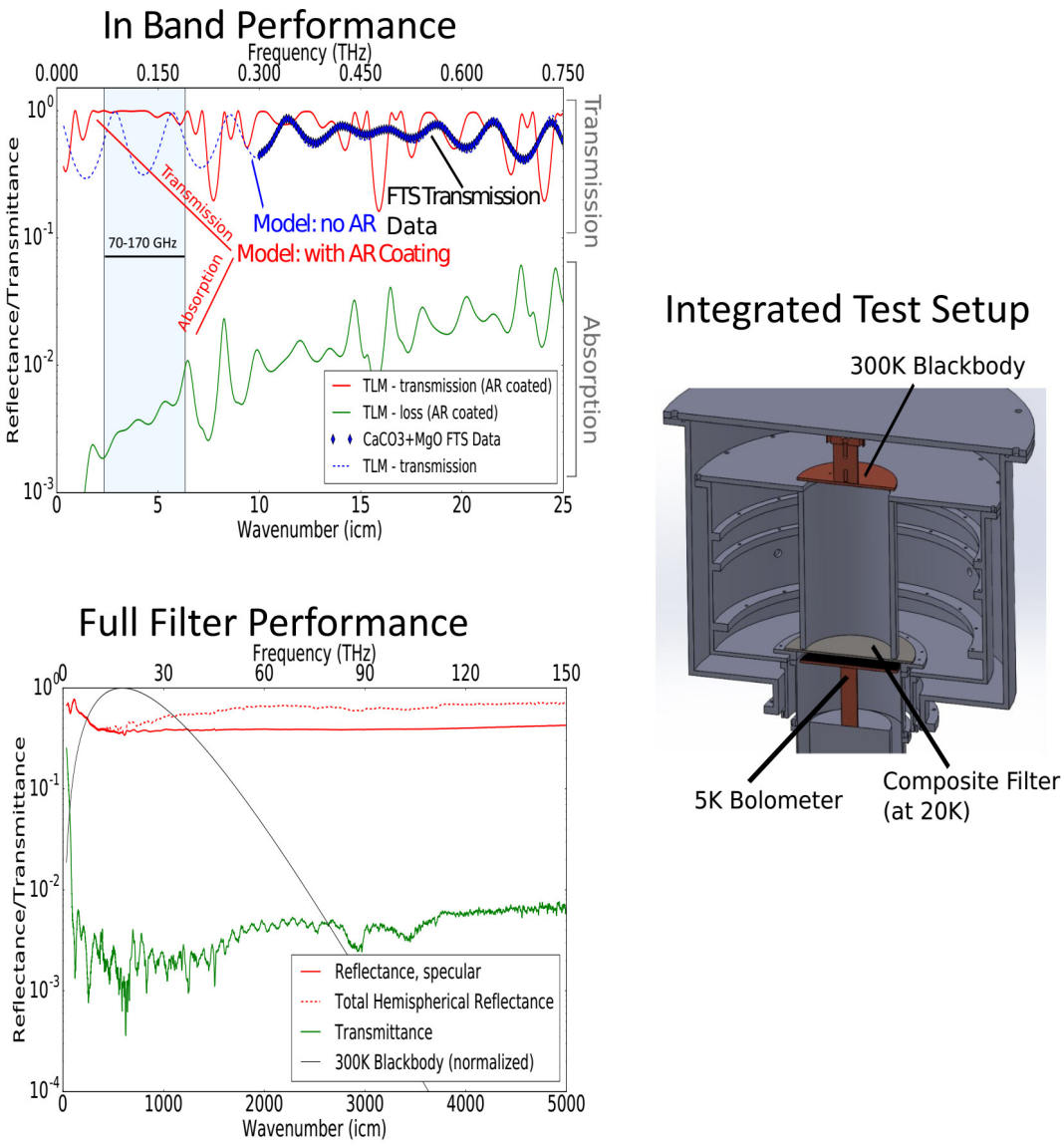

Figure 5.6: The performance of composite filter components. Top Left: The measured (blue diamonds), and simulated (blue dashed) low frequency performance for a single 75um layer of Reststrahlen powder mix, in epoxy, on a silicon wafer. Additionally shown are the best fit simulated performance (transmission and absorption) for a stack consisting of AR coated silicon on either side of a 75um powder mix layer. The target transmission band for the AR coating is 70-170 GHz and is marked with the blue band on the plot. Bottom Left: The IR blocking performance of a full composite filter is shown, with a 300K blackbody overlaid. Right: A drawing of the integrated test cryostat, wherein the filter (held at 20K) is used to block power from a 300K blackbody falling on a 5K disk bolometer (black). A total blocking efficiency of >98% was demonstrated using this setup, in keeping with the prediction from the FTS measurements. This was determined by measuring the heating of the bolometer when exposed to an aperture open to 300K, and determining the incident power relative to the same environment without a blocking filter.

Chapter 6

Real-Space Simulations of CMB Cluster Lensing

An essential companion to more advanced hardware for future CMB missions is more sophisticated simulation of expected CMB sky maps. Better simulation enables a more thorough understanding of the physical effects being observed and provides the tools for improved predictions of the performance of future experiments. For studying galaxy clusters (the most massive gravitationally bound objects in the universe) with the CMB, it is helpful to have detailed simulations that allow for rapid modification of the underlying assumptions. This is done by using general N-body simulations to generate the catalog of objects, the results from cluster modeling to generate the mass distribution of the objects, and folding these effects together with the CMB in a flexible framework. The resulting simulation approach is well suited for studying the systematics of SZ and lensing measurements with the CMB.

In this chapter, I will discuss work done to improve real-space simulations of the CMB for studying cluster lensing and the Sunyaev-Zel'dovich effect. I will focus heavily on the development of the lensing calculation framework and its implementation as part of the larger simulation package.

Generating these simulations in real-space (as opposed to Fourier space) allows for quickly propagating forward the effects of different models for the behavior of interactions between the CMB and large scale structure (such as the specific models for the Sunyaev-Zel'dovich effect and weak lensing). It also preserves the spacial correlations between separate effects due to galaxy clusters, such as those between the CMB lensing deflections and the Sunyaev-Zel'dovich effect.

6.1 Simulation Framework Overview

A full real-space simulation of the CMB involves several important components. In addition to a realization of the statistically generated base CMB, there are effects resulting from the intervening matter distribution, most notably galaxy clusters. Galaxy clusters contribute to the CMB via the Sunyaev-Zel'dovich effect (both thermal and kinetic components) and weak lensing, so a complete CMB simulation needs to account for these effects.

The bulk of the simulation framework discussed in this chapter was developed by Tomasz Biesiadzinski; my main contributions is the calculation of weak lensing deflections, the implementation of these deflections in generating the CMB maps, and the integration of this capability into the existing simulation framework. For a more thorough discussion of the framework itself and the non-lensing components, please consult Biesiadzinki's thesis [82].

6.2 The CMB

The base CMB is generated by taking a power spectrum created by the Code for Anisotropies in the Microwave Background (CAMB) software tool [83] [1] and assuming that the CMB is built of Gaussian fluctuations that produce this power spectrum. A sky realization is generated from the unlensed (CMB only) power spectra of the temperature anisotropies C_{TT}, the temperature and E-mode polarization correlations C_{TE}, and the E- and B-mode polarization anisotropies C_{EE}, and C_{BB}. This simulated CMB sky is generated in the flat-sky approximation (using Fourier modes as a small-angle approximation to spherical harmonics) in patches overlapping the desired N-body simulation region by generating random fields for the temperature fluctuations and B-mode polarization, with the E-mode polarization generated as a combination of the temperature field and an independent random field in order to produce the correct correlated spectrum. The resulting E- and B-mode maps are then rotated into Stokes Q and U maps and all the maps are Fourier transformed into real-space. A base CMB map is shown in Figure 6.1.

[1] camb.info, or via the NASA GSFC interface at https://lambda.gsfc.nasa.gov/toolbox/tb_camb_form.cfm

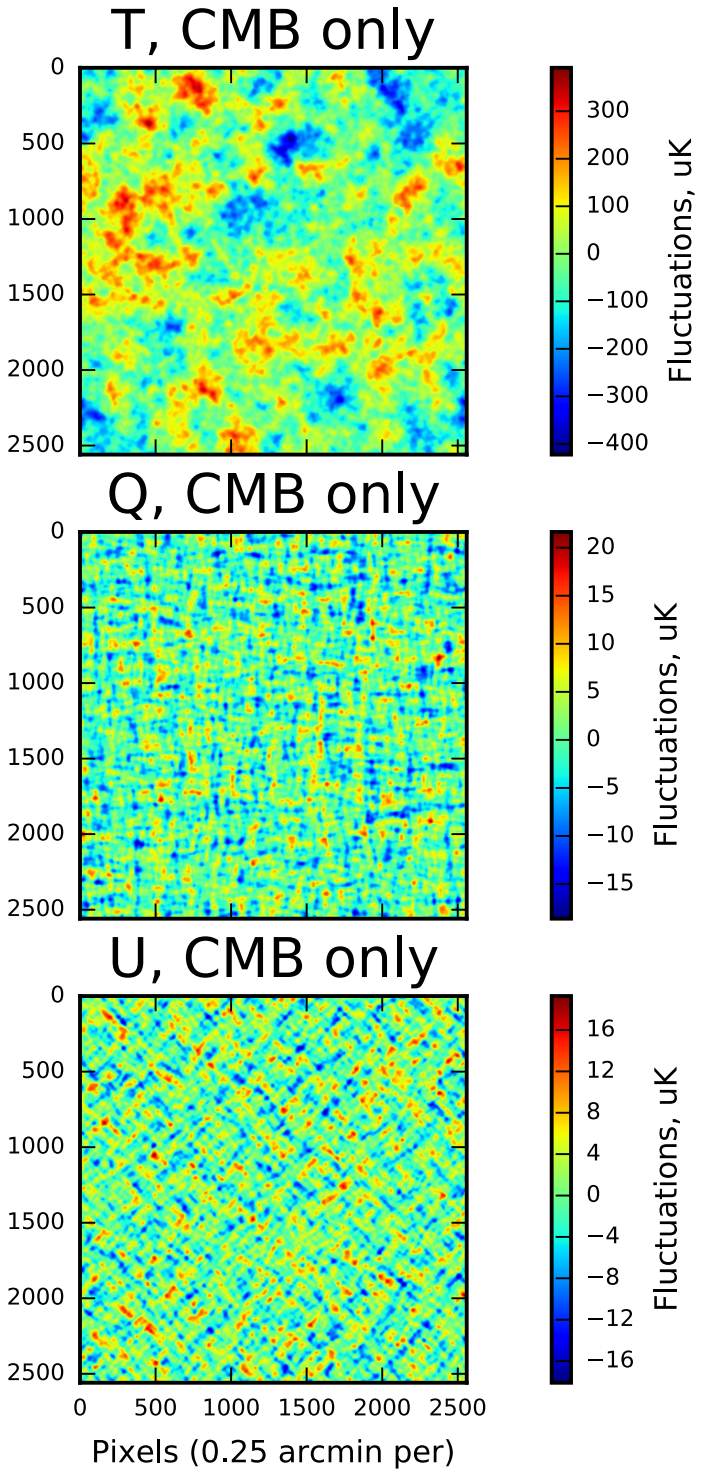

Figure 6.1: A patch of the simulated CMB, $(10.4°)^2$ generated from a CAMB spectrum for a standard ΛCDM universe, with no cluster contributions included. The temperature, Stokes Q, and Stokes U parameters are all simulated as a realization of Gaussian random fields that give the desired TT, TE, EE, and BB power spectra.

6.3 The Sunyaev Zel'dovich Effect

The Sunyaev-Zel'dovich (SZ) effect is a distortion of the CMB due to the hot electrons present in the intracluster medium (ICM) in galaxy clusters. The SZ effect is caused by inverse-Compton scattering of CMB photons off these hot electrons, leaving "cold spots" in the CMB (where there is a lack of photons due to them being shifted to higher frequencies) at primary observing bands at positions of galaxy clusters. The thermal SZ (tSZ) effect is due to the temperature of the electrons and the kinetic SZ (kSZ) effect is due to the bulk motion of the cluster (and its associated hot electrons) relative to the CMB [84] [85] [14]. These effects can be seen in the CMB as a decrement at primary observing bands and an increase at higher frequencies, and the clusters appear in surveys at other wavelengths (both as clustering of galaxies in optical surveys and as hot ICM emission in X-ray surveys), offering confirmation and further measurement from overlapping surveys in these spectral regions.

At CMB observing bands (218 GHz) the thermal SZ effect produces a decrement in the CMB by upscattering photons to higher frequencies, leaving "cold spots" in the CMB. The kinetic SZ effect has much less spectral dependence [14], and can either increase or decrease the total decrement caused by the thermal SZ effect (the overall effect remains a decrement since the kinetic SZ effect is much smaller in magnitude than the thermal). See Figure 6.2 for the spectral dependence of the thermal and kinetic components of the SZ effect, and Figure 6.3 for the simulated SZ components and their impact on the complete CMB.

6.3.1 Thermal Sunyaev-Zel'dovich Effect

The thermal SZ effect is modeled, in this simulation framework, by assuming the mass and redshift-removed scaled galaxy cluster pressure profile follows a generalized Navarro-Frenk-White (generalized NFW, or GNFW) profile [86] [87]. This generalized profile is used to generate the tSZ profile for each N-body cluster by scaling to the simulated halo mass, redshift, and angular diameter distance [82]. The tSZ signal is then aggregated for all the simulated halos in a given map region, and the resulting signal is added into the temperature map. The thermal SZ effect is unpolarized to a level far below current and next-generation instrument sensitivities, so its contribution is only accounted for in the temperature map.

6.3.2 Kinetic Sunyaev-Zel'dovich Effect

The kinetic SZ effect, resulting from the peculiar motion of galaxy clusters with respect to the primary CMB, is simulated by taking the peculiar velocity resulting from the N-body simulation, and combining it with a density profile derived from an NFW profile and varying depending on the cluster morphology (for example, cool core, non-cool core,and morphologically disturbed clusters all have slightly different profiles) of the cluster. For further details on these calculations, see chapter 2 of [82]. The resulting temperature perturbations are aggregated for all of the N-body clusters, and added to the combined temperature map. The polarization of the kSZ is also small compared to current sensitivity levels (and highly dependent on the detailed structure of the cluster [88], which is not being taken into account for these large-scale simulations), so it is also only accounted for in the temperature signal.

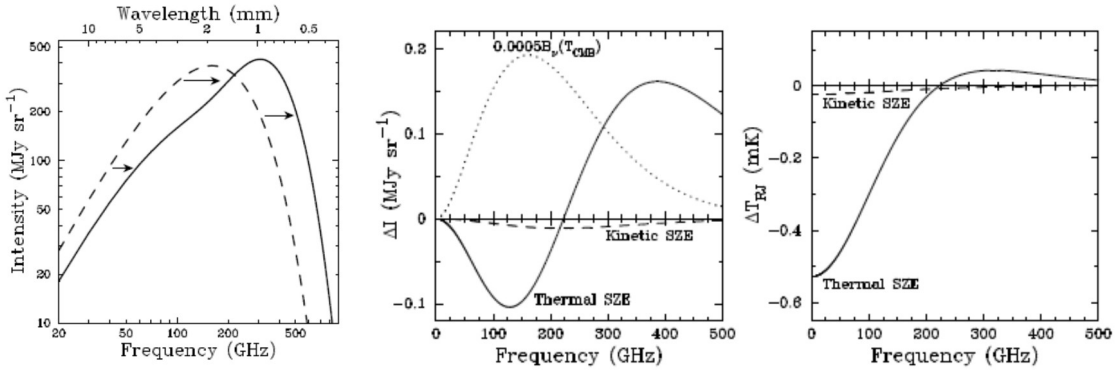

Figure 6.2: The spectral dependence and impact of the SZ effect. Left, The undistorted CMB (dashed) distorted by the SZ effect for a fictional large (1000 times the mass of a typical large cluster) galaxy cluster. This causes a decrease in intensity below 218 GHz and an increase above. Center, the spectral distortion (in intensity) caused be the thermal SZ (solid line), and kinetic SZ (dashed line), with a scaled CMB spectrum for comparison (dotted line). Right, the spectral distortion in the induced CMB temperature change. Figure from [14].

6.4 Lensing

The other significant contribution introduced to the CMB by galaxy clusters is CMB distortion due to gravitational lensing. Gravitational lensing is a necessary consequence of general relativity, by which the presence of a massive object

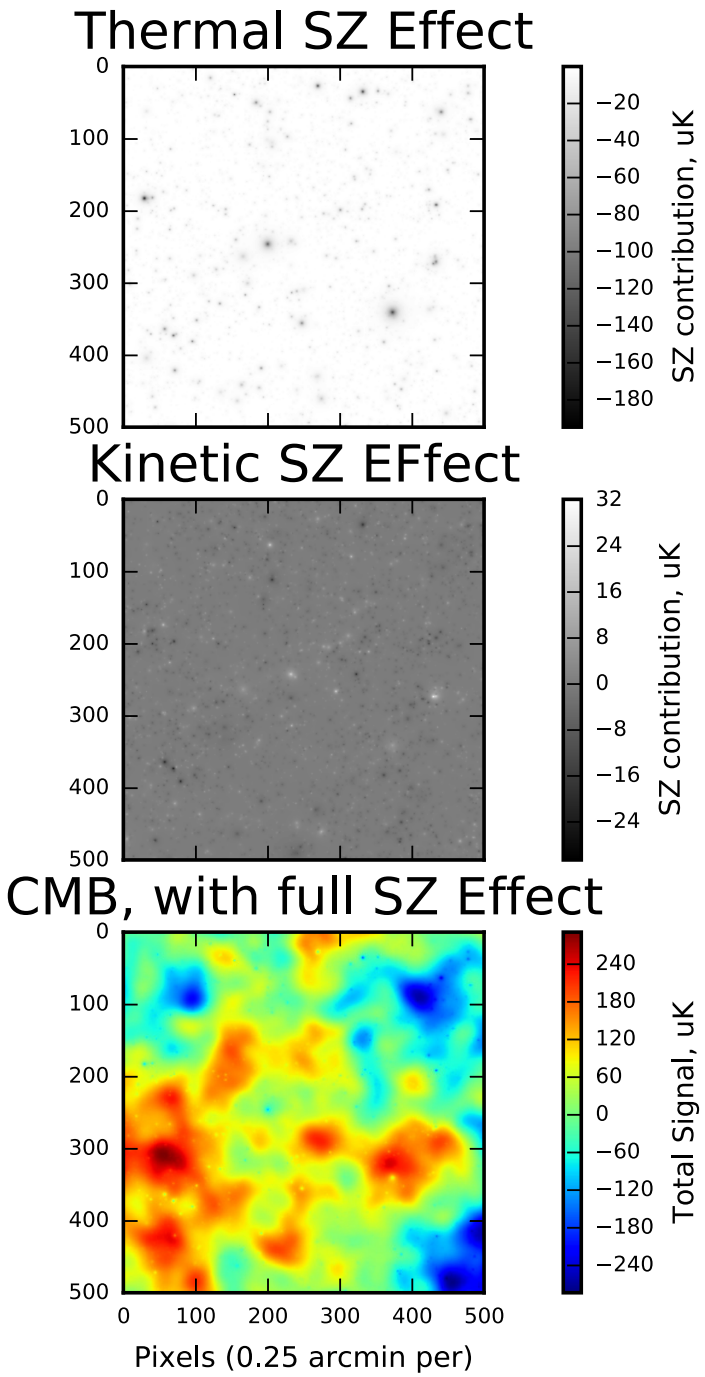

Figure 6.3: A full $(10.4°)^2$ simulation patch of (top) the thermal SZ Effect, (center) the kinetic SZ Effect, and (bottom) CMB Temperature with both SZ effects added in. Note that for this map (at 150 GHz), the Thermal SZ is present solely as a decrement to the CMB, while the kinetic SZ is either an increment or decrement depending on the cluster line-of-sight velocity.

distorts the space around it [89]. This distortion manifests as a shifting of the line-of-sight to a given point in space (or on the CMB), changing its perceived location and the observed shape of an object present there.

Lensing of the CMB introduces distortions to both the temperature and polarization components, contaminating primordial signals of interest, and providing an additional physical signal to observe.

The CMB offers a compelling environment for lensing measurements due to its unique properties as a background source. The CMB extends across the entire sky, and we have a good physical understanding of its characteristics. As the oldest visible light, it allows for probing the lensing signal from higher redshifts ($z \sim 2$) than can be reached via galaxy lensing, and with fluctuations that are well-approximated as a gaussian random field, lensing deflections can be detected as departures from the expected statistical behavior. Additionally, since the CMB is polarized, and lensing distortions appear in the polarization as well as temperature, it yields three lensed observables (temperature and two components characterizing the linear polarization) rather than just a single measurement [90].

These characteristics mean that the study of CMB lensing is important for both those interested in characteristics of the primary CMB and those interested in using it as a source for studying clusters via gravitational lensing. For the primary CMB, careful characterization of lensing is important so that its contribution can be estimated and removed (of particular importance in the search for primordial B-modes (curl-like modes in the polarization pattern on the sky), which are subject to contamination with power shifted from E-modes (divergence-like patterns) via lensing. For cluster science, CMB lensing offers another probe of the mass distribution of clusters, and can be combined with the SZ effect to further calibrate cluster characteristics.

In the simulation pipeline discussed here, I implemented real-space cluster lensing calculations and integrated it with the simulation framework created by Tomasz Biesiadzinski [82] to allow for creation of maps with realistic lensing and SZ contributions that are spacially correlated (as would be physically expected, and as opposed to previous simulations where the lensing contribution is computed statistically as a perturbation to the CMB power spectrum prior to generating a sky realization).

6.4.1 Calculating Lensing Deflections

The lensing deflections for a given object are computed by taking the mass and redshift, using those to generate the concentration factor using the c-M relation from the Canadian Cluster Comparison Project [91].

$$c = 7.85 \left(\frac{M_{vir}^{NFW}}{2x10^{12}} \right)^{-0.081} (1+z)^{-0.71} \tag{6.1}$$

Following this, the lens-plane dimensionless impact parameter of the line-of-sight with respect to the cluster (x) is computed for each pixel, given the cluster angular size (obtained from its angular diameter distance and radial size obtained from the cluster catalog), and the dimensionless deflection angle, $\alpha(\mathrm{x})$, is calculated for each pixel using the analytic form for NFW deflection angles given in [92].

$$\alpha(\mathrm{x}) = \frac{4\kappa_s}{\mathrm{x}} \left(\ln\frac{\mathrm{x}}{2} + \frac{2}{\sqrt{1-\mathrm{x}^2}} \mathrm{arctanh}\sqrt{\frac{1-\mathrm{x}}{1+\mathrm{x}}} \right) \tag{6.2}$$

Where x is the dimensionless impact parameter ($\mathbf{x} = \mathbf{r}/r_s$) and κ_s is the cluster's characteristic convergence.

$$\kappa_s = \frac{r_s \rho_s}{\Sigma_{crit}} \tag{6.3}$$

With r_s being the cluster scale radius, ρ_s the characteristic density, and Σ_{crit} the critical surface mass density of the cluster.

From here, the dimensionless deflection angle for each pixel is rescaled to a physical angle, then to the deflection in number of pixels. It is then multiplied by the unit vector pointing away from the cluster center to convert it into orthogonal sky components in pixel space (i.e. the "x" and "y" deflections in the same pixelization and coordinate space as the final maps). The deflection vectors (showing the remapping of the CMB) for several different cluster masses are plotted in Figure 6.4.

The total lensing deflection for a map is calculated via a multi-step process built on this core procedure:

(a) To begin with, the low mass objects are separated into a number of mass and redshift bins. Central values for these bins are then used to calcu-

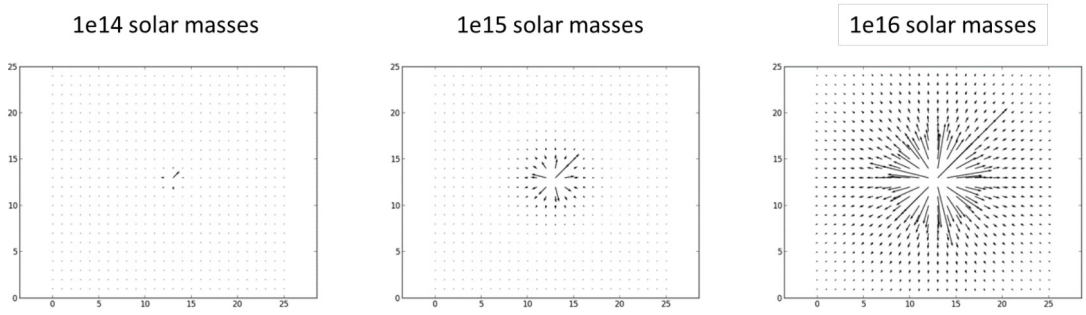

Figure 6.4: Plots of the deflection vectors for several different cluster masses. These plots are arbitrarily scaled and sampled, but demonstrate several lensing characteristics, including the symmetry of the lensing around the center of a symmetric cluster and the scaling of the lensing deflection signal with mass. These deflection vectors are aggregated for all of the lensing objects, then used to distort the CMB maps.

late a typical deflection kernel for the bin (these deflection kernels are carried around separated into orthogonal components, for ease of future use). These kernels are computed with a fixed size for ease of storage. The binned lensing deflection signals are then stored in an array for later use.

(b) The low mass lensing deflections are then aggregated by convolving the binned lensing patches with the lens positions for each object (by breaking up the lenses by bin, followed by convolving each bin's lensing kernel with the positions for all objects in that bin, then summing the contributions over all bins, yielding the combined lensing signal in each coordinate).

(c) The high mass objects are computed individually, using the full map size and generating a deflection contribution for each pixel, summing the signal over all high-mass objects.

(d) The low and high mass lensing deflection maps are added together (producing one complete lensing deflection map for each spacial coordinate, "x" and "y"). These maps are then used to remap the CMB (discussed in the next section). A total deflection magnitude squared (sum of the squares of the "x" and "y" lensing components) is shown in Figure 6.5.

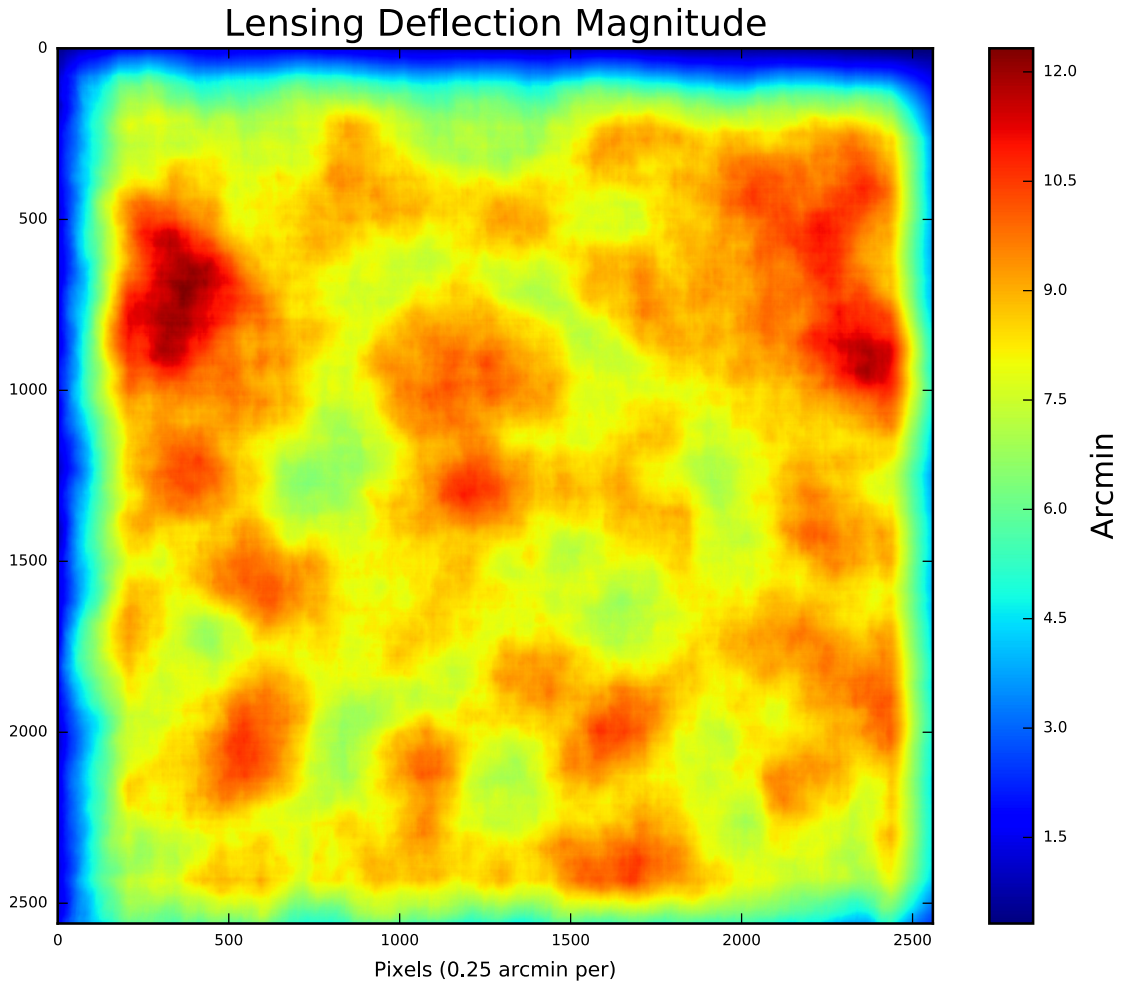

Figure 6.5: A full $(10.4^\circ)^2$ patch of the magnitude of the lensing deflections. The higher deflection regions correspond with a higher density of underlying matter (more cluster halos) in the many-body catalog used to populate this simulation. The edges of the patch have less lensing deflection due to the lack of lensing contributions from outside the region. This can be remedied by either apodizing the edges of the patch for analysis or cutting them off entirely.

6.4.2 Applying Lensing Deflections

Once the aggregate lensing deflections have been generated for the entire catalog of objects, the base CMB needs to be distorted by them. This is done using the open source computer vision library, OpenCV [2] [93]. The lensing deflections are aggregated as pixel-space shifts, and are applied using the OpenCV remapping function "remap" which efficiently transforms a source image using a specified mapping (in this case, the mapping is defined such that the destination location for a given pixel is given as the source location plus the lensing deflection) [94].

$$\tilde{T}(\mathbf{x}) = T(\mathbf{x} + \alpha(\mathbf{x})) \tag{6.4}$$

The resulting transformed map is then interpolated back to the correct pixelization to give an output map that is consistent with the desired patch. The application of this distortion to a CMB patch is shown in Figure 6.6.

[2] opencv.org

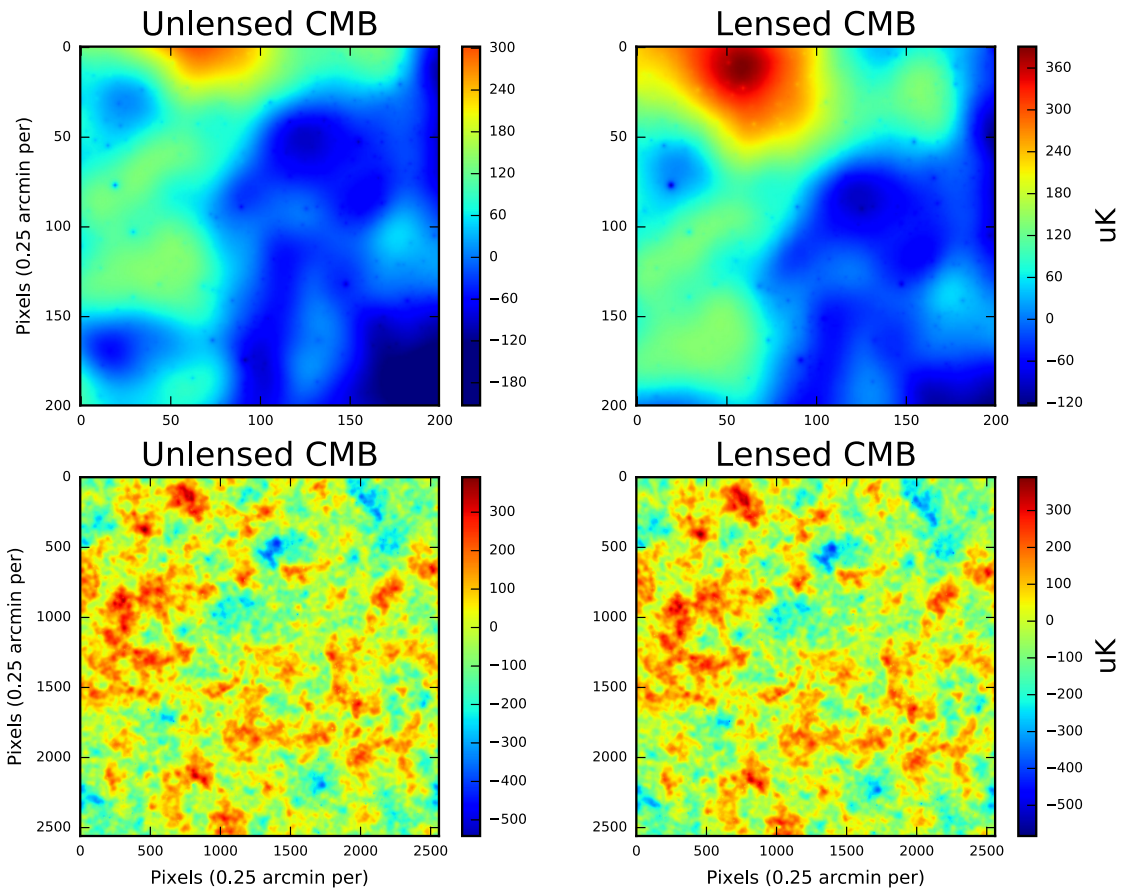

Figure 6.6: A small patch (top plots) and full $(10.4°)^2$ patch (bottom plots) before (left) and after (right) application of the lensing deflections. In the small patches, it is apparent that the pattern of the underlying CMB has been shifted by the lensing deflections, while the SZ signal (which is not lensed in these simulations), remains unshifted. The large patches show that, on the degree scale, the shifts due to lensing are subtle.

6.4.3 Checking Lensing Calculations

During the creation of the lensing simulation framework, there were several checks for consistency and correct behavior. A set of lensing deflections were made with large single cluster, centered in the field. Behind this cluster, different backgrounds were placed, including a flat field (consisting of a constant temperature across the entire region), a point source both close to and far from the cluster center, and a region of simulated CMB temperature field with a shallow gradient behind the cluster. The flat source correctly produced a flat resultant field, as expected from remapping the lines of sight (any sight line originally on a given temperature would be remapped to the same temperature, since the entire background is flat). Point sources in the background moved and were magnified, possibly being stretched into (sometimes multiple) long arcs if close enough to the lens center. Lenses in front of a gradient section of the CMB gave rise to quadrupolar shapes aligned with the gradient direction, matching the general behavior demonstrated in Lewis and Challinor [15]. Figure 6.7 shows the qualitative similarity of this effect.

After appropriate spacial behavior of the lensing simulations was confirmed, the statistical behavior of full simulation patches was checked by taking the power spectra of the simulated skies and comparing to the theoretical lensed power spectra obtained from CAMB.

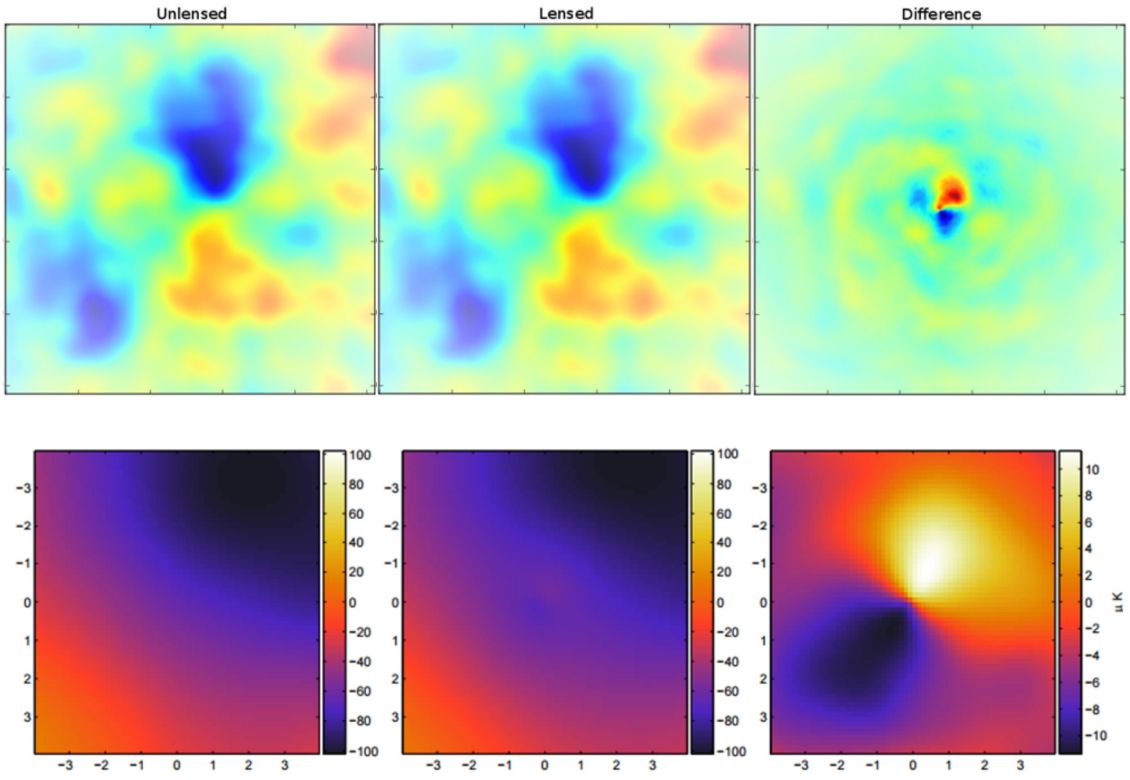

Figure 6.7: A simulated CMB (top row, with red indicating higher CMB temperature and blue indicating lower) and figure from Lewis and Challinor [15] (bottom row) demonstrating the quadrupolar shape induced by lensing a CMB gradient. The left panel of each row is the unlensed background, the center is the lensed signal, and the right panel is the difference between the two, showing this gradient-aligned shape. The more complicated structure visible in the top panel lensing difference is the result of lensing of the more complicated underlying CMB structure.

6.4.4 Tuning Lensing Simulation Parameters

Because of the binned approach to simulating the lensing contributions of low-mass objects, some tuning of the simulation parameters was needed. Lensing simulations were run with different numbers of mass and redshift bins to see the effect on the overall power spectra, and the final simulation parameters were chosen to best reproduce the theoretical power spectra obtained from CAMB. Figure 6.8 shows the power spectra resulting from a range of mass and redshift bin numbers, illustrating the dependence on these parameters.

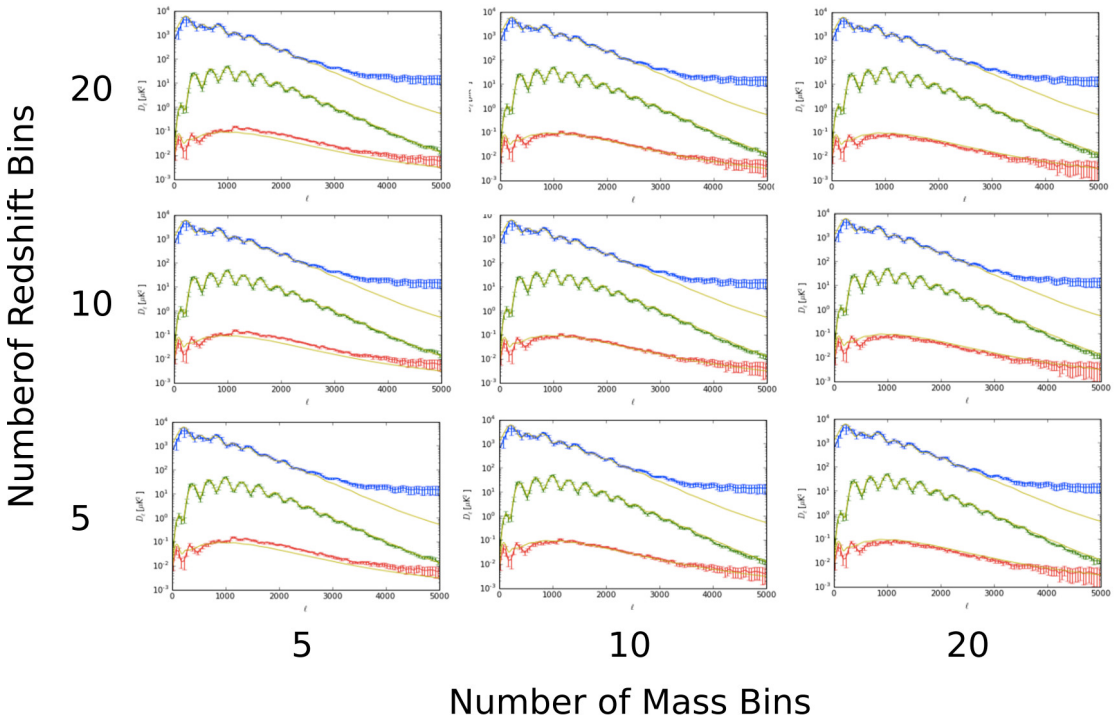

Figure 6.8: The power spectra resulting from varying the number of mass and redshift bins in the low-mass portion of the lensing simulation. The TT (blue), EE (green), and BB (red) estimated power spectra are shown, with the theoretical spectra underneath (plotted in gold). From these plots, it is apparent that increasing the number of mass bins improves the reproduction of the theoretical power spectra. The impact of increasing the number of redshift bins is significantly smaller. From these tests, it was determined that 20 mass and 20 redshift bins was a suitable baseline for future simulations. These parameters can, of course, be tuned for any given simulation to give the right balance of power spectrum reproduction and simulation performance (since fewer bins reduces the time needed to run the simulation).

The other important lensing parameter to be tuned was the size of the precomputed lensing kernels for the low-mass objects. Several different stamp sizes

were run, and the power spectra compared to theory. Figure 6.9 shows the power spectra resulting from different precomputed lensing kernel sizes.

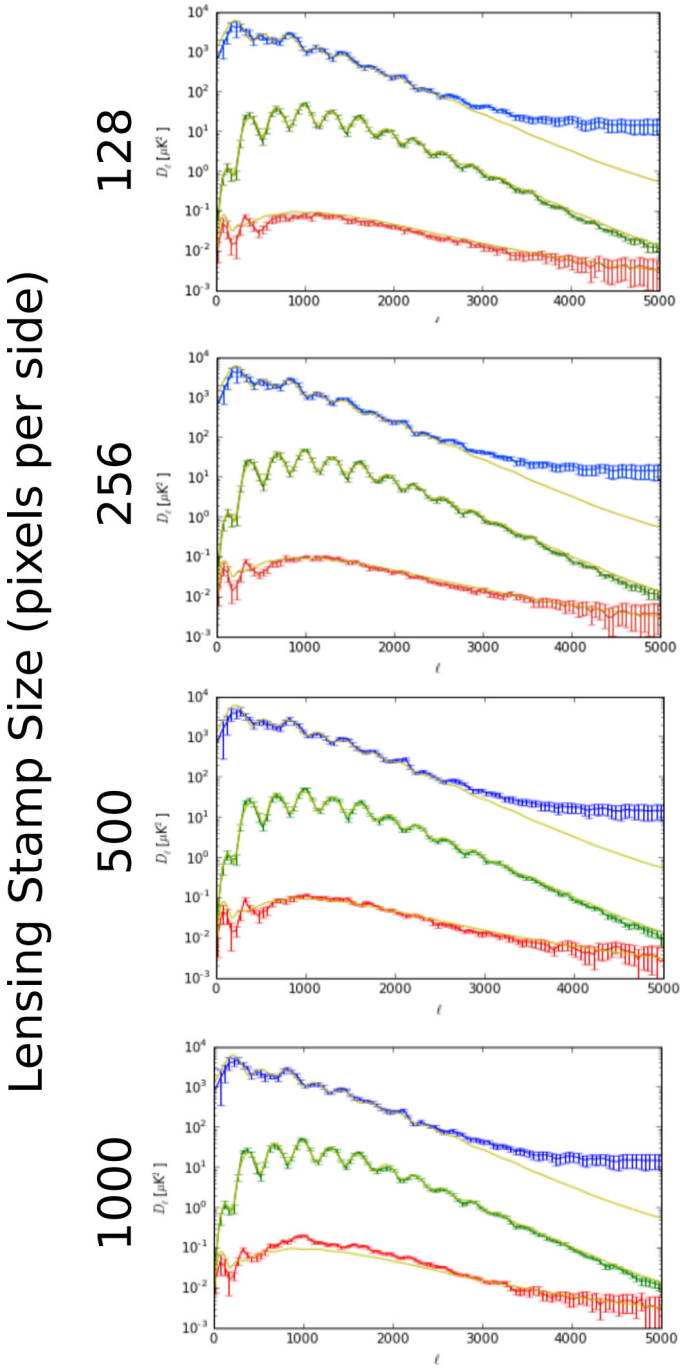

Figure 6.9: The estimated power spectra from simulations produced with a range of precomputed lensing stamp size. Smaller stamps take less time to compute, but provide a worse reproduction of the theoretical power spectra at low ℓ (large angular scales). Larger stamps better reproduce the large angular scales, but suffer from a larger degree of unbalanced lensing at the simulation edges, an effect causing noticeable deviation from the theoretical spectra for the 1000-pixel stamp. A stamp size around 256 was chosen as a baseline for future simulations.

6.5 Point Sources

Point sources were generated as randomly distributed samples from several distinct populations [95]. Power spectral distributions were generated for radio point sources [96], protospheroidal infrared (IR) sources [97], and late-type IR sources [98], and then a number of sources for a given flux density were drawn from a poisson distribution. These sources were then placed randomly on the CMB map. The polarizations were generated by producing a random polarization fraction and polarization angle, corresponding to a mean 3.8% polarization with a standard deviation of 3.4% and uniformly distributed polarization angle. These values were determined from analysis of point source data from the ACTPol project done by Rahul Datta [99]. The temperature and polarization contributions from point sources were then summed over all the point sources generated across all flux density bins, and added to their respective maps. See Figure 6.10 for a section of a temperature map with and without the addition of point sources.

For a detailed discussion of the implementation of the point source calculations, excluding their polarization see [82].

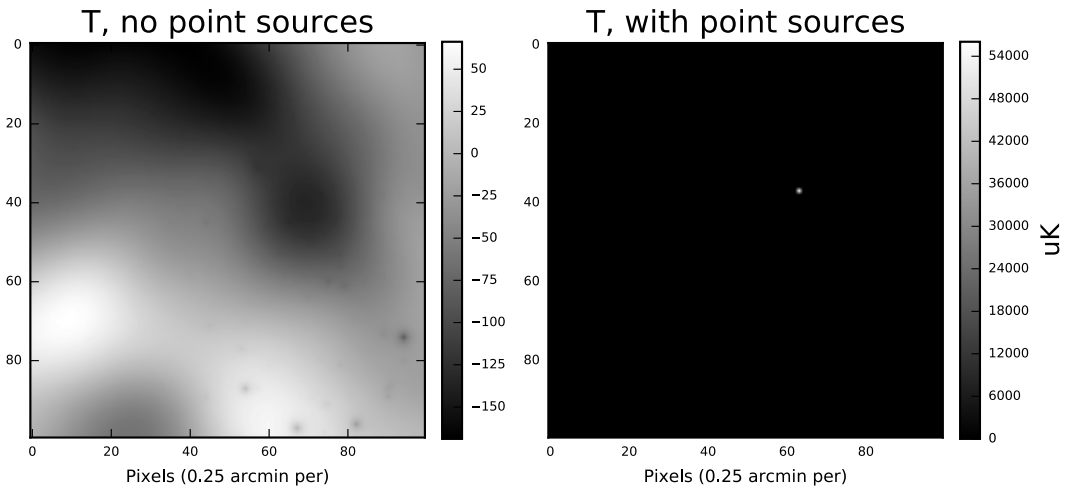

Figure 6.10: A small patch of the simulated CMB, with (right) and without the addition of point sources. This small patch was selected to show the high amplitude and small spacial extent of point source contributions (the point source shown is a single pixel in extent, but very high temperature).

6.6 Instrumental Effects

After creating realistic maps containing the relevant galaxy cluster physics as well as the CMB, it was important to account for realistic instrumental effects. This ensures that simulations can be generated that accurately represent the capabilities of existing or future instruments, and increased the usefulness of the simulation pipeline. In order to accurately capture the relevant instrumental effects, both telescope beams and instrument noise were included in the complete simulation. For the complete description of the implementation of these see [82].

6.6.1 Beam Convolution

The first step after simulating complete sky maps was convolution with the instrument beam to reproduce the angular resolution of the telescope. The simulations shown here were convolved with a 1 arcmin full width half max Gaussian beam, in keeping with the expected telescope beam for next-generation ground-based CMB telescopes. This framework can also convolve with the measured 2-dimensional instrument beams, allowing for accurate representation of current instruments (including asymmetries and imperfections in the telescope beam that would not be properly accounted for by the equivalent Gaussian beam). A sky section before and after convolution with a beam is shown in Figure 6.11.

6.6.2 Noise

Following convolution with the instrument beam, the simulations were dressed with instrumental noise appropriate for the telescope, instrument, and frequency band. This noise is generated as a realization of a noise power spectrum that is either taken from measurements of the actual performance of the instrument (in the case of existing instruments), or generated from a combination of the expected (thermal) detector noise and atmospheric noise for the specific instrument of interest. The simulation maps presented here were generated with SPT-like noise and a noise level of 1μK-arcmin in temperature (and therefore 1.4 μK-arcmin in polarization). Figure 6.12 shows a sky patch of the Q-Stokes parameter before and after adding in the instrumental noise component.

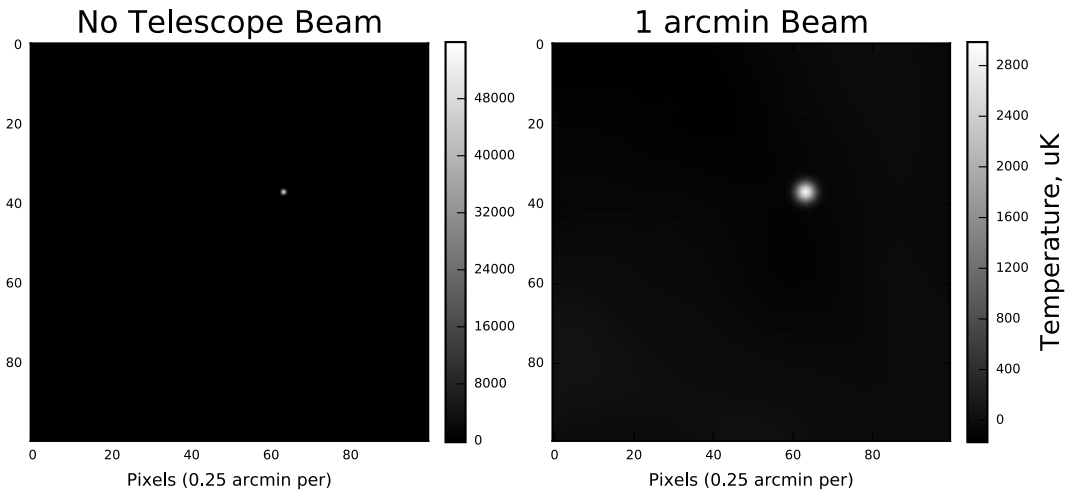

Figure 6.11: A small patch of the simulated CMB, with (right) and without (left) convolution with a 1 arcmin FWHM Gaussian beam. The simulation framework allows for convolution with either measured instrument beams or simulated beams. The blurring from the 1 arcmin beam spreads the point source in the image from a single pixel out to a 2D Gaussian.

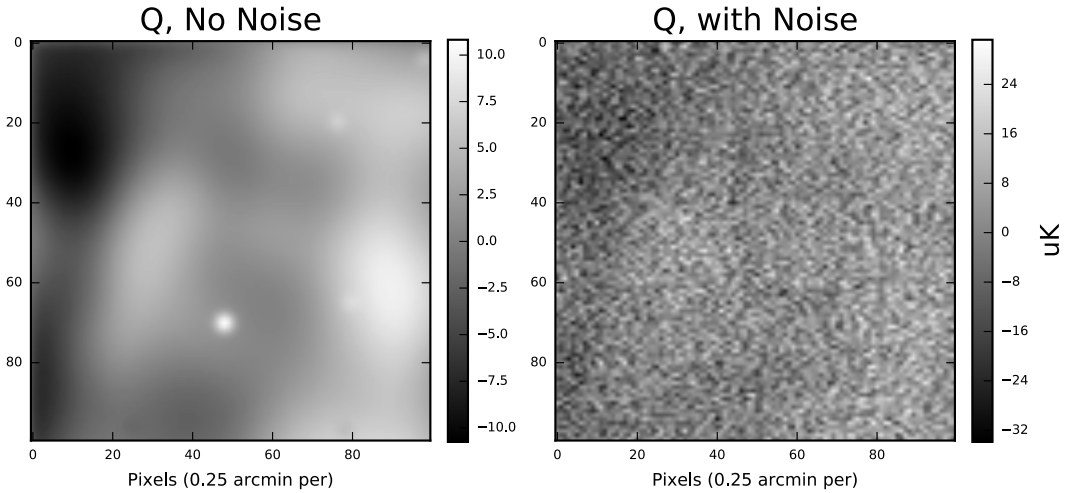

Figure 6.12: A small patch of the Stokes Q parameter from the simulated CMB, including SZ clusters, point sources, and beam convolution, with (right) and without (left) the addition of simulated noise. This noise model consists of 1/f noise added to a realistic instrument noise model.

6.7 Full Simulation Performance

By accounting for all significant cluster-derived sky components, the initial CMB, and realistic instrument performance, realistic maps of the CMB are generated (see Figure 6.13 for plots of these simulations and the resulting power spectra). These simulations accurately reproduce the expected statistical behavior of the sky (as shown by the power spectra for TT, EE, and BB cross correlations matching well the theoretically-predicted behavior), and therefore offer a viable simulation product with known characteristics and the ability to adjust the various components and explore their effects on the resulting analysis. These simulated maps will prove a useful tool for understanding the current generation of CMB measurements and for developing the next.

6.8 Future Directions

The next steps for this capability are several, both in improving this simulation pipeline, using it to improve complementary software tools, and using it to better understand existing and future CMB observations.

The ability to add and subtract sky components, while also knowing definitively the simulated lensing deflections offers a powerful tool for improving lensing deflection estimators and making them robust to contamination from other effects (such as point sources and the SZ effect). These types of simulations offer the ideal testbed for such work. These simulations also offer a testbed for the development of new lensing estimators, since the lensing signal is known and the simulations can be rapidly modified to test for estimator robustness to a wide assortment of factors.

Within the simulation framework itself, there are some improvements to be made, both in optimizing the performance and adding higher-order effects that were left out in the initial implementation.

To optimize the performance, some pieces of the software can be effectively parallelized to improve the computation speed. Additionally, more sophisticated models can be implemented for the lensing deflections and SZ effect, taking into account density profiles that are more complicated than the NFW, or even using fully numerical simulations of the density profile of cluster objects (allowing for much greater complexity in the lensing signal of a given object).

Lensing can also be implemented as a distortion to the signals being added for distant objects, namely the high-redshift point sources and high-redshift SZ clusters. These second-order contributions will introduce additional distortions to the CMB sky that could be studied in future simulations produced by this code.

Scientifically, it offers the opportunity to test the significance and sensitivity to effects like the correlation between lensing and SZ signals, and will offer guidance for the next generation of CMB telescopes looking to survey galaxy clusters in greater detail.

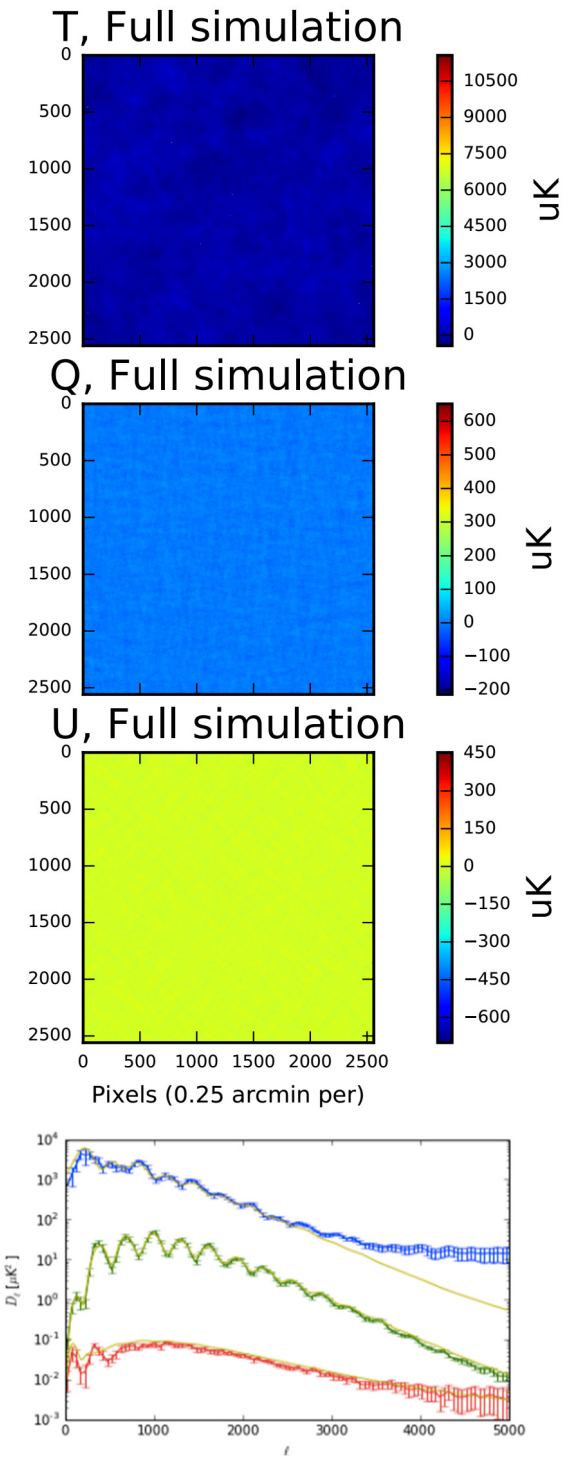

Figure 6.13: A full $(10.4^\circ)^2$ simulation patch, with lensing, the thermal and kinetic SZ effects, point sources, beam convolution, and instrument noise. The T (top map), Stokes Q (center map), and Stokes U (bottom map) are all shown, as is a reconstruction of the TT (blue data set), EE (green data set), and BB (red data set) power spectra from the map. These power spectra are compared to the theoretical input power spectra (gold lines), showing excellent reproduction of the desired statistical behavior.

Chapter 7

Concluding Remarks

Precision cosmology is a robust and growing field. We have finally entered the era where detailed measurements of the universe as a whole can yield information about its structure on the largest scales and the dynamics of its history.

The Cosmic Microwave Background offers a powerful tool for illuminating the nature of the universe in its infancy, as well as today. Developing the next generation of CMB observatories will take impressive technological feats and new innovations in order to push instrumental sensitivity to the point where it can measure the anisotropies (specifically polarization anisotropies) to the levels needed to further constrain cosmological parameters. It will certainly be among the most important observational tools for the next generation of cosmology (as it was for the last).

The technologies discussed in this thesis will enable improved sensitivity for the next generation of CMB telescopes. Silicon metamaterial optics promise to improve overall throughput of future experiments, and composite silicon optics (as demonstrated in the IR blocking filters) will create more compact and efficient telescope systems. Additionally, metamaterial silicon waveplates will enable improved large-angular-scale measurements by providing an avenue for efficient polarization modulation and enabling sophisticated noise reduction techniques. Even improved simulations will help improve the next generation of CMB experiments by providing better understanding of CMB skies and the biases present in their measurement (and therefore helping to unbias future measurements).

In the preceding chapters, I described a novel approach to making silicon lens surfaces anti-reflective, by machining sub-wavelength features into them. This

required designing and constructing a sophisticated fabrication facility, capable of making micron-scale precision features over surfaces hundreds of millimeters in diameter, and successfully produced a number of lenses for the ACTPol experiment. As an extension of the anti-reflection fabrication work, and in an effort to solve thermal problems with existing filters, I designed an infrared-blocking filter using an anti-reflection silicon substrate. This filter exhibited excellent IR blocking and cryogenic performance, while maintaining high transmission in the low-frequency signal bands, and can be scaled up to the size necessary for the current and future ACT cameras. These optical technologies offer great promise for the next generation of CMB experiments, and they will play an enabling role as larger and more sensitive observatories are built.

The final technology I developed was a simulation framework for generating a lensed CMB by using N-body simulation results. This allows for the detailed cluster physics to be handled independently from the large-scale structure simulation, and allows for rapid simulation of the effects of differing cluster physics on the CMB. In conjunction with an existing framework for similarly handling the Sunyaev-Zel'dovich effect, it enables a better understanding of cluster contributions to the CMB, and allows for the rapid simulation of these contributions over a wide range of cluster characteristics. These simulations can be used to characterize and remove measurement biases, and explore the detailed impact of cluster physics on measurements of the CMB.

Next generation experiments, enabled by current and future technological improvements, promise to provide better constraints on the sum of neutrino massses, improved constraints on inflation (and possibly measurements of inflationary gravitational waves), and will illuminate the nature of dark matter and dark energy by characterizing both the early universe and the composition of the later universe at its largest scales.

Appendix A

Metamaterial Fabrication System Details

This appendix contains the schematic diagrams for the custom dicing saw used to cut the machined antireflection surface treatments on silicon optics. These schematics give the overall system construction and serve as a reference for specific parts and connection information. The enclosure temperature control system, the flood cooling system, the compressed air system, and the control electronics are covered in this appendix, along with notes on the details of their construction. The temperature control system is laid out in Figure A.1, the flood cooling system in Figure A.2, the control electronics in Figure A.3, and the compressed air system in Figure A.4. It also includes a block diagram overview of the cutting code and a brief overview of the cutting procedure for a silicon optic.

A.1 Metamaterial Fabrication System Schematics

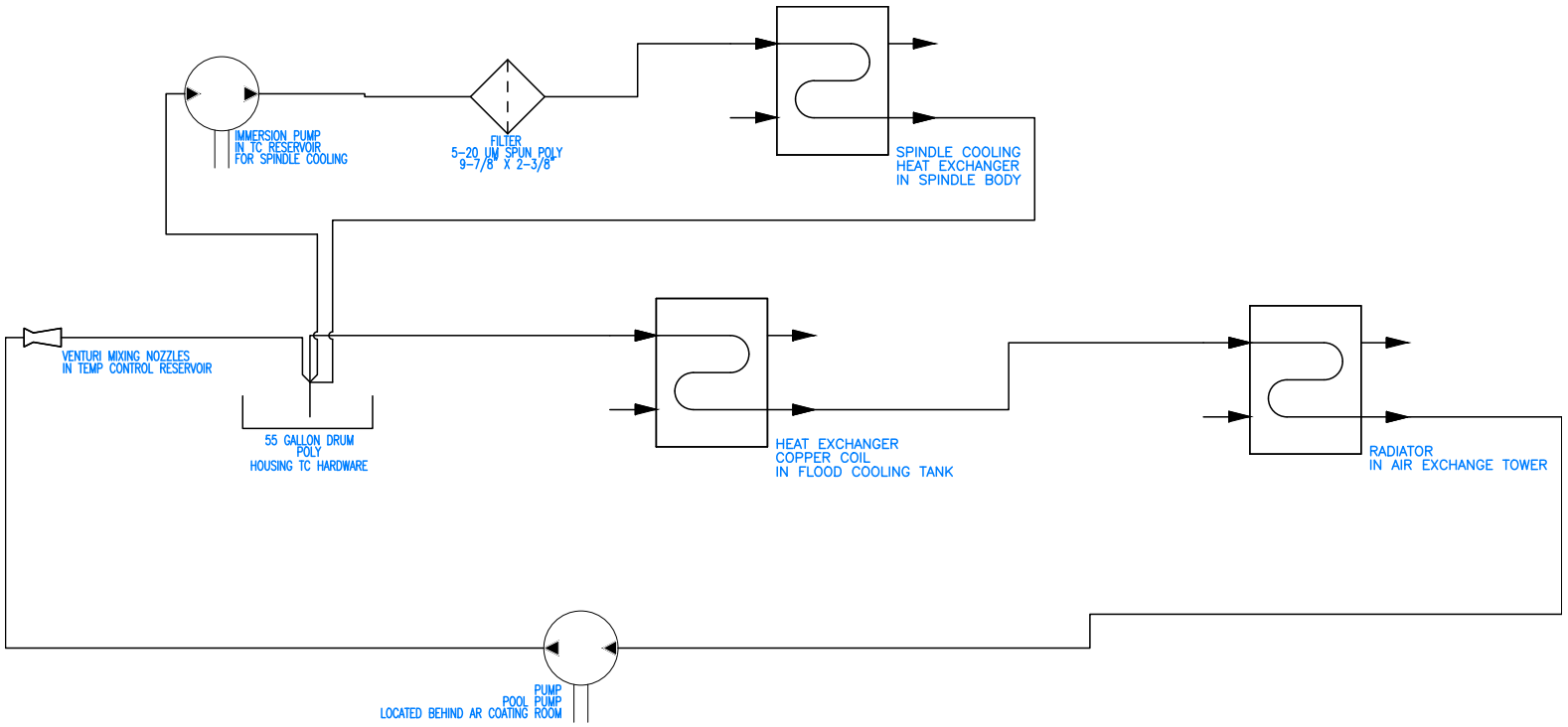

Figure A.1: A schematic of the metamaterial fabrication machine temperature control system. This system consists of two loops circulating water from a 55 gallon reservoir. The first loop uses an immersion pump to circulate water through a 5 micron particulate filter then through the cooling galleries in the body of the dicing spindle. The second loop uses a remotely mounted pump to draw the temperature control water through a heat exchanger coupled to the flood cooling bath and a radiator (with connected circulation fan) connected to the air in the machine enclosure. the pump then returns the water through a set of mixing nozzles to the reservoir. The reservoir has a heat exhanger coupled to the building process chilled water supply, 3kW of heating elements controlled by a PID controller, and an RTD thermometer providing the input to the PID controller.

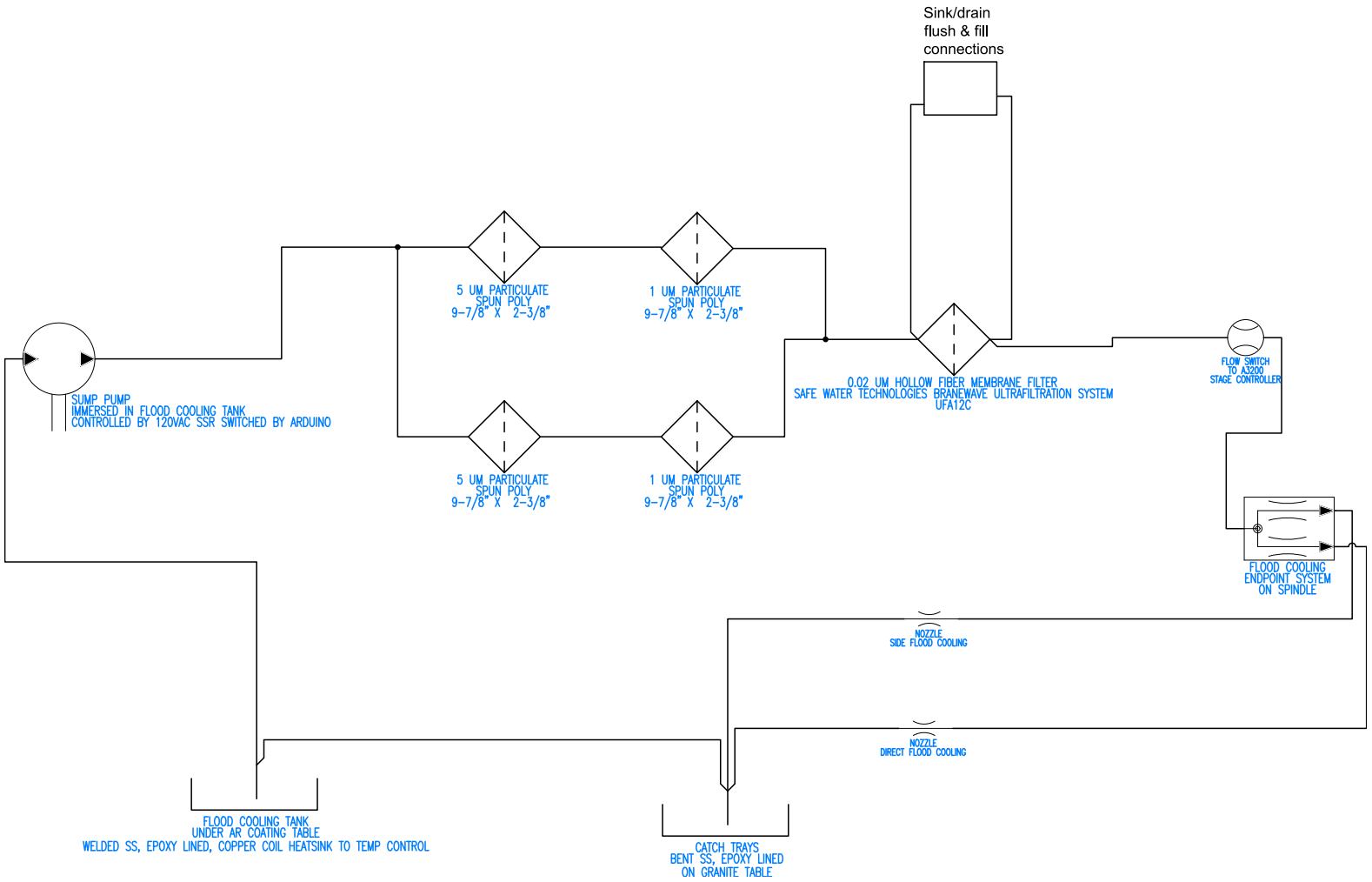

Figure A.2: A schematic of the metamaterial fabrication machine flood cooling system. This system consists of an immersion pump in an open tank below the AR coating gantry. This pumps the coolant (water and KerfAid surfactant mix) through a series of progressively finer filters (ending with a 0.02 micron hollow fiber membrane filter) and through a set of nozzles mounted on the spindle blade guard. This provides cooling and lubrication for the blade and substrate and removes debris generated by the cutting process. The water is collected by a set of catch trays and returned to the reservoir tank via gravity feed.

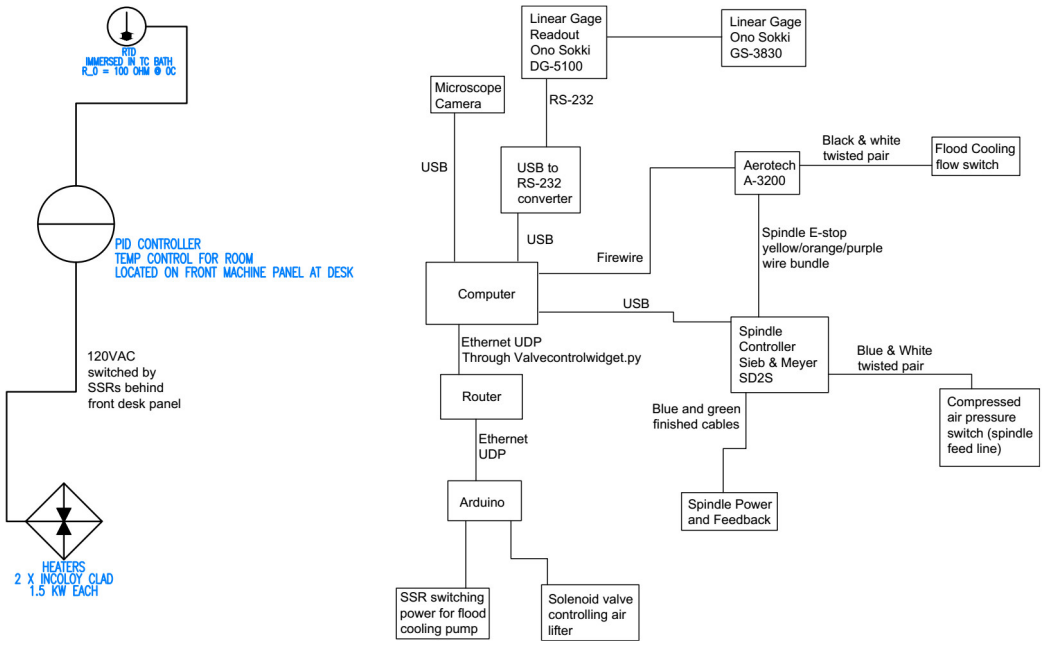

Figure A.3: A schematic of the control electronics for the AR coating system. A desktop computer running the Windows 7 operating system is used for the overall control, connecting via firewire to the Aerotech A3200 motion control unit. This unit handles the stage motion control and feedback, and communicates with the computer via Aerotech's proprietary software. The computer is also connected via USB to a Sieb & Meyer SD2S motor drive controller, which handles control of the dicing spindle. One of the SD2S outputs is connected to the A3200 system and configured to trigger the gantry emergency stop when the spindle suffers an unexpected shutdown. The spindle controller is also connected to a pressure switch in the compressed air system, which allows for automatic stopping of the spindle in the event of the compressed air pressure dropping below an acceptable value. The computer is connected via RS-232 (through an RS-232 to USB converter) to the readout electronics for the Ono Sokki linear gage, and through ethernet (UDP through a dedicated router) to an arduino handling the switching for the flood cooling pump and the solenoid valve controlling the air lifter that retracts the linear gage.

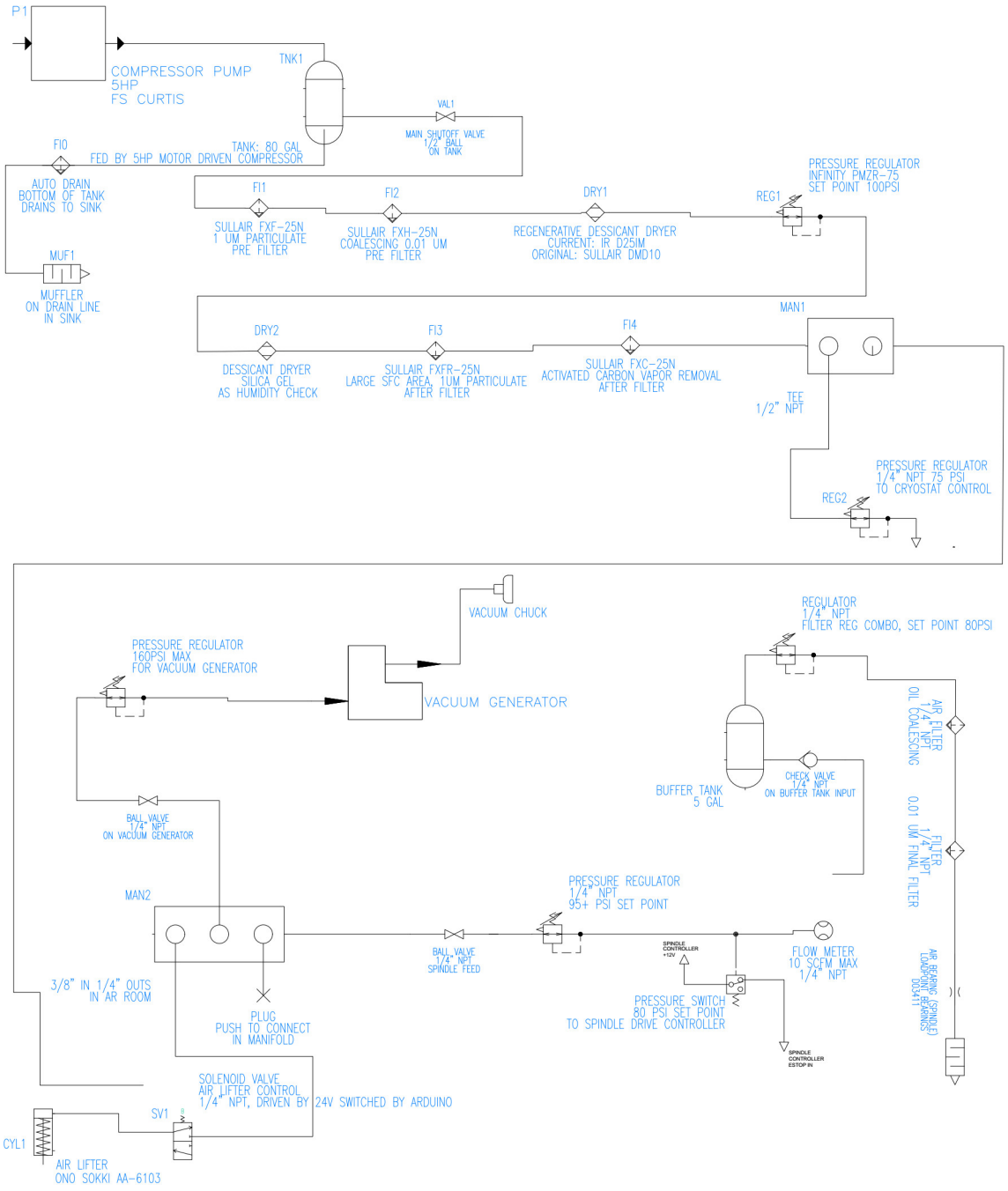

Figure A.4: A schematic of the compressed air system that feeds the AR machining system. A 5HP compressor feeding an 80 gallon tank provides the air supply, which is then filtered through a series of particulate and oil removal filters and a regenerative dessicant dryer. This air is then fed to the AR coating enclosure, where it is used to run the air lifter (through a solenoid valve), the vacuum chuck (through a manual shutoff valve), and the spindle (through a manual shutoff valve, flow meter and pressure switch, then a ballast tank and secondary filter set to prevent transfer of contaminants to the spindle).

A.2 Metamaterial Fabrication Procedure Overview

A simplified block diagram of the machining procedure follows in Figure A.5. It is followed by a description of a simplified version of the full machining procedure, as devised by Charles Munson (with input from others) and recorded by Curtis Weaverdyck.

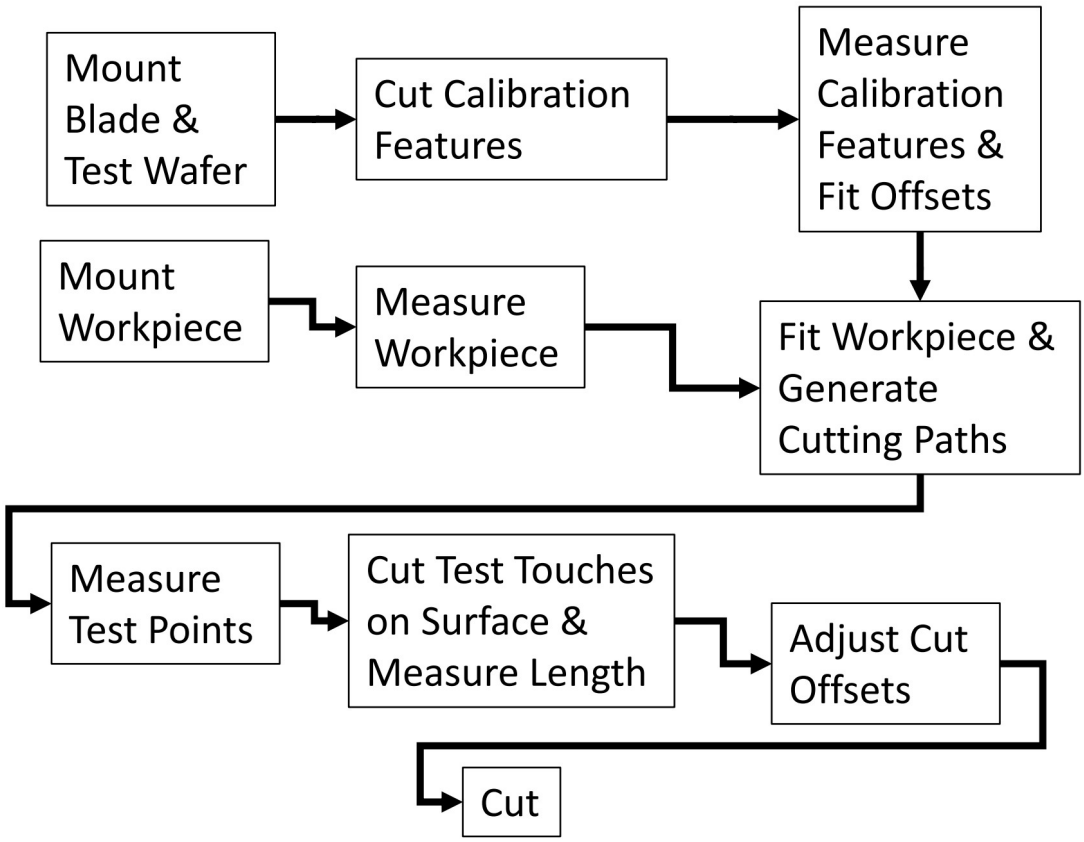

Figure A.5: A schematic of the general cutting procedure. The workpiece is mounted and measured, as is the blade. A set of test features are cut and measured, then fit to generate the cutting offsets needed to compute the tool paths. This information and the workpiece measurements are then used to locate the workpiece and generate the set of toolpaths. From this fitting, a set of test points are generated. These are measured to confirm proper fitting of the workpiece surface. A set of shallow test touches are made, cutting $\sim 10-15\mu$m into the surface, and measuring the resulting chord length. These test touches confirm proper blade alignment and allow for fine tuning of the cuts to generate the proper final depth. After this, the final cutting begins.

Operation Procedure for Dicing System

(a) Mount Lens

(b) Measure Lens

(c) Measure Lens Mounting Flange

(d) Measure Dressing Block

(e) Measure Test Wafer

(f) Calibration (occasional)

(g) Mount Blade

(h) Dress Blade

(i) Pre-cuts and Measure with Microscope

(j) Fit Lens Surface

(k) Comfirm measurement check points

(l) Measure location for test touch

(m) Make test touch

(n) Shift tool path files as needed

(o) Cut

(p) Post-cuts and Measure with Microscope

For Each Lens Side and Direction

(a) Measure the mounting flange, for a flat reference of the lens tilts

(b) Measure the dressing block, necessary to generate the dressing cuts

(c) Measure the test wafer, necessary for pre- and post-cuts

(d) Fit lens

(e) Measure test touch point on flange

(f) For uncut lens surfaces, measure the residuals using the fit check points

(g) Make cuts (all necessary cuts to make the structures in this direction, with pre- and post-cuts before and after each, and test touches on the flange to confirm relative depths

(h) Rotate lens

For Each Blade

(a) Mount Blade

(b) Dress Blade (fit dressing block, generate cuts, cut dressing block until cutting noise has diminished)

(c) Make pre-cuts (fit test wafer, generate cuts, make cuts)

(d) Observe pre-cuts with microscope, measure, save annotated image as record of shape

(e) Test touch on workpiece (measure point, predict position for 10 μm depth touch, make touch, measure chord length, adjust depth offset)

(f) Adjust depth offset for toolpath files

(g) Cut Workpiece (listen for cutting noise, photograph after $\sim$100 lines to make sure cuts look right and are aligned properly relative to previous cuts)

(h) Post cuts, measure and save

Calibration Procedure

(a) Cut YZ-plane calibration feature on test wafer

(b) Measure YZ-plane calibration feature

(c) Fit YZ-plane calibration feature to generate blade offsets

(d) Make X-axis calibration feature (set of shallow cuts)

(e) Measure X-axis calibration feature

(f) Plot X-axis calibration feature and extract center positions, use to generate blade offset

Bibliography

[1] G. Hinshaw et al. Nine-year wilkinson microwave anisotropy probe (wmap) observations: Cosmological parameter results. *The Astrophysical Journal Supplement*, 2013.

[2] J. C. Mather, D. J. Fixsen, R. A. Shafer, C. Mosier, and D. T. Wilkinson. Calibrator design for the cobe far-infrared absolute spectrophotometer. *The Astrophysical Journal*, 1999.

[3] Dorothea Samtleben, Suzanne Staggs, and Bruce Winstein. The cosmic microwave background for pedestrians: A review for particle and nuclear physicists. *Annual Review of Nuclear and Particle Science*, 2007.

[4] Wayne Hu and Scott Dodelson. Cosmic microwave background anisotropies. *Ann. Rev. Astron. Astrophys.*, 2002.

[5] Planck Collaboration. Planck 2015 results. x. diffuse component separation: Foreground maps. *Astronomy and Astrophysics*, 2016.

[6] R J Thornton et al. The atacama cosmology telescope: The polarization-sensitive actpol instrument. 2016.

[7] Matthew Hasselfield et al. The atacama cosmology telescope: Sunyaev-zel'dovich selected galaxy clusters at 148 ghz from three seasons of data. *Cosmology and Nongalactic Astrophysics*, 2013.

[8] Michael Niemack. Cmb measurements with the atacama cosmology telescope. IAU General Assembly, 2015.

[9] R. Datta, J. Austermann, J.A. Beall, D. Becker, K.P. Coughlin, S.M. Duff, P.A. Gallardo, E. Grace, M. Hasselfield, S.W. Henderson, G.C. Hilton, S.P. Ho, J. Hubmayr, B.J. Koopman, J.V. Lanen, D. Li, J. McMahon, C.D. Munson, F. Nati, M.D. Niemack, L. Page, C.G. Pappas, M. Salatino, B.L. Schmitt, A. Schillaci, S.M. Simon, S.T. Staggs, J.R. Stevens, E.M. Vavagiakis, J.T. Ward, and E.J. Wollack. Design and deployment of a multichroic polarimeter array on the atacama cosmology telescope. *Journal of Low Temperature Physics*, 2015.

[10] Sigurd Naess et al. The atacama cosmology telescope: Cmb polarization at $200 < \ell < 9000$. *Journal of Cosmology and Astroparticle Physics*, 2014.

[11] Wikipedia user Stahlkocher. https://en.wikipedia.org/wiki/monocrystalline_silicon#/media/file:monokristalines_silizium_f%c3%bcr_die_waferherstellung.jpg. Used under the creative commons license.

[12] Donald C. O'shea, Thomas J. Suleski, Alan D. Kathman, and Dennis W. Prather. *Diffractive Optics: Design, Fabrication, and Test.* SPIE Press, 2004.

[13] R. Datta, C. D. Munson, M. D. Niemack, J. J. McMahon, J. Britton, E. J. Wollack, J. Beall, M. J. Devlin, J. Fowler, P. Gallardo, J. Hubmayr, K. Irwin, L. Newburgh, J. P. Nibarger, L. Page, M. A. Quijada, B. L. Schmitt, S. T. Staggs, R. Thornton, and L. Zhang. Large-aperture wide-bandwidth antireflection-coated silicon lenses for millimeter wavelengths. *Appl. Opt.*, 52(36):8747–8758, Dec 2013.

[14] John E. Carlstrom, Gilbert P. Holder, and Erik D. Reese. Cosmology with the sunyaev-zel'dovich effect. *Ann. Rev. Astron. Astrophys.*, 2002.

[15] Antony Lewis and Anthony Challinor. Weak gravitational lensing of the cmb. *Astrophysics*, 2006.

[16] Wayne Horowitz. *Mesopotamian Cosmic Geography.* Eisenbrauns, 1998.

[17] American Institute of Physics Center for the History of Physics. The greek worldview: https://www.aip.org/history/exhibits/cosmology/ideas/greekworldview.htm.

[18] Stephen Hawking, editor. *On the Shoulders of Giants.* Running Press, 2002.

[19] American Institute of Physics Center for the History of Physics. The start of scientific cosmology: https://www.aip.org/history/exhibits/cosmology/ideas/start-of-scientific-cosmology.htm.

[20] Owen Gingerich. Did copernicus owe a debt to aristarchus? *Journal for the History of Astronomy*, 16(1):37–42, Feb 1985.

[21] David W. Corson, editor. *Man's Place in the Universe: Changing Concepts.* College of Liberal Arts, University of Arizona, 1977.

[22] American Institute of Physics Center for the History of Physics. The mechanical universe: https://www.aip.org/history/exhibits/cosmology/ideas/mechuniverse.htm.

[23] Charles Joseph Singer. *A Short History of Science to the Nineteenth Century.* Clarendon Press, 1941.

[24] William Herschel. *The Scientific Papers of Sir William Herschel.* The Royal Society and the Royal Astronomical Society, 1912.

[25] H. Shapley. On the nature and cause of cepheid variation. *Astrophysical Journal*, 1914.

[26] Henrietta S. Leavitt. 1777 variables in the magellanic clouds. *Annals of the Harvard College Observatory*, 1908.

[27] Edwin Hubble. A spiral nebula as a stellar system, messier 31. *Astrophysical Journal*, 1929.

[28] American Institute of Physics Center for the History of Physics. From our galaxy to island universes: https://www.aip.org/history/exhibits/cosmology/ideas/island.htm.

[29] Albert Einstein. Die feldgleichungen der gravitation. *Presussische Akademie der Wissenschaften*, 1915.

[30] American Institute of Physics Center for the History of Physics. The expanding universe: https://www.aip.org/history/exhibits/cosmology/ideas/expanding.htm.

[31] V. M. Slipher. Spectroscopic observations of nebulae. *Popular Astronomy*, 1915.

[32] Edwin Hubble. A relation between distance and radial velocity among extra-galactic nebulae. *Proceedings of the National Academy of Sciences of the United States of America*, 1929.

[33] Georges Lemaître. Un univers homogène de masse constante et de rayon croissant rendant compte de la vitesse radiale des nébuleuses extra-galactiques. *Annales de la Société Scientifique de Bruxelles*, 1927.

[34] Georges Lemaître. Republication of: A homogeneous universe of constant mass and increasing radius accounting for the radial velocity of extra-galactic nebulae. *Gen. Rel. Grav.*, 2013.

[35] W. de Sitter. On the magnitudes, diameters and distances of the extra-galactic nebulae and their apparent radial velocities. *Bulletin of the Astronomical Institutes of the Netherlands*, 1930.

[36] R. A. Alpher, H. Bethe, and G. Gamow. The origin of chemical elements. *Physical Review*, 1948.

[37] Ralph A. Alpher and Robert Herman. Evolution of the universe. *Nature*, 1948.

[38] A. A. Penzias and R. W. Wilson. A measurement of excess antenna temperature at 4080 mc/s. *Astrophysical Journal*, 1965.

[39] R. B. Partridge. *3K: The Cosmic Microwave Background*. Cambridge University Press, 1995.

[40] R. H. Dicke, P. J. E. Peebles, P. G. Roll, and D. T. Wilkinson. Cosmic black-body radiation. *Astrophysical Journal*, 1965.

[41] Alan H. Guth. Inflationaryuniverse: A possible solution to the horizon and flatness problems. *Phys. Rev. D*, 1981.

[42] Barbara Ryden. *Introduction to Cosmology*. Addison Wesley, 2003.

[43] Gianfranco Bertone, Dan Hooper, and Joseph Silk. Particle dark matter: Evidence, candidates and constraints. *Physics Reports*, 2005.

[44] C. L Bennett et al. Scientific results from cobe. *Advances in Space Research*, 1993.

[45] D. S. Swetz et al. The atacama cosmology telescope: The receiver and instrumentation. *The Astrophysical Journal Supplement*, 2011.

[46] SPT Collaboration. The south pole telescope. *Proc. SPIE Int. Soc. Opt. Eng.*, 2004.

[47] M D Niemack et al. Actpol: A polarization-sensitive receiver for the artacama cosmology telescope. *Proceedings of the SPIE*, 2010.

[48] J. W. Fowler et al. Optical design of the atacama cosmology telescope and the millimeter bolometric array camera. *Applied Optics*, 2007.

[49] J W. Fowler et al. The atacama cosmology telescope: A measurement of the $600 < \ell < 8000$ cosmic microwave background power spectrum at 148 ghz. *Astrophysical Journal*, 2010.

[50] A D Hincks et al. The atacama cosmology telescope (act): Beam profiles and first sz cluster maps. *Astrophysical Journal Supplement*, 2010.

[51] J McMahon et al. Multi-chroic feed-horn coupled tes polarmiteres. *Journal of Low Temperature Physics*, 2012.

[52] R. Datta., J. Hubmayr, C. Munson, et al. Horn coupled multichroic ppolarimeter for the atacama cosmology telscope polarization experiment. *Journal of Low Temperature Physics*, 2014.

[53] Emmanuel Schaan et al. Evidence for the kinematic sunyaev-zel'dovich effect with actpol and velocity reconstruction from boss. *Physical Review D*, 2015.

[54] Matthew Madhavacheril et al. Evidence of lensing of the cosmic microwave background by dark matter halos. *Physical Review Letters*, 2015.

[55] Alexander van Engelen et al. The atacama cosmology telescope: Lensing of cmb temperature and polarization derived from cosmic infrared background cross-correlation. *The Astrophysical Journal*, 2015.

[56] Eva-Maria Mueller, Francesco de Bernardis, Rachel Bean, and Michael D. Niemack. Constraints on massive neutrinos from pairwise kinematic sunyaev-zel'dovich effect. *Physical Review D*, 2015.

[57] Suzanne Staggs, Lyman Page, and David Spergel. Award abstract #1440226 advanced actpol.

[58] S. W. Henderson et al. Advanced actpol cryogenic detector aarray and readout. *Journal of Low Temperature Physics*, 2015.

[59] Erminia Calabrese et al. Precision epoch of reionization studies with next-generation cmb experiments. *Journal of Cosmology and Astroparticle Physics*, 2014.

[60] Silfex Inc. Silicon growing, http://www.silfex.com/services_2_1.html.

[61] Mohammed Nurul Afsar and Xiaohui Li. Millimeter wave complex refractive index, complex dielectric permittivity and loss tangent of high purity and compensated silicon. *International Journal of Infrared and Millimeter Waves*, 1994.

[62] C. J. Glassbrenner and Glen A. Slack. Thermal conductivity of silicon and germanium from 3°k to the melting point. *Phys. Rev.*, 1964.

[63] J. Lau et al. Millimeter-wave antireflection coating for cryogenic silicon lenses. *Applied Optics*, 2006.

[64] P.-S. Kildal, K. Jakobsen, and K. Sudhakar Rao. Meniscus-lens-corrected corrugated horn: a compact feed for a cassegrain antenna. *IEEE Proc. H - Microwaves, Optics and Antennas*, 1984.

[65] S. B. Cohn. *Lens Type Radiators: Antenna Engineering Handbook.* McGraw Hill, 1961.

[66] Tuck C. Choy. *Effective Medium Theory.* Oxford: Clarendon Press, 1999.

[67] KF Schusterothers. Krebs, Y. Guillaud, F. Mattiocco, M . Kornberg, and A. Poglitsch. Micro-machined quasi-optical elements for thz applications. *Proceedings - 16th International Symposium on Space Terahertz Technology*, 2005.

[68] A. MacKay. Proof of polarization independence and nonexistence of crosspolar terms for targets presenting n-fold (n >2) rotational symmetry with special reference to frequency-selective surfaces. *Electron. Lett.*, 1989.

[69] ANSYS. Hfss website: http://www.ansys.com/products/electronics/ansys-hfss.

[70] Jeff McMahon. Private communication.

[71] R. Ulrich. Effective low-pass filters for far infrared frequencies. *Infrared Physics*, 1967.

[72] R. Ulrich. Far-infrared properties of metallic mesh and its complementary structure. *Infrared Physics*, 1967.

[73] Peter A. R. Ade, Giampaolo Pisano, Carole Tucker, and Samuel Weaver. A review of metal mesh filters. *Proc. SPIE*, 6275:62750U–62750U–15, 2006.

[74] Yuki Inoue, Tomotake Matsumura, Masashi Hazumi, Adrian T. Lee, Takahiro Okamura, Aritoki Suzuki, Takayuki Tomaru, and Hiroshi Yamaguchi. Cryogenic infrared filter made of alumina for use at millimeter wavelength. *Appl. Opt.*, 53(9):1727–1733, Mar 2014.

[75] T. R. Manley and D. A. Williams. Scattering filters in the far infrared. *Spectrochimica Acta*, 1965.

[76] Enrico Fermi. *Molecules, Crystals, and Quantum Statistics.* W. A. Benjamin, Inc., 1966.

[77] Yahiko Yamada, Akiyoshi Mitsuishi, and Hiroshi Yoshinaga. Transmission filters in the far-infrared region. *J. Opt. Soc. Am.*, 52(1):17–17, Jan 1962.

[78] L. C. Robinson. *Physical Principles of Far-Infrared Radiation*, volume 10 of *Methods of Experimental Physics.* Academic Press, 1973.

[79] G. A. Niklasson, C. G. Granqvist, and O. Hunderi. Effective medium models for the optical properties of inhomogeneous materials. *Applied Optics*, 20, 1981.

[80] E. R. Dobrovisnkaya, L. A.. Lytvynov, and V. Pishchik. *Sapphire: Material, Manufacturing, Applications.* Springer Science + Business Media, 2009.

[81] Armand Hadni, Jacques Claudel, Xavier Gerbaux, Guy Morlot, and Jean-Marie Munier. Sur le comportement différent des cristaux et des verres dans l'absorption de l'infrarouge lointain (40–1500μ) à la température de l'hélium liquide. *Appl. Opt.*, 4(4):487–494, Apr 1965.

[82] Tomasz P. Biesiadzinski. *Near-Infrared Instrumentation and Millimeter-Wave Simulations for Cosmological Surveys.* PhD thesis, University of Michigan, 2013.

[83] Antony Lewis, Anthony Challinor, and Anthony Lasenby. Efficient computation of cmb anisotropies in closed frw models. *Astrophys. J.*, 538:473–476, 2000.

[84] R. A. Sunyaev and Zel'dovich Ya. B. The observations of relic radiation as a test of the nature of x-ray radiation from the clusters of galaxies. *Comments on Astrophysics and Space Physics*, 1972.

[85] Mark Birkinshaw. The sunyaev-zel'dovich effect. *Physics Reports*, 1999.

[86] Daisuke Nagai, Alexey Vikhlinin, and Andrey V. Kravtsov. Testing x-ray measurements of galaxy clusters with cosmological simulations. *The Astrophysical Journal*, 2007.

[87] M. Arnaud, G. W. Pratt, R. Piffaretti, H. Boehringer, J. H. Croston, and E. Pointecouteau. The universal galaxy cluster pressure profile from a representative sample of nearby systems (rexcess) and the y_sz-m_500 relation. *Astronomy and Astrophysics*, 2010.

[88] G. Lavaux, J. M. Diego, H. Mathis, and J. Silk. Sunyaev-zel'dovich polarization as a probe of the intracluster medium. *Mon. Not. R. Astron. Soc.*, 2004.

[89] Matthias Bartlemann. Gravitational lensing. *Class. Quant. Grav.*, 2010.

[90] Duncan Hanson, Anthony Challinor, and Antony Lewis. Weak lensing of the cmb. *Gen. Rel. Grav.*, 2010.

[91] Henk Hoekstra, Andisheh Mahdavi, Arif Babul, and Chris Bildfell. The canadian cluster comparison project: weak lensing masses and sz scaling relations. *Monthly Notices of the Royal Astronomical Society*, 2012.

[92] H. S. Dumet-Montoya, G. B. Caminha, and M. Makler. Analytic solutions for navarro-frenk-white lens models in the strong lensing regime for low characteristic convergences. *Astronomy and Astrophysics*, 2013.

[93] Itseez. Open source computer vision library. `https://github.com/itseez/opencv`, 2015.

[94] Duncan Hanson, Anthony Challinor, and Antony Lewis. Weak lensing of the cmb. *General Relativity and Gravitation*, 2010.

[95] M. Negrello, F. Perrotta, J.; Gonzlez-Nuevo, L. Silva, G. de Zotti, G. L. Granato, and L. Baccigalupi, C.and Danese. Astrophysical and cosmological information from large-scale submillimetre surveys of extragalactic sources. *Monthly Notices of the Royal Astronomical Society*, 2007.

[96] G. de Zotti, R. Ricci, D. Mesa, L. Silva, P. Mazzotta, L. Toffolatti, and J. Gonzlez-Nuevo. Predictions for high-frequency radio surveys of extragalactic sources. *Astronomy and Astrophysics*, 2005.

[97] Gian Luigi Granato, Gianfranco De Zotti, Laura Silva, Alessandro Bressan, and Luigi Danese. A physical model for the coevolution of qsos and their spheroidal hosts. *The Astrophysical Journal*, 2004.

[98] C. Gruppioni, C. Lari, F. Pozzi, G. Zamorani, A. Franceschini, S. Oliver, M. Rowan-Robinson, and S. Serjeant. A new method for isocam data reduction ii. mid-infrared extragalactic source counts in the elais southern field. *Monthly Notices of the Royal Astronomical Society*, 2002.

[99] Rahul Datta. Personal communication. 2016.